Integrated Analysis of Longitudinal Tumor Burden Data

Citation

Zhao, Rui. 2015. Integrated Analysis of Longitudinal Tumor Burden Data. Doctoral dissertation, Harvard University, Graduate School of Arts & Sciences.

Integrated Analysis of Longitudinal Tumor Burden Data

A thesis presented

by

Rui Zhao

to

The Department of Biostatistics

in partial fulfillment of the requirements
for the degree of
Doctor of Philosophy
in the subject of
Biostatistics

Harvard University
Cambridge, Massachusetts

September 2014

Dissertation Advisor: Professor Franziska Michor Rui Zhao

Integrated Analysis of Longitudinal Tumor Burden Data

Abstract

The first part of this thesis introduces a new statistical method to estimate parameter values in a mixed population consisting of both single- and bi- phasic longitudinal trajectories. This proposed model is capable of categorizing patients according to their longitudinal relationships and estimating the associated parameters of interest, while accounting for between-patient variability. We applied this method to a large phase III randomized trial and found significant differences in patients between different treatment cohorts and within the same treatment cohort, in terms of their longitudinal relationships, with the majority of patients displaying complex bi-phasic trends. In the second part of this thesis, we designed a dynamical system model to explain the observed bi-phasic longitudinal trends and their implications for the underlying cancer biology. We found that a hybrid model encompassing both hierarchical cellular model and clonal expansion model is needed to explain the observed bi-phasic patterns. The third part of this thesis explores the effects of proliferative patterns in colon crypt on crypt stability and rates of somatic evolution.

Contents

List of Figures

List of Tables

Acknowledgments

I would like to thank to my advisor, Professor Franziska Michor, for her dedication, diligence and patience, helping me achieving this important milestone in my life. I would also like to thank my thesis committee members Professor Paul Catalano and Professor Victor De Gruttola for their guidance and support in the last two years.

And thanks to my teachers, professors, friends, and family members.

Estimating Mono- and Bi- Phasic Regression Parameters Using a Piecewise Linear Random-Effects Mixture Model

Rui Zhao[1,2], Paul Catalano[1,2], Victor G. DeGruttola[1], Franziska Michor[1,2]

[1]Department of Biostatistics, Harvard School of Public Health
[2]Department of Biostatistics and Computational Biology, Dana-Farber Cancer Institute

1.1 Summary

A piecewise linear random-effects mixture model taking into account both heterogeneity and nonlinear relationships between biomarkers and time is presented. The proposed model is capable of categorizing patients according to their functional relationships and estimating the associated parameters of interest, while accounting for between-patient variability. This model is applied to a large randomized controlled phase III clinical trial for multiple myeloma. Results from this model suggest that the longitudinal tumor burdens in multiple myeloma patients are heterogeneous and nonlinear, even among patients assigned to the same treatment cohort. In addition, between cohorts, there are distinct differences in terms of the regression parameters and the distributions among categories in the mixture. These results imply that longitudinal data from clinical trials may harbor unobserved subgroups and nonlinear relationships; accounting for both are essential for analyzing longitudinal data. Given the short follow-up time of clinical trials, the current implementation of the model focuses primarily on mono- vs. bi- phasic changes in longitudinal relationships; however this model can be extended to include multi-phasic changes and multiple categories, as well as other clinically important covariates.

Keywords: longitudinal data, random-effects model; mixture distributions; piecewise linear.

1.2 Introduction

The abilities to handle imbalance in the numbers of observations, to distinguish between-subject and within-subject sources of variability, and to model population-level response as well as individual trajectories, make random-effects model a popular choice for analyzing longitudinal data, particularly in medical research [1–3]. Recent progress extends the random-effects models to account for heterogeneity in data, assuming it arises from a finite mixture model [4]. This extension is particularly relevant to clinical research, since clinical data may often contain unobserved categorical variables corresponding to, for example, “responders” or “non-responders”. Ignoring such mixtures may result in biases in estimates. Xu and Hedeker applied this idea and found there is ample evidence of non-homogeneous responses in two large psychiatric clinical trials [5]. Ketchum, Best and Ramakrishnan further extended the mixed-effects mixture models to allow for differences in the variance-covariance matrices [6]. These improvements enable the random-effects models to better characterize heterogeneity in data.

In addition to population heterogeneity, changes in functional relationships between response variables and explanatory variables, particularly with time, are ubiquitous in longitudinal studies: HIV-1 viral load [7, 8], hepatitis B/C viral loads [9, 10], BCR-ABL expression levels in chronic myeloid leukemia [11, 12] and M-protein declines in multiple myeloma [13]. Biomarkers in these examples exhibit nonlinear changes over time, and many of which are biphasic in nature. One method for accounting for changes in the functional relationships is the nonlinear mixed-effects models [14,15]. Morrel *et al.* applied a piecewise nonlinear mixed-effects model to a prostate cancer data set with unknown change time. Naumova, Must and Laird applied a piecewise mixed-effect model with known change points to a prospective study on the development of obesity in female adultescents; in this model, the piecewise change points are the time of menarche [16]. Cudeck and Klebe, and Harring *et al.* applied similar ideas to psychology related data sets [17, 18]. There examples demonstrate the flexibility of the nonlinear mixed-effects models to handle changing functional relationships over time.

Both heterogeneity and varying functional relationships have been addressed separately, however, only a few papers addressed both problems simutaneously. Pauler and Laird introduced a general framework for finite mixture of nonlinear hierarchical models; and they applied their method to investigate noncompliance in a HIV clinical trial [19]. In their application, the mixture consists of a constant mean model for the complying patients and a piecewise linear model for the noncomplying patients. Recently, Lu and Huang extended the general framework proposed by Pauler and Laird to incorporate skewness in distributions [20]; they applied their method to analyze HIV viral load data from the patients enrolled in the ACTG398 trial [21]. The underlying nonlinear mixed-effects model they have used is formulated based on the model structure from a well-known ODE model [22]. One problem associated with these approaches is that their models require extensive prior knowledge in order to specify the nonlinear models before analyzing the data. Misspecification of the model may have detrimental effects on parameter estimation and patient classification. Particularly, if the differences between different categories in the mixture are not well separated, specifying the model becomes an even more challenging problem. To address this issue, we present a piecewise linear random-effects mixture model that does not require any sophisticated prior knowledge of the model structure to address both heterogeneity and time-varying functional relationships. The only assumptions of this proposed model are, that the underlying data may contain a mixture of mono- and bi- phasic observations, and, that the biphasic observations are piecewise linear; no further constraints on the intercepts and slopes are needed. The primary purpose of this model is to offer an initial inspection method to detect for deviations from the linear mixed-effects model. Given the limited numbers of follow-up measurements in clinical trials, the current implementation of the model focuses primarily on mono- vs. bi- phasic changes; however, this proposed model could be generalized to include multi-phasic changes and multi-category mixtures. In addition, because of the piecewise linear nature of the model, other clinically relevant covariates can also be included easily.

1.3 Methods:

We designed a hierarchical model to allow both monophasic and biphasic intercepts and slopes to vary between patients. In addition, for the biphasic patients, the phasic change time is patient-specific. For the i^{th} patient with total M_i observations, the dependent variable y_{ij}, corresponding to the quantitative measure of the disease burden, may either follow a monophasic or a biphasic regression line, depending on the latent indicator variable η_i:

$$\begin{aligned} &\eta_i = 0 : y_{ij} = s_{0i} + s_{1i} t_{ij} + \varepsilon_{ij} \\ &\eta_i = 1 : \left\{ \begin{array}{l} y_{ij} = b_{0i} + b_{1i} t_{ij} + \varepsilon_{ij}, \text{ for } j = 1 \ldots k_i \\ y_{ij} = b'_{0i} + b'_{1i} t_{ij} + \varepsilon_{ij}, \text{ for } j = k_{i+1} \ldots M_i \end{array} \right. \end{aligned} \tag{1.1}$$

where, k_i denotes for the phasic transition point for patient i, if patient i is biphasic. The individual regression parameters, s_i and b_i are drawn from their respective population-level distributions:

$$s_i = \begin{pmatrix} s_{0i} \\ s_{1i} \end{pmatrix} \sim N\left(\begin{pmatrix} S_0 \\ S_1 \end{pmatrix}, \Sigma_{S,2\times 2}\right) = N(S, \Sigma_S) \tag{1.2}$$

$$b_i = \begin{pmatrix} b_{0i} \\ b_{1i} \\ b'_{0i} \\ b'_{1i} \end{pmatrix} \sim N\left(\begin{pmatrix} B_0 \\ B_1 \\ B'_0 \\ B'_1 \end{pmatrix}, \Sigma_{B,4\times 4}\right) = N(B, \Sigma_B) \tag{1.3}$$

Assuming for now that regardless of true "phasicities", biphasic design matrices are given, the "complete-data" likelihood which needs to be maximized is:

$$\begin{gathered} P(S, \Sigma_S, B, \Sigma_B, \sigma^2, \lambda | Y, H) \propto \\ \prod_{i=1}^{N} \{(1-\lambda) P(Y_i | Q_i^s S, Q_i^s \Sigma_S (Q_i^s)^T + I\sigma^2)\}^{1-\eta_i} \prod_{i=1}^{N} \{\lambda P(Y_i | Q_i^b B, Q_i^b \Sigma_B (Q_i^b)^T + I\sigma^2)\}^{\eta_i} \end{gathered} \tag{1.4}$$

where, Q_i^s and Q_i^b denote for the individual mono- and bi- design matrices respectively, and $H = (\eta_1, ..., \eta_N)^T$, where η_i is the missing indicator variable for "phascity". For now, Q_i^s and Q_i^b are assumed to be given and the structures for the mono- and bi- phasic design matrices are shown below:

$$Q_i^s = \begin{bmatrix} 1 & t_{i1} \\ \vdots & \vdots \\ 1 & t_{iM_i} \end{bmatrix} \tag{1.5}$$

$$Q_i^b = \begin{bmatrix} 1 & t_{i1} & 0 & 0 \\ \vdots & \vdots & \vdots & \vdots \\ 1 & t_{ik} & 0 & 0 \\ 0 & 0 & 1 & t_{ik+1} \\ \vdots & \vdots & \vdots & \vdots \\ 0 & 0 & 1 & t_{iM_i} \end{bmatrix} \tag{1.6}$$

The design matrix, shown in Eq (1.6), allows the biphasic model in Eq (1) to be written in the form of standard linear regression [23]. The procedure to construct the biphasic design matrix for each patient is presented in later text.

The corresponding marginal likelihood function is:

$$\begin{aligned} &P(S, \Sigma_S, B, \Sigma_B, \sigma^2, \lambda | Y) \propto \\ &\prod_{i=1}^{N} \{(1-\lambda) P(Y_i | Q_i^s S, Q_i^s \Sigma_S (Q_i^s)^T + I\sigma^2) + \lambda P(Y_i | Q_i^b B, Q_i^b \Sigma_B (Q_i^b)^T + I\sigma^2)\} \end{aligned} \tag{1.7}$$

To maximize the marginal likelihood, we implemented the Expectation Maximization (EM) algorithm coupled with Empirical Bayes estimators, using the procedures derived by Verbeke and Lesaffre [4] and Xu and Hedeker [5]. Following the notations used in Xu and Hedeker, the Empirical Bayes estimators for individual regression parameters and the covariance matrices are:

$$\begin{aligned} \hat{s_i} &= S + (\Sigma_S^{-1} + (Q_i^s)^T (\sigma^2 I_i)^{-1} Q_i^s)^{-1} Q_i^s (\sigma^2 I_i)^{-1} (Y_i - Q_i^s S) \\ \hat{b_i} &= B + (\Sigma_B^{-1} + (Q_i^b)^T (\sigma^2 I_i)^{-1} Q_i^b)^{-1} Q_i^b (\sigma^2 I_i)^{-1} (Y_i - Q_i^b B) \\ \hat{\Sigma}_{s_i} &= (\Sigma_S^{-1} + (Q_i^s)^T (\sigma^2 I_i)^{-1} Q_i^s)^{-1} \\ \hat{\Sigma}_{b_i} &= (\Sigma_B^{-1} + (Q_i^b)^T (\sigma^2 I_i)^{-1} Q_i^b)^{-1} \end{aligned} \tag{1.8}$$

The expectation step calculates the expectation of the "phasicity" indicator variables, η_i:

$$z_i = P(\eta_i = 1 | S, B, \Sigma_S, \Sigma_B, \lambda, \sigma^2, Y_i) = \frac{\lambda \text{\textcircled{1}}_i}{(1-\lambda)\text{\textcircled{0}}_i + \lambda \text{\textcircled{1}}_i} \tag{1.9}$$

where,

$$\begin{aligned} &\text{\textcircled{0}}_i : N(Y_i | Q_i^s S, Q_i^s \Sigma_S (Q_i^s)^T + I\sigma^2) \\ &\text{\textcircled{1}}_i : N(Y_i | Q_i^b B, Q_i^b \Sigma_B (Q_i^b)^T + I\sigma^2). \end{aligned}$$

The maximization step consists of the followings:

$$
\begin{aligned}
\hat{\lambda}^{new} &= \frac{1}{N}\sum_{i=1}^{N} z_i \\
\hat{S}^{new} &= \frac{\sum_{i=1}^{N}(1-z_i)\hat{s}_i}{\sum_{i=1}^{N}(1-z_i)} \\
\hat{B}^{new} &= \frac{\sum_{i=1}^{N} z_i\hat{b}_i}{\sum_{i=1}^{N} z_i} \\
\hat{\Sigma}_S^{new} &= \frac{\sum_{i=1}^{N}(1-z_i)(\hat{\Sigma}_{s_i} + (\hat{s}_i - \hat{S}^{new})(\hat{s}_i - \hat{S}^{new})^T)}{\sum_{i=1}^{N}(1-z_i)} \\
\hat{\Sigma}_B^{new} &= \frac{\sum_{i=1}^{N} z_i(\hat{\Sigma}_{b_i} + (\hat{b}_i - \hat{B}^{new})(\hat{b}_i - \hat{B}^{new})^T)}{\sum_{i=1}^{N} z_i} \\
\hat{\sigma}^{2^{new}} &= \frac{\sum_{i=1}^{N}(1-z_i)[u_i^s(u_i^s)^T + Q_i^s\hat{\Sigma}_{s_i}(Q_i^s)^T]}{\sum_{i=1}^{N}(1-z_i)} + \frac{\sum_{i=1}^{N} z_i[u_i^b(u_i^b)^T + Q_i^b\hat{\Sigma}_{b_i}(Q_i^b)^T]}{\sum_{i=1}^{N} z_i}
\end{aligned}
\tag{1.10}
$$

where, $u_i^s = Y_i - Q_i^s\hat{s}_i$ and $u_i^b = Y_i - Q_i^b\hat{b}_i$.

Hitherto, the EM algorithm is derived under the assumption that biphasic design matrices are provided; however, these matrices are in fact hidden and need to be estimated. The estimation of this biphasic change point is a very-known problem in statistics, mathematics and computer science with many applications in other field, and many methods have been suggested [24,25]. We employed the simplest Bayesian formulation of the change point problem, suggested by Carlin, Gelfand and Smith [26]. For a particular patient i with M_i observations, there are $M_i + 1$ possible change points. For completeness, change points occurring before the first observation and after the last observation are also being considered.

$$Q_{i0}^b = \begin{bmatrix} 0 & 0 & 1 & t_{i1} \\ 0 & 0 & 1 & t_{i2} \\ \vdots & \vdots & \vdots & \vdots \\ 0 & 0 & 1 & t_{iM_i-1} \\ 0 & 0 & 1 & t_{iM_i} \end{bmatrix} \quad (1.11) \qquad Q_{i1}^b = \begin{bmatrix} 1 & t_{i1} & 0 & 0 \\ 0 & 0 & 1 & t_{i2} \\ \vdots & \vdots & \vdots & \vdots \\ 0 & 0 & 1 & t_{iM_i-1} \\ 0 & 0 & 1 & t_{iM_i} \end{bmatrix} \quad (1.12)$$

Equation (1.11) is an example in which phasic transition occurs before the first observation and the example in which phasic transition between the first and the second observations is shown in equation (1.12). The subscripts 0 and 1 in Q_{i0}^b and Q_{i1}^b denote the position before which observations the phasic changes occur. Assuming all patients follow the trial protocol precisely, despite its infinitesimal probability, the phasic transition problem can be formulated into a finite mixture problem, in which each split of the design matrix is a distinct category. The overall marginal likelihood is:

$$L(S, B, \Sigma_S, \Sigma_B, \lambda, \pi, \sigma^2 | Y) = \\ \prod_{i=1}^{N} \{(1-\lambda) N(Y_i | Q_i^s S, Q_i^s \Sigma_S (Q_i^s)^T + I\sigma^2) + \lambda \sum_{j=0}^{M_i} \pi_{ij} N(Y_i | Q_{ij}^b B, Q_{ij}^b \Sigma_B (Q_{ij}^b)^T + I\sigma^2)\} \tag{1.13}$$

where, $\pi = (\pi_1^T, ..., \pi_N^T)^T$ and $\pi_i = (\pi_{i1}, ..., \pi_{iM_i})^T$, representing the vector of weighting factors. The corresponding conditional likelihood, conditioning on the unobserved indicator variables, can be written as:

$$L(S, B, \Sigma_S, \Sigma_B, \lambda, \pi, \sigma^2 | Y, \Xi, H) = \\ \prod_{i=1}^{N} [(1-\lambda) N(Y_i | Q_i^s S, Q_i^s \Sigma_S (Q_i^s)^T + I\sigma^2)]^{1-\eta_i} [\lambda \prod_{j=0}^{M_i} \{\pi_{ij} N(Y_i | Q_{ij}^b B, Q_{ij}^b \Sigma_B (Q_{ij}^b)^T + I\sigma^2)\}^{\xi_{ij}}]^{\eta_i} \tag{1.14}$$

where, ξ_{ij} is the unobserved indicator for j^{th} biphasic design matrix for subject i, such that $\sum_{j=0}^{M_i} \xi_{ij} = 1$, and $\xi_i = (\xi_{i0}, ..., \xi_{iM_i})^T$ and $\Xi = (\xi_1^T, ..., \xi_N^T)^T$. The EM algorithm can be applied to the conditional likelihood (1.14) to maximize the marginal likelihood function, equation (1.13). In the expectation step,

$$\zeta_{ij} = P(\xi_{ij} = 1 | B, \Sigma_B, \sigma^2, Y_i) = \frac{\pi_{ij} N(Y_i | Q_{ij}^b B, Q_{ij}^b \Sigma_B (Q_{ij}^b)^T + I\sigma^2)}{\sum_{j=0}^{M_i} \pi_{ij} N(Y_i | Q_{ij}^b B, Q_{ij}^b \Sigma_B (Q_{ij}^b)^T + I\sigma^2)} \tag{1.15}$$

is calculated. Similarly, the expected value for η_i can be calculated:

$$z_i = P(\eta_i = 1 | S, B, \Sigma_S, \Sigma_B, \lambda, \sigma^2, Y_i) = \frac{\lambda exp(\textcircled{3}_i)}{(1-\lambda) exp(\textcircled{2}_i) + \lambda exp(\textcircled{3}_i)} \tag{1.16}$$

where,

$$②_i : 2logN(Y_i|Q_i^s S, Q_i^s \Sigma_S (Q_i^s)^T + I\sigma^2) - 2log(M_i)$$

$$③_i : 2log(\sum_{j=0}^{M_i} \pi_{ij} N(Y_i|Q_{ij}^b B, Q_{ij}^b \Sigma_B (Q_{ij}^b)^T + I\sigma^2)) - 4log(M_i)$$

where, $②_i$ and $③_i$ are the negative bayesian information criteria (BIC) for the mono- and bi- phasic models respectively. Bayesian information criterion corrects for improvement in fitting associated with increasing model complexity and the $M_i + 1$ possible design matrices for the biphasic model. In addition, bayesian information criterion ensures model identifiability by penalizing against the biphasic model. The advantage of this approach is that it does not require prior knowledge for specifying the conditions needed to ensure identifiability, such as $B_1 < S_1 < B_1'$ and $B_0' < B_0$. In terms of selecting for the appropriate penalty factors for the BIC, we used the most "naive" penalty factors of 2 and 4 which correspond to the numbers of regression parameters in the mono- and biphasic models.

Assuming all patients comply with the trial protocol precisely, $\pi_j = \pi_{ij} = \pi_{i'j}$, the maximization of ζ_{ij} can be easily achieved:

$$\pi_j^{new} = \pi_{ij}^{new} = \pi_{i'j}^{new} = \frac{\sum_{i=1}^{N} \zeta_{ij} z_i}{\sum_{i=1}^{N} z_i}. \tag{1.17}$$

However, in practice never do all patients follow the trial design precisely; frequently, patients either miss follow-up visits completely or not according to their scheduled time. This departure from the trial design creates misalignments between patients' observation intervals. To compensate for this departure from the trial design and to correct for misalignments, a novel continuous time variable specifying the phasic transition probability as a function of time is introduced:

$$\theta(t) = \frac{\sum_{i=1}^{N} \sum_{j=1}^{M_i - 1} \zeta_{ij} I(t_{ij} < t < t_{i(j+1)}) z_i}{\int_0^{max(t)} \sum_{i=1}^{N} \sum_{j=1}^{M_i - 1} \zeta_{ij} I(t_{ij} < t < t_{i(j+1)}) z_i dt}. \tag{1.18}$$

Continuous variable $\theta(t)$ represents the normalized phasic transition density at time t. The weight for each interval for each patient can be updated by integrating over its corresponding interval:

$$\pi_{ij}^{new} = \int_{t_{ij}}^{t_{i(j+1)}} \theta(t) dt. \tag{1.19}$$

We ignore the scenarios in which biphasic transitions occur before the first observation or after the last observation, since the regression lines in these two cases are monophasic in nature.

The Empirical Bayes estimators for the biphasic individual regression parameters and biphasic covariance matrices are modified to take into account this additional layer of mixture among biphasic patients:

$$\begin{aligned}\hat{b}_{ij} &= B + (\Sigma_B^{-1} + (Q^b_{ij})^T(\sigma^2 I_i)^{-1} Q^b_{ij})^{-1} Q^b_{ij} (\sigma^2 I_i)^{-1}(Y_i - Q^b_{ij} B) \\ \hat{\Sigma}_{b_{ij}} &= (\Sigma_B^{-1} + (Q^b_{ij})^T(\sigma^2 I_i)^{-1} Q^b_{ij})^{-1}\end{aligned} \tag{1.20}$$

For the monophasic parameters, the maximization step remains unchanged; and the maximization steps for the biphasic parameters and the variance consist of the following steps:

$$\begin{aligned}\hat{B}^{new} &= \frac{\sum\limits_{i=1}^{N}\sum\limits_{j=0}^{M_i} z_i \zeta_{ij} \hat{b}_{ij}}{\sum\limits_{i=1}^{N} z_i} \\ \hat{\Sigma}_B^{new} &= \frac{\sum\limits_{i=1}^{N}\sum\limits_{j=0}^{M_i} z_i \zeta_{ij} (\hat{\Sigma}_{b_{ij}} + (\hat{b}_{ij} - \hat{B}^{new})(\hat{b}_{ij} - \hat{B}^{new})^T)}{\sum\limits_{i=1}^{N} z_i} \\ \hat{\sigma}^{2new} &= \frac{\sum\limits_{i=1}^{N}(1 - z_i)[u^s_i (u^s_i)^T + Q^s_i \hat{\Sigma}_{s_i} (Q^s_i)^T]}{\sum\limits_{i=1}^{N}(1 - z_i)} + \frac{\sum\limits_{i=1}^{N}\sum\limits_{j=0}^{M_i} z_i \zeta_{ij} [u^b_{ij} (u^b_{ij})^T + Q^b_{ij} \hat{\Sigma}_{b_{ij}} (Q^b_{ij})^T]}{\sum\limits_{i=1}^{N} z_i}\end{aligned} \tag{1.21}$$

where, $u^b_{ij} = Y_i - Q^b_{ij} \hat{b}_{ij}$.

The Gibbs' sampler is used to assess the uncertainty associated with the parameter estimates. The starting values for the Gibbs' sampler are obtained from the aforementioned algorithm and the detailed steps for the Gibbs' sampler are listed below:

1. Calculate ζ_{ij} for each patient, using equation (1.15).

2. For each patient, draw a ξ_i vector from a multinomial distribution with a parameter vector ζ_i; and obtain the corresponding biphasic design matrix Q^b_{ij}, such that $\xi_{ij} = 1$.

3. Calculate z_i based on the monophasic design matrix, Q_i^s and the biphasic design matrix Q_{ij}^b from step (3).

4. Draw η_i from Bernoulli distribution with parameter z_i for each patient.

5. Update $\theta(t)$ using equation (1.18), with ζ_{ij} replaced by ξ_{ij} and z_i replaced by η_i.

6. Draw a vector π_i from a Dirichlet distribution with a parameter vector $(\int_{t_{i1}}^{t_{i2}} \theta(t)dt, ..., \int_{t_{iM_i-2}}^{t_{iM_i-1}} \theta(t)dt)$, for each patient.

7. Draw λ from a Beta distribution with parameters $(\sum\limits_{i=1}^{N} \eta_i + 1, \sum\limits_{i=1}^{N} (1 - \eta_i) + 1)$.

8. Sampling s_i and b_i:

$$\begin{aligned} s_i &\sim N(\hat{s}_i, \hat{\Sigma}_{s_i}) \\ b_i &\sim N(\hat{b}_{ij}, \hat{\Sigma}_{b_{ij}})) \end{aligned} \tag{1.22}$$

where, $\hat{s}_i$ and $\hat{\Sigma}_{s_i}$ are from equation (1.8), and $\hat{b}_{ij}$ and $\hat{\Sigma}_{b_{ij}}$ are from equation (1.21). The design matrix for the biphasic is draw from step (2).

9. Sampling S and B from s_i and b_i:

$$\begin{aligned} S &\sim N\left(\frac{\sum\limits_{i=1}^{N} (1 - \eta_i) s_i}{\sum\limits_{i=1}^{N} (1 - \eta_i)}, \frac{\Sigma_S}{\sum\limits_{i=1}^{N} (1 - \eta_i)}\right) \\ B &\sim N\left(\frac{\sum\limits_{i=1}^{N} \eta_i b_i}{\sum\limits_{i=1}^{N} \eta_i}, \frac{\Sigma_B}{\sum\limits_{i=1}^{N} \eta_i}\right) \end{aligned} \tag{1.23}$$

10. Sampling Σ_S and Σ_B:

$$\begin{aligned} \Sigma_S &\sim Inv - Wishart(\sum_{i=1}^{N} (1 - \eta_i) - 1 - 2, \sum_{i=1}^{N} (1 - \eta_i)(s_i - S)(s_i - S)^t) \\ \Sigma_B &\sim Inv - Wishart(\sum_{i=1}^{N} (\eta_i) - 1 - 4, \sum_{i=1}^{N} (\eta_i)(b_i - B)(b_i - B)^t) \end{aligned} \tag{1.24}$$

11. Sampling σ^2:

$$\begin{aligned} &Inv - \chi^2(\sum_{i=1}^{N} M_i - 2, \\ &\qquad \frac{1}{\sum\limits_{i=1}^{N} M_i - 2} \sum_{i=1}^{N} \{(1 - \eta_i)(Y_i - Q_i^s s_i)^t (Y_i - Q_i^s s_i) + (\eta_i)(Y_i - Q_i^b b_i)^t (Y_i - Q_i^b b_i)\}) \end{aligned} \tag{1.25}$$

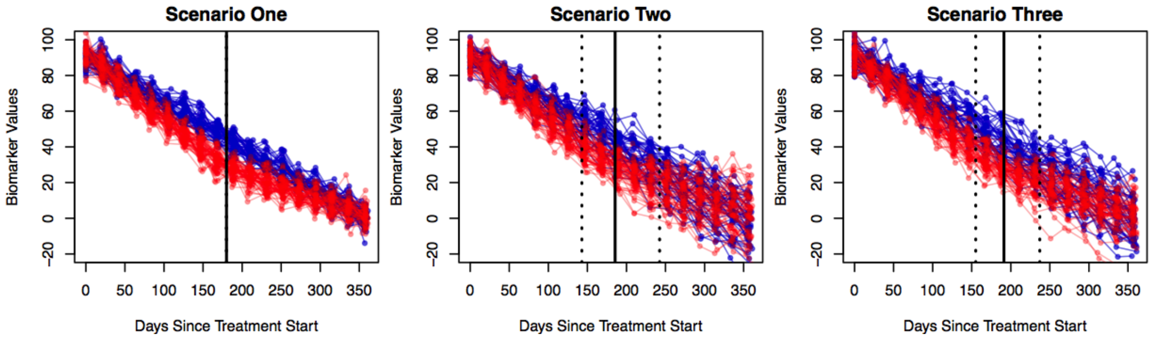

Figure 1.1: Longitudinal trajectories for the simulated patients in the three scenarios. Blue lines indicate monophasic patients' trajectories; red lines indicate biphasic patients' trajectories. Vertical solid lines indicate the median time at which phasic transitions occur for the biphasic patients; vertical dashed lines indicate the 10^{th}% and 90^{th}% phasic transition time. All biphasic patients have the same phasic transition time in scenario one; hence, the dashed and solid lines coincide.

1.4 Simulations

We designed three simulation studies to test the algorithms' abilities to categorize patients and to estimate parameters. All three scenarios have the same population level regression parameters as shown in Table 1.1; the differences between the three scenarios lie in the covariance matrices specifying for between-patient variability. The first simulation scenario assumes that there is no between-patient variability; the second simulation scenario assumes that there is between-patient variability in the intercepts and slopes in both mono- and bi- phasic patients; however, there are no correlations between these parameters, *i.e.* all non-diagonal cells in Σ_s and Σ_b are zero. The third scenario assumes there is a significant positive correlation between the first and second slopes among the biphasic patients, with correlation 0.5. In each scenario, we simulated 100 patients, $N = 100$. The proportion of biphasic patients is 0.60, $\lambda = 0.60$; *i.e.* there are 60 biphasic and 40 monophasic patients. Each patient according to a hypothetical protocol is measured every 21 days for 1 baseline and 17 follow-up measurements for a total follow-up duration of 357 days. In this simulation study, the actual visits may deviate within ± 5 days from the scheduled time. The true individual regression parameters are drawn from multivariate normal distributions with respective population parameters and covariance matrices, (S, Σ_S), or (B, Σ_B), depending on "phascities". For each simulated biphasic patient i, phasic transition time occurs at $t = \frac{b_{i0}-b'_{i0}}{b'_{i1}-b_{i1}}$.

We first applied the EM algorithm to estimate the parameter values that maximize the marginal likelihood. The true and estimated parameters, excluding the covariance for the three scenarios, are shown in Table 1.1. In all three scenarios, the proposed model was able provide parameter estimates that are in close proximity to the true parameter values. The only exception is that the biphasic proportion parameter λ is biased towards the monophasic model in scenarios 2 and 3. These biases are the results of the BIC correction for ensuring model identifiability and compensating for overfitting. Estimating the covariance matrices for scenarios two and three is more challenging, Table 1.2. In particular, we found that the proposed model consistently over-estimates the variance term associated with the second intercept for the biphasic patients. Three possible causes for this poor estimation are: 1) the biphasic design matrices are estimated; misclassification of observations between the first and second phases may result in an enlarged variance term for the second intercept. 2) estimation of the second intercept requires projection back to time zero; uncertainty is magnified by projection. 3) In the phasic transition time in our simulated data is distributed according the Gaussian ratio distribution, with heavy tails [27]; thus, biphasic patients with extreme transition time may not be classified correctly. The reason for simulating the transition time using the Gaussian ration distribution is made based on the observation that the phasic transition time in real data often have heavy tails. In addition to parameter estimation, the proposed model was able to classify patients according to their “phasicities”, Table 1.3.

Table 1.1: The true and the means of the estimated parameters in the three simulation scenarios. The means of the estimated parameters are calculated based on 1,000 simulation runs for each scenario.

	S_0	S_1	B_0	B_1	B'_0	B'_1	σ	λ
Truth	90.00	-0.2500	91.00	-0.3500	55.00	-0.1500	5.00	0.6000
Scenario One	89.99	-0.2499	90.83	-0.3463	56.20	-0.1538	4.89	0.5999
Scenario Two	89.79	-0.2569	90.57	-0.3466	56.87	-0.1506	5.00	0.5058
Scenario Three	89.80	-0.2533	90.63	-0.3453	56.74	-0.1535	4.98	0.5449

In addition to the three scenarios, we performed sensitivity analysis to test the effects of population-level intercepts and slopes, S_0, S_1, B_0, B_1, B'_0, and B'_1 on classification accuracy, Figure 1.2. For each of the three scenarios, we tested a grid of values for the biphasic first slope, B_1 (-0.45, ..., -0.26),

Table 1.2: The true and the means of estimated covariance components in the three simulation scenarios. True values are shown outside of the parentheses and estimated values are shown inside the parentheses. The lower triangular components of the monophasic covariance matrix and the upper triangular components of the biphasic covariance matrix are shown. The means of the estimated covariance components are calculated based on 1,000 simulation runs for each scenario.

Scenario One

	b_0	b_1	b_0'	b_1'	
	0.0000 (1.6766)	0.0000 (-0.0140)	0.0000 (0.3485)	0.0000 (-0.0011)	b_0
		0.0000 (0.0002)	0.0000 (-0.0060)	0.0000 (0.0000)	b_1
s_0	0.0000 (0.8547)		0.0000 (12.469)	0.0000 (-0.0442)	b_0'
s_1	0.0000 (-0.0035)	0.0000 (0.0000)		0.0000 (0.0002)	b_1'
	s_0	s_1			

Scenario Two

	b_0	b_1	b_0'	b_1'	
	4.0000 (5.1418)	0.0000 (-0.0124)	0.0000 (0.9831)	0.0000 (-0.0062)	b_0
		0.0009 (0.0006)	0.0000 (-0.0070)	0.0000 (0.0003)	b_1
s_0	4.0000 (4.4488)		4.0000 (12.931)	0.0000 (-0.0480)	b_0'
s_1	0.0000 (-0.0019)	0.0009 (0.0011)		0.0009 (0.0009)	b_1'
	s_0	s_1			

Scenario Three

	b_0	b_1	b_0'	b_1'	
	4.0000 (5.0456)	0.0000 (-0.0117)	0.0000 (0.8151)	0.0000 (-0.0036)	b_0
		0.0009 (0.0007)	0.0000 (-0.0097)	0.0000 (0.0006)	b_1
s_0	4.0000 (4.3801)		4.0000 (13.589)	0.0000 (-0.0461)	b_0'
s_1	0.0000 (0.0017)	0.0009 (0.0010)		0.0009 (0.0010)	b_1'
	s_0	s_1			

Table 1.3: Classification accuracy for the three scenarios. A representative example for each scenario and the averages of 1,000 simulation runs are shown. A hard cut-off for calling a patient mono- or bi- phasic is used based on the expected probabilities of being biphasic. Patients with expected biphasic probabilities exceeding 0.5 are called to be biphasic, otherwise, monophasic.

Representative examples		Scenario 1		Scenario 2		Scenario 3	
		Truth		Truth		Truth	
		Monophasic	Biphasic	Monophasic	Biphasic	Monophasic	Biphasic
Estimated	Monophasic	40	0	40	7	40	1
	Bi-phasic	0	60	0	53	0	59
	Sensitivity/Specificity	100%	100%	100%	88%	100%	98%
Averages of 1,000 simulations		100%	100%	99.88%	84.37%	99.85%	90.87%

and the second slope, B_1' (-0.24, ..., -0.05), centering around the monophasic slope $S_1 = -0.25$. For this sensitivity analysis, the second intercept for the biphasic patients were kept at the values such that the population-level phasic transition time occur at the middle of the time span of the trial (178 days). All other parameters, S_0, S_1, B_0, σ and λ were kept at the values used in the previous three scenarios. The covariance matrices, if applicable, were also kept at the values used in the three scenarios. As expected, as the biphasic first and second slopes approach the value of the monophasic slope, the specificity diminishes in all three scenarios. More biphasic patients are misclassified as monophasic patients. Due to the strong penalty induced by the BIC correction in deciding patients "phascities", the proposed model is biased toward the monophasic model. Sensitivity is close to 100% in all three scenarios; hence the contour plots for sensitivity are not shown. In addition, we also investigated the effects of the numbers of observations per patient and the effects of the numbers of patients on the model's ability to distinguish between mono- and bi-patients. As expected, as the number of observations per patient decreases, specificity decreases. Interestingly, the model is less sensitive towards the total numbers of patients, Figure 1.3.

In addition to obtaining the maximum likelihood parameter estimates, Gibbs' sampling was implemented to assess the statistical significance of the estimated parameters for the three scenarios. The key parameter of interest in this simulation study is the coverage probability for the proposed model. We simulated 1,000 independent data sets using identical parameters values for each scenario. The EM algorithm is first applied to search for the parameter values that maximize the likelihood; then using them as the starting values, a Monte Carlo simulation is performed for each data set, with the number of iterations per simulation equal 30,000. With these samples

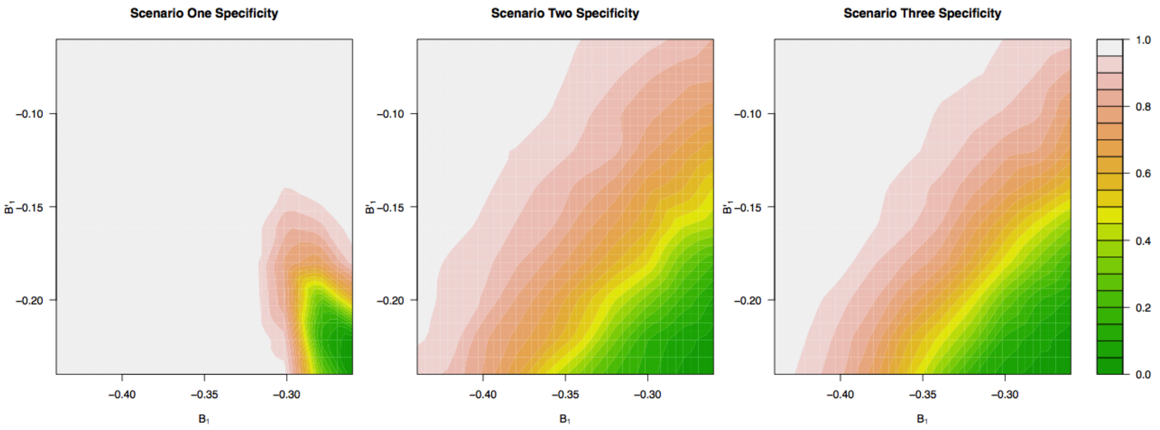

Figure 1.2: Specificity as a function of true biphasic slopes. True monophasic slope is kept at -0.25; biphasic first slopes vary between -0.45 and -0.26; biphasic second slopes vary between -0.24 and -0.05. Population-level monophasic slope and biphasic first intercepts are 90 and 91 respectively; the second slopes for biphasic patient are selected such that the population level phase transition occurs at 178 days, which is in the middle of 357-day trial period. Each graph is generated based the averages of 10 simulations.

generated from the posterior distribution, we constructed a 95% simultaneous rectangular credible region for each simulated data set, using the method outlined by Held [28, 29]. The coverage probability is calculated as the probabilities of the simultaneous credible regions covering all 8 parameters for scenario one and covering all 21 parameters in scenarios two and three, out of the 1,000 simulated data sets. The coverage probabilities are 80.8%, 75.0% and 76.4% for the three scenarios, respectively. We performed detailed analysis to determine the parameter with the worst coverage probability in each scenario. For scenario one, the estimated standard deviation, σ, has the worst coverage probability of only 87.2%. The σ sampled from the Gibbs' sampler are consistently smaller than the actual noise standard deviation. This discrepancy can be explained by the mismatch between the model, which assumes the existence of between-patient variability, and the simulated data, in which all patients are identical in terms of their regression parameters. Thus, the model mistakenly attributes a portion of the random noise to the between-patient covariance matrices, hence reducing the variance of the noise term. Further analysis for scenarios two and three reveals that the variance component for the biphasic second intercept has the lowest coverage rate among all parameters; the 95% simultaneous credible regions for all 21 parameters only were able to cover the covariance term for the second intercept at rates of 90.1% and 90.7% for scenarios two and three, respectively. In this case, the covariance components obtained from

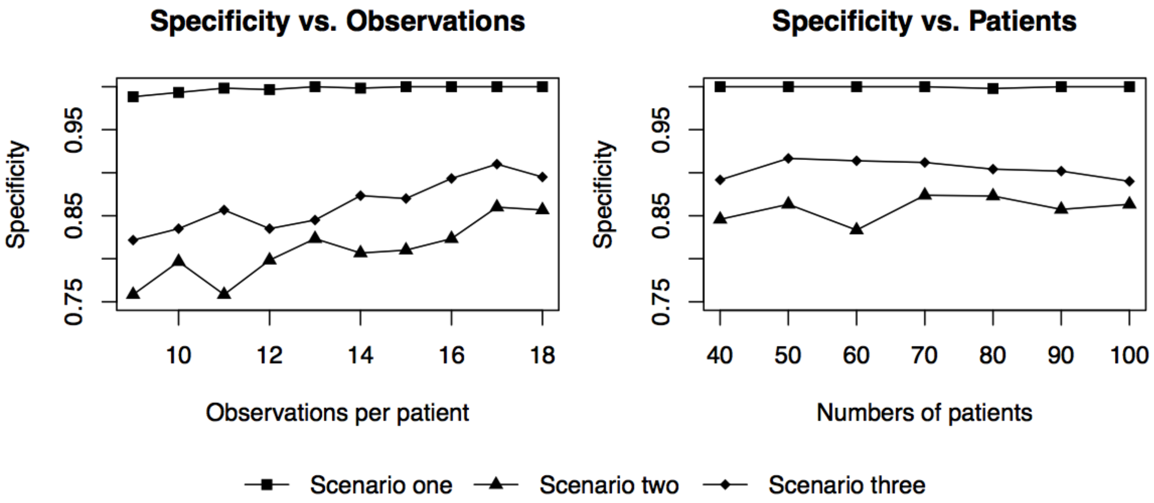

Figure 1.3: Specificity as a function of the numbers of observations per patient and the total numbers of patients per simulated data set. Parameter values are identical to these used in the three scenarios. The numbers of observations per patient vary in the figure on the left; these observations are evenly distributed between day 0 and day 357. The total numbers of patients, N, vary in the figure on the right; the number of observations per patient is kept at 18.

the Gibbs' sampler are consistently higher than the true covariance used in the simulated data. The same reasons, mentioned in the EM algorithm section, can explain this enlarged covariance. Another parameter of particular interest is the correlation between the first and second slopes in scenario three. Focusing only on this parameter, our model was able to detect this significant correlation in 62.1% of the simulation runs; significant correlation is defined as 0 not being covered by the 95% credible region. Overall, the actual coverage probabilities from the proposed model are lower than the nominal probabilities. Model complexity is believed to be a leading contributor for this poor coverage; as previous research has shown that even in the simple binomial case, coverage probability rarely agrees with the nominal probability [30]. In addition, the parameter values, particularly the slopes, used in our simulation have considerable overlaps; this makes the identification of patients' "phasicities" difficult, lowering the coverage probabilities.

To ensure fairness in assessing model's ability to estimate parameters, the true model parameters and patients' "phascities" were never used and are always hidden. The starting values for the EM algorithm were determined based on an *ad hoc* procedure. For the monophasic patients, the starting values are estimated by fitting each patient, regardless of the true "phascity", a simple linear regression. The maximum and minimum values in intercepts and slopes define the range of the starting values for the EM algorithm. The monophasic between-patient covariance matrix is obtained by calculating the covariance between simple linear regression parameters. For the biphasic starting values, 0^{th} to X^{th} percentiles of observations and Y^{th} to 100^{th} percentile of observations, ranked according to time of measurement, are used to establish the range for the first and second phases. Likewise, the covariance for these parameters is used as the starting values for the between-patient covariance matrix. The standard deviation for the noise is obtained from fitting a simple linear regression to all data points across all patients. The proportion parameter, λ, is always assumed to be 0.5, to reflect the lack of prior knowledge. The continuous weighting variable $\theta(t)$ is seeded from a normal distribution density centered at the phasic change point established by the biphasic starting values; the associated standard deviation term is kept at 1/10 of the maximum observation span.

1.5 Application

To further demonstrate the utility of the proposed method, we applied it to the M-protein data from the Velcade as Initial Standard Therapy in Multiple Myeloma: Assessment with Melphalan and Prednisone (VISTA) trial [31]. Briefly, the VISTA trial is a randomized, open-label phase III study, consisting of 682 patients with newly diagnosed, untreated, symptomatic, measurable multiple myeloma patients. In this study, the patients were randomized to treatment either with melphalan and prednisone with (VMP cohort) or without bortezomib (MP cohort) (bortezomib, Johnson & Johnson Pharmaceutical R&D and Millennium). Measurable disease was defined as the presence of quantifiable M-protein in serum or urine, or measurable soft-tissue or organ plasmacytomas. The longitudinal M-protein data for patients in the VISTA are shown in Figure 1.4.

The parameter estimates from our model reveal a few interesting features associated with the M-protein dynamics, Table 1.4. First, the differences between the first and second slopes for the biphasic patients in both cohorts are striking. For the biphasic patients, the first slopes are

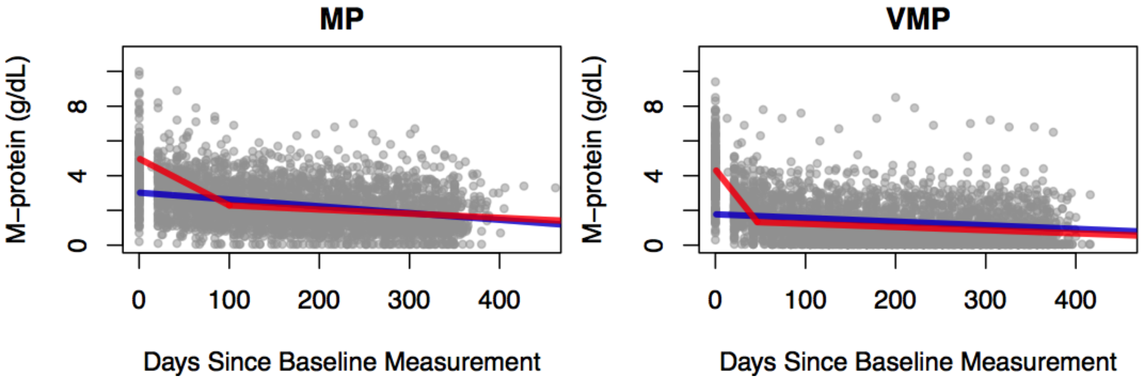

Figure 1.4: Longitudinal trajectories for patients in the VISTA trial separated by treatment cohorts. The monophasic (blue) and biphasic (red) lines indicate the population-mean trajectories based on maximum likelihood estimates from the EM algorithm.

significantly more negative than the second slopes in both cohorts. Second, the proportions of biphasic patients are significantly different in the two cohorts. Third, the biphasic first slope in the VMP cohort is more negative than the biphasic first slope in the MP cohort. Forth, the biphasic first intercept are similar in both cohorts. Fifth, the long-term declines for the biphasic patients in both cohorts are not significantly different. Sixth, in both cohorts, the intercepts for the monophasic patients tend to be substantially smaller than the first intercepts of the biphasic patients. Lastly, in the MP cohort, despite the large differences in the rates of initial declines, the long-term declines are very similar between the monophasic and the biphasic patients, as shown by the similarity in the estimates for S_1 and B_1'. These observed differences in the M-protein dynamics between cohorts suggest that the tumor dynamics of multiple myeloma are highly complex. Once possible explanation proposed by us is that the tumor dynamics follows a hybrid mathematical model with both hierarchical and clonal expansion components [13].

Table 1.4: 95% simultaneous credible regions for the MP and VMP cohorts in the VISTA trial.

Cohorts	S_0	S_1	B_0	B_1	B_0'	B_1'	σ	λ
MP	(2.332, 3.062)	(-0.004, -0.002)	(4.344, 5.452)	(-0.036, -0.016)	(2.234, 3.230)	(-0.004, -0.001)	(0.254, 0.279)	(0.359, 0.592)
VMP	(1.064, 2.686)	(-0.003, -0.000)	(3.996, 4.689)	(-0.077, -0.053)	(1.114, 1.671)	(-0.002, -0.001)	(0.220, 0.340)	(0.794, 0.938)

1.6 Discussion

We have proposed a piecewise linear mixture random-effects model to investigate heterogeneity and time varying functional relationships in longitudinal data. This proposed model is a special case of the general framework proposed by Pauler and Laird [19]. The proposed model assumes a simple yet robust piecewise linear functional form. The major advantage of this piecewise linear functional form over other more complex nonlinear functions is that the likelihood can be maximized analytically, using empirical Bayes estimators and standard expectation-maximization algorithm. No prior knowledge of the functional relationship other than the piecewise assumption is required; this method would be particularly useful for initial exploratory analysis. In addition, in the extreme case in which all patients are monophasic, the proposed model completely reduces to the linear mixed-effects model. Although not shown here, this model can be easily extended to include covariates other than time alone. In addition, the ease of interpretation of the parameter estimates is another advantage of the proposed model. One minor drawback of our approach is that for the biphasic patients, Eq (1.1), the proposed model produces a point of discontinuity between k_i and k_{i+1} observations. Nonlinear models, such as the broken-stick model, Bacon Watts model, and, polynomial model suggested by Matthews *et. al.* offer potential solutions to this problem [32]; however, analytical solutions do not exist for these nonlinear functions.

From the prospectives of clinical trial design, one interesting question is how to design a trial to maximize "phasicity" detection. Our linear framework may offer a simpler approach to address such questions. Although from our analysis of the M-protein data we have not found significant correlation between "phasicities" and patients' outcomes, the distinct mono- and bi- phasic trajectories may have significant medical importance, that warrants further medical and biological investigations. Better ability in identifying patients according to their individual trajectories may further improve patient prognosis and disease management. Similar conclusion was reached by Lu and Huang in their analysis of HIV viral load data [20]. In addition, our model can also be extended beyond between-patient variability by including additional layers inside the hierarchy. For instance, patients with metastatic solid tumors, multiple tumors at different sites may share a large degree of similarity yet having distinct differences depending on their micro environments. Modeling on-treatment responses require the incorporation of between-patient variability and within-patient-between-tumor variability. These questions can be addressed easily in the proposed piecewise linear framework.

Myeloma Stem Cells Are Relatively Insensitive to Targeted Therapy

Min Tang[1,2,*], Rui Zhao[1,2,*], Helgi Van de Velde[3], Yawei Ge[2], Constantine Mitsiades[4], Suzanne Viselli[5], Rachel Neuwirth[6], Dixie-Lee Esseltine[6], Kenneth Anderson[4], Jesús F. San Miguel[7], Paul G. Richardson[4], Michael H. Tomasson[8], Franziska Michor[1,2]

[1]Department of Biostatistics, Harvard School of Public Health
[2]Department of Biostatistics and Computational Biology, Dana-Farber Cancer Institute [3]Oncology R&D, Janssen Research & Development, a division of Janssen Pharmaceutica NV, Beerse, Belgium
[4]Dana-Farber Cancer Institute, Boston, Massachusetts 02215, USA
[5]Oncology R&D, Janssen Research & Development LLC, Raritan, USA
[6]Millennium Pharmaceuticals, Inc., Cambridge, USA
[7]Hospital Universitario Salamanca, CIC, IBMCC (USAL-CSIC), Salamanca, Spain
[8]Division of Oncology, School of Medicine, Washington University in St. Louis, St Louis, Missouri 63130 USA
[*]Equal contribution

2.1 Summary

Current standard therapy induces complete responses and prolongs overall survival in multiple myeloma (MM) patients, but ultimately fails to eradicate disease [33]. Here, we analyzed tumor response data from two large randomized controlled phase III trials [31, 34–36] and a randomized controlled phase II trials [37] to establish and validate a mathematical model of MM cell dynamics. Dynamics of treatment response in newly diagnosed patients were most consistent with a mathematical model postulating the existence of two tumor cell subpopulations, "myeloma progenitor cells" and "myeloma differentiated cells". Differential treatment responses were observed with significant tumoricidal effects on myeloma differentiated cells and less clear effects on myeloma progenitor cells. When applying our model to data of relapsed MM patients [34], we found that a hybrid mathematical model incorporating both a MM differentiation hierarchy and clonal evolution best explains the tumor response patterns in all patients. The clinical data, together with mathematical modeling, suggests that bortezomib-based therapy exerts a selection pressure on the myeloma cells that can shape the disease phenotype, thereby generating further inter-patient variability. Our modeling approach incorporating clonal evolution and a cancer differentiation hierarchy also has implications for other tumor types.

2.2 Introduction

Therapy with melphalan and prednisone has been the standard of care for elderly patients with newly diagnosed multiple myeloma (MM) for more than 40 years [38, 39]. In 2008, the proteasome inhibitor bortezomib (Velcade®) was approved in combination with melphalan and prednisone for treatment of newly diagnosed MM patients not eligible for high-dose chemotherapy, based on the results of the randomized phase III VISTA trial comparing bortezomib-melphalan-prednisone to melphalan-prednisone treatment [34]. Earlier, bortezomib was approved for treatment of relapsed multiple myeloma based on the results of the randomized phase III APEX trial comparing bortezomib monotherapy to dexamethasone treatment [35, 36]. Although in both phase III studies, bortezomib had been able to induce complete tumor responses and significantly prolong survival [31, 36, 40] myeloma relapses eventually occurred and the patients could not be considered cured. Recently a new phase II trial investigating the safety and efficacy of the addition of siltuximab to the bortezomib-melphalan-prednisone regimen showed no significant survival difference associated with siltuximab [37]. Furthermore, the existence of a differentiation hierarchy of MM cells has been suggested [41], but the effects of chemotherapies on different subpopulations remain largely unexplored. Here we analyzed the treatment response of MM patients and sought to identify the effects of treatment on different subpopulations of cells.

2.3 Methods

To develop a mathematical model for multiple myeloma (MM) tumor cell dynamics under treatment, we utilized M-protein data from 682 newly diagnosed MM patients in the VISTA trial [31]. First, we utilized a statistical modeling approach to identify unique treatment response trends among patients; second, we constructed a dynamical system model to model multiple myeloma tumor cell dynamics. This dynamical system model is updated and validated using two independent trials, the CNTO 328 trial [37] and the APEX trial [36].

2.3.1 Trial summaries and patient selection

VISTA trial

The Velcade as Initial Standard Therapy in Multiple Myeloma: Assessment with Melphalan and Prednisone (VISTA) trial is a randomized, open-label phase III study, consisting of 682 patients with newly diagnosed, untreated, symptomatic, measurable Multiple Myeloma (MM) patients. These patients were not candidates for high-dose therapy and stem-cell transplantation because of age ($\geq$ 65 years) and/or coexisting conditions [33]. In this study, the patients were randomized to treatment with melphalan and prednisone with or without bortezomib (bortezomib, Johnson &

Johnson Pharmaceutical R&D and Millennium). Measurable disease was defined as the presence of quantifiable M-protein in serum or urine, or measurable soft-tissue or organ plasmacytomas. Treatment was given for 54 weeks (9 cycles) unless discontinued earlier upon withdrawal of the patient's consent, disease progression, or the occurrence of unacceptable toxic side effects.

The 682 patients were randomly assigned to receive nine 6-week cycles of melphalan (at a dose of 9 mg per square meter of body-surface area) and prednisone (at a dose of 60 mg per square meter) on days 1, 2, 3, and 4 of each cycle. The two arms differed in the additional administration of bortezomib: patients in one arm received only melphalan and prednisone, while patients in the other arm received, in addition, bortezomib at a dose of 1.3 mg per square meter. Bortezomib was administered on days 1, 4, 8, 11, 22, 25, 29, and 32 of cycles 1 to 4 and on days 1, 8, 22, and 29 of cycles 5 to 9. The dose of melphalan, prednisone or bortezomib was reduced if there was any pre-specified hematologic toxic effect of grade 3 or 4, or a non-hematologic toxic effect. For both arms, treatment was administered for a maximum of 9 cycles (54 weeks) and was discontinued upon disease progression, treatment-related toxicity, or withdrawal of consent. All study medication was supplied from a central source by the study sponsor.

Blood samples were collected for each patient every three weeks (at day 1 and day 22 of each 6-week cycle) for the entire duration of the treatment, i.e. 54 weeks after the date of randomization. In addition, blood samples were collected every eight weeks after treatment completion until the development of confirmed progressive disease. For patients who discontinued treatment before the 54-week time period was completed, blood samples were obtained every three weeks until the end of the 54-week time period, and every eight weeks thereafter. All blood samples for serum M-protein electrophoresis were analyzed in a central laboratory (Covance).

Of the 682 randomized patients, 668 were evaluable for response in the trial (i.e., they had baseline measurable disease and were treated with at least one dose of study drug). Of those, there were 604 patients with heavy chain MM (measurable levels of M-protein IGG, IGA, IGM, or IGD by serum protein electrophoresis) who were included in this analysis. Patients with light chain disease (n = 54) or only measurable plasmocytomas (n = 10) were not included in the modeling. Of those 604 patients, 301 were randomized to the control arm and were administered only melphalan and prednisone (referred to as the VISTA MP cohort), while 303 were randomized to the case arm and were treated with melphalan, prednisone and bortezomib (referred to as the VISTA VMP cohort). Two patients from the VISTA MP cohort and 3 patients from the VISTA VMP cohort were excluded from further analysis due to early treatment discontinuation (melphalan or prednisone) or treatment crossover. We thus obtained 299 patients in the VISTA MP cohort and 300 patients in the VISTA VMP cohort.

VMP with or without CNTO328 trial

VMP with or without CNTO328 trial is a randomized, open-label, phase II study, consisting of 118 newly diagnosed patients, treated either bortezomib-melphalan-prednisone with siltuximab (SVMP, n=64, 12 from the safety cohort + 52 from the efficacy cohort) or bortezomib-melphalan-prednisone alone (VMP, n=54) 2. The primary objectives for this study are: 1) assessing the safety of SVMP, 2) assessing the efficacy of SVMP. For the purpose of assessing efficacy, patients were randomized based on a 1:1 ratio to either SVMP or VMP, and were treated up to a maximum of 9 cycles (54 weeks). For the VMP cohort, patients received nine 6-week cycles of oral melphalan 9 mg/m2 and oral prednisone 60 mg/m2, days 1 to 4, in combination with intravenous bortezomib 1.3 mg/m^2 on days 1, 4, 8, 11, 22, 25, 29, and 32 during cycles 1 to 4; days 1, 8, 22, and 29 during cycles 5 to 9. For the SVMP cohort, patients received siltuximab at 11 mg/kg every 3 weeks by intravenous infusion. Blood and 24-hour urine samples were collected every 3 weeks during the 54-week treatment period then at every 9 weeks interval until progression; M-protein analyses were performed by a central laboratory.

Of the 106 randomized patients (efficacy cohorts), 105 were evaluable for response in the trial (i.e., they had baseline measurable disease and were treated with at least one dose of study drug). Of those, there were 90 patients with single heavy chain MM (measurable levels of

M-protein IGG and IGA by serum protein electrophoresis) who were included in this analysis. Patients with light chain disease (n=13) or biclonal heavy chain disease (n=2) were removed. Of those remaining 90 patients, 43 were randomized to SVMP cohort and 47 were randomized to VMP cohort. The 12 patients in the safety cohort are not analyzed since these patients were not randomized.

APEX trial

The Assessment of Proteasome Inhibition for Extending Remission (APEX) trial is a randomized, open-label, phase III study, consisting of 669 relapsed MM patients with measurable progressive disease after one to three previous treatments3. In this study, patients were randomized to either an intravenous bolus of bortezomib or high-dose dexamethasone.

The 669 patients were randomized by strata based on the number of previous treatments (1 vs. ¿1), time to progression after the last treatment (≤6 months vs. ¿6 months), and 2-microglobulin values (≤2.5 mg per liter vs. ¿2.5 mg per liter), to either intravenous bolus of bortezomib (at a dose of 1.3 mg per square meter of body-surface area) on day 1, 4, 8, and 11 of cycles 1 through 8 (21-day cycles) and on days 1, 8, 15, and 22 of cycles 9 to 11 (35-day cycles) for a maximum treatment period of 273 days, or oral dexamethasone (40 mg) on days 1 to 4, 9 to 12, and 17 to 20 of cycles 1 through 4 (35-day cycles) and on days 1 to 4 of cycles 5 through 9 (28-day cycles), for a maximum treatment period of 280 days. Platelet and red cell transfusions and the administration of neutrophil growth factors and epoetin alpha were allowed. All patients received bisphosphonates intravenously every three to four weeks unless such treatment was clinically contraindicated.

Patients were evaluated every 3 weeks during the first 39 weeks. Follow-up was then performed every six weeks until disease progression, after which follow-up for skeletal events and survival was performed every three months. Patients with a complete response continued to receive treatment for two cycles after the confirmation of the response. Patients who discontinued treatment before disease progression were followed every 3 weeks for 39 weeks or until disease progression. All assessments of M protein were confirmed at a central laboratory.

Of the 669 randomized patients, 624 were evaluable for response in the trial (i.e., they had baseline serum M-protein measurements and were treated with at least one dose of the study drug). Of these, there were 538 patients with heavy chain MM (measurable levels of M-protein IGG, IGA, IGM, or IGD by serum protein electrophoresis) who were included in this analysis. Patients with light chain or non-secretory (n=86) disease were excluded. Of the remaining 538 patients, 269 were randomized to receive bortezomib (Velcade®, referred to as the APEX VEL cohort) and 269 were randomized to receive dexamethasone (referred to as the APEX DEX cohort).

2.3.2 Statistical analysis

We first aimed to investigate the presence of general trends within the treatment response data in each of the six cohorts from the three trials. We performed this investigation both at individual patient level and at whole cohort level.

Patient-level analysis

For each patient, we used the M-protein data, starting from the baseline value obtained before the initiation of therapy until the end of follow-up, to fit four statistical models. The aim of this model fitting was to identify the model with the best fit. The set of models investigated comprised a single-phase exponential curve, a 2-phasic exponential curve with a turning point, a 3-phasic exponential curve with two turning points, and a 4-phasic exponential curve with three turning points. These models were chosen since the goal of this study was to investigate the dynamics of treatment response of MM cells through the analysis of serum M-protein levels, and since any cell population is expected to decrease (or increase) at an exponential rate. Furthermore, visual inspection suggested that overall, the data of most patients displayed at most four slopes.

When fitting these four models to each individual patient's data, we first performed a logarithmic transformation of the original data and then fit a linear, 2-phasic linear, 3-phasic linear, or 4-phasic linear model to the transformed data. For data points for which the M-protein level was below the threshold for quantification, a value of 0.05 g/dl was used in the model, since a value of zero does not allow logarithmic transformation and 0.05 g/dl represents the upper level of detectability in the central laboratory. In the following, a linear model refers to a model applied to the logarithmically transformed data.

For each patient, the data of the M-protein measurements over time was of the format (t_1, y_1), ..., (t_n, y_n), where time points were enumerated as $t_1 < ... < t_n$, and the corresponding M-protein values were given as $y_1, ..., y_n$. A piecewise linear model with k turning points can be written as

$$E(y) = \beta_0 + \beta_1 t + \delta_1 (t - \tau_1) I_{(t>\tau_1)} + ... + \delta_k (t - \tau_k) I_{(t>\tau_k)} \tag{2.1}$$

Here I represents the indicator function. The parameters $\tau_1, ..., \tau_k$ are the turning points between the piecewise linear segments. The parameters β_0 and β_1 determine the slope and intercept of the first segment of the fitted model. Finally, the parameters $\delta_1, ..., \delta_k$ determine the additional slopes of the remaining segments of the fitted model; for instance, for a 2-phasic model, the first slope is given by β_1 while the second slope is given by $\beta_1 + \delta_1$. The piecewise linear model with k = 0, 1, 2, and 3 turning points corresponds to the single-phasic, 2-phasic, 3-phasic and 4-phasic linear model, respectively. To determine the best fitting model, among the four models, for each individual patients, we used the join point software, which is publicly availability through National Cancer Institute [42]. For each model with k turning points, we estimated a total of $2 + 2k$ parameters, for parameter estimation, we utilized Hudson's Method, [43], as it provides more accurate estimates compared to the Grid Search method [42], even though it is computationally more expensive. For the three trials, we applied the approach to determine the best fitting model for each patient, the parameter estimates are listed in Tables 2.1, 2.2 and 2.3. Based on the observation that the major of patients in all three trials display either 1- or 2- phasic patterns, we further investigated 1- and 2- phasic M-protein decline trends for patients with more than 4 data points while on treatment, shown in Tables 2.4, 2.5 and 2.6.

Cohort-level analysis

We then investigated the best fitting model for the entire patient cohort. The data was of the form (t_{ij}, y_{ij}), $i = 1, ..., N$ and $j = 1, ..., n_i$, where i is the patient-specific index; N is the total number of patients, and n_i is the total number of data points for patient i. The two models under consideration are equation (2.2) the single-phasic model and equation (2.3) the bi-phasic model:

$$E(y_{ij}) = a_i + b_i t_{ij} \tag{2.2}$$

$$E(y_{ij}) = a_i + b_i t_{ij} + \delta_i (t_{ij} - \tau_i) I_{(t_{ij} > \tau_i)} \tag{2.3}$$

For each model, the total sum of squared errors (SSE) and total sum of squares (SST) are calculated, as $\sum\limits_{i}^{N} SSE_i$ and $\sum\limits_{i}^{N} SST_i$ across all patients. At individual patient level, the R_i^2 is calculated as $R_i^2 = 1 - \frac{SSE_i}{SST_i}$; and at cohort level, the total R^2 is calculated as $R^2 = 1 - \sum\limits_{i}^{N} SSE_i / \sum\limits_{i}^{N} SST_i$. We used the Bayesian information criterion to determine the best fitting model for a entire cohort, while accounting for difference in model complexity [44]:

$$BIC = log(\frac{SEE_k}{\sum\limits_{i=1}^{N} n_i}) + \frac{p_k}{\sum\limits_{i=1}^{N} n_i} log(\sum_{i=1}^{N} n_i) \tag{2.4}$$

where, k denotes the number of piecewise segments, with $k = 0$ denoting single-phasic model and $k = 1$ denoting bi-phasic model, respectively; and p_k denotes the number of parameters, with $p_0 = 2$ and $p_1 = 4$, for single- and bi- phasic models respectively. Estimates are listed in Tables 2.7. These results suggest that the bi-phasic model is the best fitting model for all six cohorts from the three trials. Thus, we fitted a bi-phasic model to each patient, estimates shown in Table 2.8.

Table 2.1: Summary statistics of the estimated slopes and turning points for the VISTA trial.

Slopes and turning points	Mean (standard deviation)	Median (standard deviation)
VISTA trial MP cohort		
First slope, β_1	-0.0055 (0.0094)	-0.0024 (272)
Second slope, β_2	0.0003(0.0097)	0.0002(168)
Third slope, β_3	0.0022(0.0172)	0.0017(67)
Fourth slope, β_4	0.0036(0.0077)	0.0032(18)
First turning point, τ_1	197.7(132.0)	158.2(168)
Second turning points,	339.4(136.2)	335.0(67)
Third turning points,	410.0(85.4)	401.5(18)
VISTA trial VMP cohort		
First slope, β_1	-0.0222(0.0218)	-0.0172(263)
Second slope, β_2	-0.0010(0.0134)	0.000(104)
Third slope, β_3	0.0053(0.0239)	0.0029(104)
Fourth slope, β_4	0.0005(0.0153)	0.0018(31)
First turning point, τ_1	126.6(92.1)	98.4(234)
Second turning points, τ_2	353.8(171.7)	335.4(104)
Third turning points, τ_3	443.8(155.7)	393.0(31)

Table 2.2: Summary statistics of the estimated slopes and turning points for the CNTO 328 trial.

Slopes and turning points	Mean (standard deviation)	Median (standard deviation)
CNTO 328 trial VMP cohort		
First slope, β_1	-0.0247 (0.0216)	-0.0178 (41)
Second slope, β_2	-0.0082(0.0221)	-0.0008(40)
Third slope, β_3	0.0082(0.0264)	0.0022(21)
Fourth slope, β_4	0.0102(0.0124)	0.0095(6)
First turning point, τ_1	126.0(91.66)	102.3(40)
Second turning points,	285.4(115.4)	257.3(21)
Third turning points,	420.6(161.2)	463.7(6)
CNTO 328 trial SVMP cohort		
First slope, β_1	-0.0500(0.0541)	-0.0281(40)
Second slope, β_2	-0.0068(0.0272)	0.000(34)
Third slope, β_3	0.0078(0.0282)	0.0014(16)
Fourth slope, β_4	0.0079(0.0181)	0.0132(8)
First turning point, τ_1	91.0(64.9)	64.7(34)
Second turning points, τ_2	290.7(152.8)	64.7(34)
Third turning points, τ_3	439.7(153.3)	465.6(8)

Table 2.3: Summary statistics of the estimated slopes and turning points for the APEX trial.

Slopes and turning points	Mean (standard deviation)	Median (standard deviation)
APEX trial DEX cohort		
First slope, β_1	-0.0059 (0.0120)	-0.0037 (206)
Second slope, β_2	0.0076(0.0110)	0.0045(85)
Third slope, β_3	0.0165(0.044)	0.0032(6)
Fourth slope, β_4	-	-
First turning point, τ_1	78.7(40.1)	72.4(85)
Second turning points,	181.1(82.5)	144.8(6)
Third turning points,	-	-
APEX trial VEL cohort		
First slope, β_1	-0.0142(0.0241)	-0.0085(229)
Second slope, β_2	-0.0004(0.0168)	0.0003(119)
Third slope, β_3	0.0191(0.0282)	0.0099(23)
Fourth slope, β_4	0.0060(0.0055)	0.0069(3)
First turning point, τ_1	71.7(51.5)	62.6(119)
Second turning points, τ_2	153.8(85.0)	135.0(23)
Third turning points, τ_3	155.8(40.2)	140.0(3)

Table 2.4: Summary statistics of the estimated 1- and 2- phasic slopes and turning points for the VISTA trial.

Slopes and turning points	Mean (standard deviation)	Median (standard deviation)
VISTA trial MP cohort		
Single-phasic patients		
Slope, β	-0.0025(0.0047)	-0.0015(153)
Bi-phasic patients		
First slope, β_1	-0.0101(0.0108)	-0.0073(102)
Second slope, β_2	-0.0014(0.0247)	-0.0003(102)
Turning point, τ	127.7(75.3)	111.4(102)
VISTA trial VMP cohort		
Single-phasic patients		
Slope, β	-0.0100(0.0099)	-0.0073(55)
Bi-phasic patients		
First slope, β_1	-0.0253(0.0229)	-0.0201(194)
Second slope, β_2	0.0000(0.0117)	0.0000(194)
Turning point, τ	109.6(71.2)	89.6(194)

Table 2.5: Summary statistics of the estimated 1- and 2- phasic slopes and turning points for the CNTO 328 trial.

Slopes and turning points	Mean (standard deviation)	Median (standard deviation)
CNTO 328 trial VMP cohort		
Single-phasic patients		
Slope, β	-0.0056(0.0058)	-0.0048(4)
Bi-phasic patients		
First slope, β_1	-0.0197(0.0156)	-0.0157(36)
Second slope, β_2	-0.0080(0.0200)	-0.0001(36)
Turning point, τ	153.2(76.7)	134.3(36)
CNTO 328 trial SVMP cohort		
Single-phasic patients		
Slope, β	-0.0053(0.0072)	-0.0032(8)
Bi-phasic patients		
First slope, β_1	-0.0637(0.0586)	-0.0391(30)
Second slope, β_2	-0.0019(0.0069)	0.0000(30)
Turning point, τ	104.4(75.7)	82.8(30)

Table 2.6: Summary statistics of the estimated 1- and 2- phasic slopes and turning points for the APEX trial.

Slopes and turning points	Mean (standard deviation)	Median (standard deviation)
APEX trial DEX cohort		
Single-phasic patients		
Slope, β	-0.0037(0.0074)	-0.0020(94)
Bi-phasic patients		
First slope, β_1	-0.0169(0.0142)	-0.0129(49)
Second slope, β_2	0.0056(0.0055)	0.0041(49)
Turning point, τ	83.5(44.6)	74.7(49)
APEX trial VEL cohort		
Single-phasic patients		
Slope, β	-0.0051(0.0091)	-0.0020(83)
Bi-phasic patients		
First slope, β_1	-0.0285(0.0244)	-0.0219(85)
Second slope, β_2	0.0049(0.0116)	0.0015(85)
Turning point, τ	69.8(33.3)	65.3(85)

Table 2.7: Best fitting model for a cohort of patients.

	1-phasic model	2-phasic model	1-phasic model	2-phasic model
	VISTA MP		VISTA VMP	
Min R_i	0.000	0.089	0.002	0.174
25% R_i	0.327	0.678	0.374	0.874
Median R_i	0.629	0.865	0.645	0.929
Mean R_i	0.572	0.787	0.577	0.889
75% R_i	0.847	0.938	0.813	0.962
Max R_i	0.980	0.999	0.955	1.000
R	0.706	0.902	0.642	0.910
BIC	-978.9	-1096.8	-480.5	-773.1
	CNTO 328 VMP		CNTO 328 SVMP	
Min R_i	0.007	0.684	0.003	0.187
25% R_i	0.444	0.872	0.350	0.876
Median R_i	0.630	0.926	0.399	0.948
Mean R_i	0.573	0.912	0.473	0.883
75% R_i	0.731	0.968	0.773	0.968
Max R_i	0.938	0.999	0.950	1.000
R	0.640	0.929	0.471	0.934
BIC	-241.5	-313.9	-214.8	-309.5
	APEX DEX		APEX VEL	
Min R_i	0.000	0.054	0.000	0.228
25% R_i	0.105	0.716	0.195	0.828
Median R_i	0.370	0.846	0.529	0.937
Mean R_i	0.404	0.799	0.498	0.873
75% R_i	0.684	0.944	0.777	0.983
Max R_i	0.964	1.000	0.996	1.000
R	0.496	0.830	0.580	0.898
BIC	-1201.4	-1402.5	-1376.1	-1729.7

Table 2.8: Cohort-level parameters

Cohorts	Slope 1, β_1	Slope 2, β_2	Turning point, τ
VISTA MP	-0.0067	-0.0011	116.20
VISTA VMP	-0.0237	-0.0016	106.2
CNTO 328 VMP	-0.0192	0.0004	151.5
CNTO 328 SVMP	-0.0530	0.0014	106.6
APEX DEX	-0.0169	0.0037	67.1
APEX VEL	-0.0285	0.0034	70.1

2.3.3 Mathematical model

The differentiation hierarchy model

Our mathematical model considers the differentiation hierarchy of hematopoietic cells. In the normal differentiation hierarchy, stem cells reside on top of the hierarchy and give rise to progenitor cells, which produce differentiated cells. In the Multiple Myeloma (MM) differentiation hierarchy, there are MM progenitor cells, which give rise to MM differentiated cells. The abundances of normal stem cells, progenitors and differentiated cells are given by x_0, x_1 and x_2, while the abundances of MM progenitor cells and MM differentiated cells are given by y_1 and y_2 . Normal stem and progenitor cells as well as MM progenitor cells do not secret the monoclonal (M-)protein while MM differentiated cells do. Although normal plasma cells also secret M-protein, their contribution to the rate of M-protein production is small enough such that it can be neglected; otherwise, healthy individuals would test positive for M-protein. The M-protein abundance secreted by MM cells is given by z. Normal stem cells divide at the rate r_x per day. The rate constants for the production of progenitors and differentiated cells are given by a and b, with the appropriate suffixes to distinguish between normal and MM cells. Normal stem cells die at rate d_0, progenitors at rate d_1, and differentiated cells at rate d_2 per day. MM progenitor cells and differentiated cells die at rates δ_1 and δ_2 per day, respectively. M-protein are depleted at rate δ_3 per day. Cells at all levels are assumed to potentially reproduce symmetrically and/or asymmetrically; the limited replication potential of more differentiated cell types is then considered as part of the differentiation rates. We assume that there is a slow clonal expansion of MM progenitor cells. This assumption is made since otherwise, MM progenitor cells would not be able to make up a significant fraction of the progenitor cell compartment at diagnosis. Furthermore, as compared to normal cells, there is an increased rate at which MM differentiated cells are produced. The basic model is given by

$$\begin{array}{ccc}
 & \text{Normal} & \text{Myeloma} \\
\text{Stem cells} & \dot{x}_0 = [r_x \varphi_{x_0} - d_0]x_0 & \\
\text{Progenitor cells} & \dot{x}_1 = a_x \varphi_{x_1} x_0 - d_1 x_1 & \dot{y}_1 = [a_y \varphi_{y_1} - \delta_1] y_1 \\
\text{Differentiated cells} & \dot{x}_2 = b_x x_1 - d_2 x_2 & \dot{y}_2 = b_y y_1 - \delta_2 y_2 \\
\text{M-protein} & - & \dot{z} = c_y y_2 - \delta_3 z
\end{array} \tag{2.5}$$

Here, $\varphi_{x_0} = [1 + \rho_{x_0} x_0]^{-1}$, $\varphi_{x_1} = [1 + \rho_{x_1}(x_1 + y_1)]^{-1}$ and $\varphi_{y_1} = [1 + \rho_{y_1}(x_1 + y_1)]^{-1}$ denote the density dependence terms.

Density dependence for normal stem cells is achieved by the function $\varphi_{x_0} = [1 + \rho_{x_0} x_0]^{-1}$. Density dependences for normal and MM progenitors are achieved through the density dependence terms $\varphi_{x_1} = [1 + \rho_{x_1}(x_1 + y_1)]^{-1}$, and $\varphi_{y_1} = [1 + \rho_{y_1}(x_1 + y_1)]^{-1}$. These functions take into account cell crowding, limited resources, and interactions with the microenvironment. In the absence of MM cells, the differentiation hierarchy of normal cells is in equilibrium, i.e. the abundances and proportions of different cell types do not change. Once the first MM progenitor cell arises, it produces MM differentiated cells, which in turn secrete M-protein. We assume that MM progenitors and differentiated cells have increased production rates as compared to their normal counterparts, $a_y > a_x$ and $b_y > b_x$. We consider that diagnosis occurs and treatment initiates when the MM differentiated cell burden reaches the same level as the normal differentiated cells. Chemotherapy acts by increasing death rates. The half-life of M-protein is not affected by treatment to a large extent. These effects result in distinct phases of treatment response: (i) the first phase, with an exponential slope of -δ_2, corresponds to the decline of differentiated MM cells; this slope has an average of $\delta_2 = -0.0067$ per day for patients treated with VISTA MP and $\delta_2 = -0.0237$ per day for patients treated with bortezomib in addition to VISTA MP; and (ii) the second phase, with a slope of $-l \approx a_y \varphi_{y_1} - \delta_1$, signifies the depletion of MM progenitors; this slope is about $-l = -0.0011$ per day for patients in the VISTA MP cohort and $l = -0.0016$ per day for patients treated with bortezomib in addition to VISTA MP. The second slope of depletion, $-l$, in fact depends on the density dependence term; the resulting non-linearity leads to the system not being able to be solved exactly. However, during the time of treatment, there is little variation in the density dependence term. We have therefore assumed it to be constant.

The model represents the kinetically dominant subpopulations in the hematopoietic differentiation hierarchy; in reality, this hierarchy includes a larger number of distinct differentiation levels. However, for the purposes of explaining the chemotherapy response dynamics, only three populations for normal cells and two populations for MM cells are necessary to include in the simplest possible mathematical model. Similarly, if each subpopulation consists of many clones of the same differentiation stage, which may have distinct growth, differentiation, and death kinetics, then the predictions of the model with regard to the question addressed in this paper does not change significantly. The model then describes the dominant clone within the respective subpopulation at any time.

The clonal evolution model

The above mathematical framework assumes a differentiation hierarchy of the MM cell system. An alternative hypothesis is that instead of the MM differentiation hierarchy, there are genetically different MM clones in the system. This model is given by

$$\begin{array}{rcrc} & \text{Normal} & & \text{Myeloma} \\ \text{Progenitor cells} & \dot{x}_0 = [r_x\varphi_{x_0} - d_0]x_0 & \text{MM clone1} & \dot{y}_1 = [r_1 - d_1]y_1 \\ & - & \text{MM clone2} & \dot{y}_2 = [r_2 - d_2]y_2 \\ & - & \text{M-protein} & \dot{z} = r(y_1 + y_2) - dz \end{array} \tag{2.6}$$

where, $\varphi_0 = [1 + \rho_{x_0} x_0]^{-1}$ denotes the density dependence terms.

In this alternative mathematical model, the abundance of normal cells are given by x_0 and the abundance of MM cells in the two MM clones is denoted as y_1 and y_2, respectively. The rate constants for the production and death rates of cells are given by r and d, with the appropriate suffixes for each cell type. We assume that MM cells in both MM clones produce M-protein at the same rate. We then conducted simulations to investigate whether this model could recapitulate the observed VISTA trial data.

The simulations were conducted in the following way. We solved the ordinary differential equation system to obtain an explicit form of the M-protein value. Let C_1 and C_2 be the number of MM cells in clone 1 and clone 2 when treatment starts; let Z_0 be the M-protein baseline level at treatment initiation. We then obtained the level of M-protein values over time during treatment as $Z(t) = A_1 e^{a_1 t} + A_2 e^{a_2 t} + A_3 e^{-dt}$, where, $A_1 = rC_1/(a_1 + d)$, $A_2 = rC_2/(a_2 + d)$ and $A_3 = Z_0 - A_1 - A_2$ where, $a_1 = r_1 - d_1$ and $a_2 = r_2 - d_2$. We analyzed the treatment response of 249 VISTA VMP patients who had sufficiently many data points (5 or more) and compared, for each patient, the best fitting model (1-phasic or 2-phasic exponentials models). We found that 55 out of 249 patients had the 1-phasic model as the best fitting model while 194 had the 2-phasic as the best fitting model. We also obtained the estimates of first and second slopes as well as the turning points of the 83 2-phasic patients whose had both negative first and second slopes of M-protein depletion. In the simulation of the alternative mathematical model, we simulated M-protein data during treatment of 249 patients. For each patient, we randomly sampled a pair of M-protein depletion rates (a_1, a_2) from the estimated rates of the above 83 VISTA VMP patients in the VISTA trial. We then randomly simulated a M-protein baseline value Z_0 for each simulated case from the VISTA baseline values for VISTA VMP patients. For the initial number of cells in the two clones (C_1 and C_2), we chose their sum to be 10^5 and chose the value of the less frequent clone (clone 2) from a power-law distribution [45]. This choice was made since clone 1 was considered to produce clone 2 by the accumulation of a specific (epi)genetic change, and the number of cells in such a new clone, when the total number of cells (including both clones) reaches a certain size is given by a power law distribution [45]. To be specific, we chose a power law distribution with cumulative density function $F(y) = 1 - (y/L)^{-\alpha+1}$with parameters $L = 1$ and $\alpha = 1.1$. The production rate of M-protein was given by $r = dZ_0/(C_1 + C_2)$ and its depletion rate by $d = 0.08$. Furthermore, we added a noise term generated from a normal distribution with mean 0 and standard deviation 0.1. With the chosen parameters and added noise, we obtained, for each case, the M-protein values during treatment every 22 days for up to a year. Any M-protein value below 0.05 was considered as below detection baseline and was replaced by 0.05 for the following statistical analysis.

After obtaining the simulated data of 249 cases through the above process, we compared for each case the best fitting model between 1-phasic and 2-phasic exponential models. In one simulation iteration, we obtained 113 cases whose best-fitting model was the 1-phasic model while the remaining 136 displayed a better fit with the 2-phasic model. In the VISTA trial, these numbers were 55 (1-phasic) versus 194 (2-phasic). There was a significant difference in the numbers of

1-phasic and 2-phasic patients between the observed clinical data in the VISTA trial and the simulated data based on the alternative mathematical model ($p = 5 \times 10^{-8}$, Fisher's exact test). Furthermore, the estimated turning points for 2-phasic patients with both negative first and second slopes were significantly different between the observed clinical data in the VISTA trial and the simulated data based on the alternative mathematical model (90±69, median 72 days in VISTA data; 186±81, median 169 days in simulated data; $p = 2 \times 10^{-12}$, two-sample t-test). In the simulated data, fewer cases had 2-phasic trends and for those 2-phasic cases, the turning points occurred much later compared with what we observed in the VISTA trial. The simulation results were consistent when we repeated the above simulation to investigate its robustness regarding the stochasticity in choosing slopes from VISTA patients as well as the number of cells in clone 2. We did not repeat the analysis for patients of the VISTA MP cohort since the results are expected to be very similar. Thus the alternative mathematical framework considering genetically different MM clones was unable to recapitulate the VISTA trial data.

The hybrid model

To explain the early rebound of M-protein values before the termination of treatment in the refractory patients, we then proposed a model combining both the MM differentiation hierarchy model and the clonal evolution model. This model is given by

$$\begin{array}{cccc}
 & \text{Normal} & \text{MM clone 1} & \text{MM clone 2} \\
\text{Stem cells} & \dot{x}_0 = [r_x \varphi_{x_0} - d_0] x_0 & & \\
\text{Progenitor cells} & \dot{x}_1 = a_x \varphi_{x_1} x_0 - d_1 x_1 & \dot{y}_1 = [a_y \varphi_{y_1} - \delta_1] y_1 & \dot{z}_1 = [a_z \varphi_{z_1} - \Delta_1] z_1 \\
\text{Differentiated cells} & \dot{x}_2 = b_x x_1 - d_2 x_2 & \dot{y}_2 = b_y y_1 - \delta_2 y_2 & \dot{z}_2 = b_z z_1 - \Delta_2 z_2 \\
\text{M-protein} & - & \dot{M}_s = c_y y_2 - \delta_3 M_s & \dot{M}_r = c_z z_2 - \Delta_3 M_r \\
\text{Overall M-protein} & & \multicolumn{2}{c}{M = M_s + M_r}
\end{array} \tag{2.7}$$

Here, $\varphi_{x_0} = [1 + \rho_{x_0} x_0]^{-1}$, $\varphi_{x_1} = [1 + \rho_{x_1}(x_1 + y_1)]^{-1}$, $\varphi_{y_1} = [1 + \rho_{y_1}(x_1 + y_1 + z_1)]^{-1}$, and $\varphi_{z_1} = [1 + \rho_{z_1}(x_1 + y_1 + z_1)]^{-1}$ denote the density dependence terms.

This model is analogous to the original differentiation hierarchy model, with the addition of a resistant clone. The dynamics of this system depends on the relative frequencies of the two clones, which is controlled by the time at which mutation arises. For small z_1, MM clone 1 cells determine the treatment response, as these M-protein trajectories are observed in the newly diagnosed patients; as treatment continues, MM clone 2 slowly expands. However, given the small number of clone 2 progenitor cells at the beginning of the first treatment, clone 2 cells are not sufficiently abundant to drive the rebound of M-protein values after the termination of the initial treatment. However, after multiple rounds of treatment, clone 2 reaches dominance and may result in a rebound even before the termination of treatment. Clones 1 and 2 may also be referred to as "sensitive" and "resistant" MM clones.

Ancillary parameters for the hierarchy model and the hybrid model

The mathematical model proposed is a highly parameterized model; besides the estimated parameter values for the first and second slopes, a list of ancillary parameters are required for the prediction of the M protein trajectories. The parameter values for these ancillary parameters are listed here below. The parameter values are selected based on the estimation of multiple myeloma total tumor burden, which is estimated to be on the order of 10^{12}cells [46]. We assume that normal differentiated cells are on the order of 10^{12} cells. Furthermore we assume that the cellular ratio between stem: progenitor: differentiated cells is 1:100:10,000. In addition, The production rate (g/cell/dL) and elimination rate of M-protein (0.07/day) were obtained from experimental measurements [46, 47]. All other parameters, besides the first and second slopes, are selected such that the normal cells are in a state of homeostasis.

where,

$$f_n(x, \delta', \delta) = \begin{cases} \delta' e^{log \frac{\delta}{\delta'} / (365 \times 5) x} \text{ for } 0 \leq x \leq 365 \times 5 \\ \delta \text{ for } x > 365 \times 5 \end{cases} \tag{2.8}$$

Table 2.9: Parameters used in the hierarchical model and the hybrid model during different phases of disease progression and treatment.

Density dependence terms			
$\rho_{x_0} = 5 \times 10^{-7}$	$\rho_{x_1} = 5 \times 10^{-10}$	$\rho_{y_1} = 8 \times 10^{-9}$	$\rho_{z_1} = 8 \times 10^{-9}$
Before treatment			
$r_x = 0.005$		$d_0 = 0.0001$	
$a_x = 0.05$	$a_y = a_z = 0.25$	$d_1 = 0.0001$	$\delta_1 = \Delta_2 = 0.0001$
$b_x = 0.5$	$b_y = b_z = 0.5$	$d_2 = 0.003$	$\delta_2 = \Delta_2 = 0.003$
	$c_y = c_z = 2.2 \times 10^{-13}$		$\delta_2 = \Delta_2 = 0.07$
On-treatment			
$r_x = 0.005$		$d_0 = 0.0001$	
$a_x = 0.05$	$a_y = a_z = 0.25$	$d_1 = 0.0001$	δ_1=slope1-$a_y \varphi_{y_1}$, $\Delta_2 = 0.0001$
$b_x = 0.5$	$b_y = b_z = 0.5$	$d_2 = 0.003$	δ_2=slope2, $\Delta_2 = 0.0001$
	$c_y = c_z = 2.2 \times 10^{-13}$		$\delta_2 = \Delta_2 = 0.07$
Post-treatment			
$r_x = 0.005$		$d_0 = 0.0001$	
$a_x = 0.05$	$a_y = a_z = 0.25$	$d_1 = 0.0001$	$\delta_1 = f_n(x, \text{slope1} - a_y \varphi_{y_1}, 0.0001)$, $\Delta_2 = 0.0001$
$b_x = 0.5$	$b_y = b_z = 0.5$	$d_2 = 0.003$	$\delta_2 = f_n(x, \text{slope2}, 0.003)$, $\Delta_2 = 0.0003$
	$c_y = c_z = 2.2 \times 10^{-13}$		$\delta_2 = \Delta_2 = 0.07$

where, x denotes the number of days once treatment cession, δ and δ' denote the before treatment and on-treatment death rate, respectively. The five-year (365×5) used in the equation (2.8) correspond tot he median survival time of multiple myeloma patients [48].

2.4 Results

For each patient, we investigated several statistical models to identify the model with the best fit to the M-protein data (Methods). When studying the individual dynamics of treatment response in both the VISTA MP and VISTA VMP cohorts, we identified a 2-phasic exponential model to be the best-fitting statistical model for both cohorts (Methods, Table 2.7). The summary statistics for the first slopes (β_1), second slopes (β_2) and turning points (τ) for the VISTA and the APEX trials when fitting 2-phasic exponential models to all patients in each cohort are shown in Table 2.8. First, we found that patients in the VISTA VMP cohort had a significantly steeper first slope on average than patients in the VISTA MP cohort ($p = 3 \times 10^{-15}$ Wilcoxon rank-sum test). Second, for the VISTA trial, the difference between cohorts in terms of the second slopes was not statistically significant (p=0.2439 Wilcoxon rank-sum test) and both cohorts were not significantly different from zero (MP p=0.2645 and VMP p=0.08 t-statistics). Third, the difference between cohorts in terms of the turning point was also not statistically significant (p=0.3852 Wilcoxon rank-sum test).

In addition to the cohort-level analysis described above, we also estimated the bortezomib treatment effect by comparing the treatment response dynamics of patients in the VISTA trial, at an individual patient level, by determining the best piecewise exponential model (1- vs. 2-phasic models) for each patient. First, we found that there was a significantly larger proportion of 2-phasic patients in the VISTA VMP cohort as compared to the VISTA MP cohort ($p \leq 10^{-16}$, Fisher's exact test). Second, 2-phasic patients in the VISTA VMP cohort had a significantly steeper first slope than such patients in the VISTA MP cohort ($p = 3 \times 10^{-15}$ for all patients with β_1¡0, Wilcoxon rank-sum test). The difference between cohorts in the second slope was not statistically significant. Third, 2-phasic patients in the VISTA VMP cohort had a smaller turning point than patients in the VISTA MP cohort (p = 0.02 for all 2-phasic patients with β_1¡0 and $p = 0.01$ for all 2-phasic patients with $\beta_0 < 0$ and $\beta_1 < 0$, Wilcoxon rank-sum test). When investigating the relationship between the best-fitting model and MM stage, we found that patients with advanced-stage disease in the VISTA MP cohort were significantly more likely to display a 2-phasic rather than a 1-phasic exponential trend after the initiation of therapy . For the VISTA VMP cohort, however, there was no significant association between MM stage and the shape of the treatment response curve. In both cohorts, there were more deaths of patients with positive second slopes compared to patients with negative second slopes. Furthermore, for VISTA VMP patients displaying a 2-phasic M-protein depletion in the treatment phase, the first slope was significantly associated with the time to progression (p = 0.005, Cox model) when controlling for MM stage.

The observed 2-phasic M-protein depletion suggests multiple myeloma cellular dynamics is highly complex. To interpret these results in a cell biology-relevant framework, we designed a mathematical model describing the differentiation hierarchy of the hematopoietic system (Methods). This model was created to relate the abundance of M-protein to the numbers of different MM cells. In the context of this model, normal stem cells reside on top of the hierarchy and give rise to progenitor cells, which in turn produce differentiated cells. In addition to normal cells, the bone marrow of MM patients also includes MM cells. Since the statistical analyses above suggested the presence of a 2-phasic exponential depletion of M-protein values over time, we designed a model including two subpopulations of MM cells with distinct growth and differentiation kinetics: progenitors and differentiated cells. In this model, MM progenitors reside on top of the MM hierarchy and give rise to MM differentiated cells, which in turn produce M-protein. MM progenitors produce none or only low amounts of M-protein, which we neglected in the mathematical model (Methods).

This hierarchical mathematical model, together with the estimates of the two slopes obtained with our statistical modeling approach, was then used to predict the kinetics of the treatment response in the VISTA MP and VMP cohorts (Figure 2.1b-e). After treatment initiation, the MM cell population declines at the death rate of differentiated MM cells during therapy (equal to the first slope identified in the data, mean -0.0067 (VISTA MP cohort) and -0.0237 (VISTA VMP cohort)) until the latter reach a steady state with MM progenitor cells; from this time onwards, the kinetics display a shallower decrease signifying the depletion of progenitor cells during treatment (equal to the second slope identified in the data, mean -0.0011 (VISTA MP cohort) and -0.0016 (VISTA VMP cohort)). After treatment discontinuation, some patients show a lasting suppression of their M-protein values, while others experience a disease rebound. In the context of the mathematical model, these patterns are generated by a selective effect of treatment on different MM clones: treatment may select for MM phenotypes with altered growth and differentiation kinetics as compared to the predominant clone present at the time of diagnosis. In patients in whom no rebound occurs by the end of follow-up, the MM clones that remain after treatment are less “fit” (either via a decreased growth rate or an increased death rate) than those present before treatment. Thus, their expansion occurs at a slower time scale, such that the M-protein value slowly increases after treatment cessation but remains below the detection limit. In patients in which a rebound occurs, cells are selected that lead to positive M-protein values after variable periods of time.

We also tested another mathematical model, which postulates the existence of two genetically independent MM clones, i.e. a clonal evolution model (Methods). We found that there was a significant difference in the numbers of 1-phasic and 2-phasic patients between the observed clinical data in the VISTA trial and the simulated data based on the clonal evolution model ($p = 5 \times 10^{-8}$, Fisher's exact test). Furthermore, the estimated turning points for 2-phasic patients were significantly different between the observed clinical data in the VISTA trial and the simulated data based on the clonal evolution model (Methods). Thus, the clonal evolution model, which considers genetically different MM clones, was unable to recapitulate the VISTA trial data.

To validate the hierarchical mathematical model, we utilized data from two independent clinical trials: the CNTO 328 trial comparing bortezomib-melphalan-prednisone (VMP) vs. siltuximab plus VMP (SVMP) in newly diagnosed patients (n=106); and the APEX trial comparing high-dose dexamethasone (DEX) vs. single agent bortezomib (VEL) in refractory patients (n=669). For the two validation data sets, we first applied the same statistical methods as before to estimate the treatment effects. For both CNTO 328 and APEX trials, we found that the cohort-level during treatment M-protein responses are best explained by the 2-phasic exponential model Table 2.7. The summary statistics at the whole cohort-level are shown in Table 2.8. For the CNTO 328 trial, we found that there is a statistically significant different between CNTO 328 VMP and CNTO 328 SVMP in terms of the first slopes (β_1), (p=0.0005, t-test). However, comparing between VISTA VMP and CNTO 328 VMP cohorts, the first slopes are not significantly different (p=0.2082, t-test). Interestingly, although the addition of siltuximab significantly increases the initial reduction of the M-protein levels, the CNTO 328 trial failed in establishing survival benefits [37]. In terms of the second slopes, there is no significant difference between CNTO 328 VMP and SVMP cohorts (p=0.7586, t-test); and both cohorts were not significantly different from zero (VMP p= 0.8953 and SVMP p=0.2123, t-test). For the APEX trial, first we found that patients in the APEX VEL cohort had a significantly steeper first slope than patients in the APEX DEX cohort (p = 0.0035 t-test). Second, the difference between cohorts in terms of the second slope was not statistically significant (p=0.8635 t test). However, unlike the VISTA trial, in the APEX trial the second slopes are significantly positive (DEX p=0.01231 and VMP p=0.001 t-statistics). These increases may signify the development of resistance. In all three trials, patients displayed significant reductions in M-protein levels immediately upon receiving treatments; however, the long-term effects of these

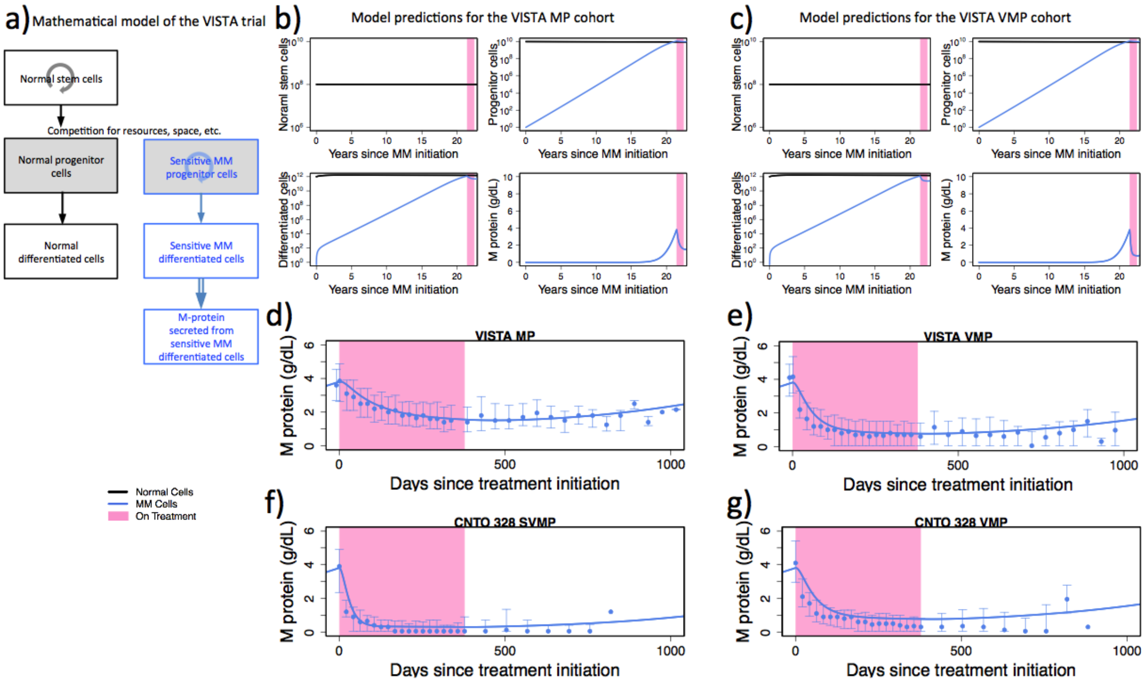

Figure 2.1: The hierarchical mathematical model accurately predicts the dynamics of M-protein response in the VISTA and CNTO 328 trials. (a) Illustration of the hierarchical mathematical model. Normal and MM cells are shown in black and blue, respectively. Solid downward arrows indicate the direction in the differentiation hierarchy. Circular arrows indicate cellular regeneration within each differentiation level. Double-lined arrow indicates M-protein production from differentiated MM cells. (b-c) The panels display the abundance of healthy (black) stem cells, healthy (black) and MM (blue) progenitor cells and differentiated cells over time (years) for the VISTA MP (panel b) and VISTA VMP (panel c) cohorts since the emergence of the first MM cell, as predicted by the mathematical framework (see Methods). The pink shaded region denotes the time during which patients receive treatment. (d-g) Concordance between observed population-level MM protein trajectories and the MM protein levels predicted by the mathematical model. The parameter values for the first and second slopes used to generate panels d), e) and f) are listed in Table 2.9. For panel g) the model predicted trajectory is generated using the same first and second slopes as panel e). All ancillary parameters for panels d)-g) are identical and are listed in Methods.

medications remain less clear.

We then aimed to validate our mathematical model (see Figure 2.1 and Methods) using data from the CNTO 328 and the APEX trials. First, for the CNTO 328 trial, consisting of newly diagnosed patients, the hierarchical model was able to recapitulate the population-level M-protein trajectory. The population-level M protein trajectory for the VMP cohort in the CNTO 328 trial can be recapitulated using the same first and second slope estimates obtained from the VISTA trial, Figure 2.1 e) and g). For the SVMP cohort, the M-protein trajectory can be recapitulated using slope estimates obtained from the SVMP patient data, while keep all other parameters unchanged

Figure 2.1 f) and Table 2.8.

For the APEX trial, we observed increasing trends in M-protein values already during the treatment phase in many patients in the APEX trial at both the cohort and individual patient level; this was not unexpected as the time to myeloma progression is shorter in relapsed multiple myeloma than in newly diagnosed myeloma, and therefore for many patients in the APEX trial, this time fell within the trial-specified treatment duration. First, among patients displaying 1-phasic patterns, more patients in the APEX trial had statistically significant positive slopes, (β_1¿0 and p¡0.05; APEX DEX: 4/94 and APEX VEL: 11/83) than in the VISTA trial (VISTA MP: 3/153 and VISTA VMP: 0/55). Second, for patients displaying 2-phasic patterns in the APEX trial, we observed rebounds (β_2¿0) in the M-protein values during treatment (see Table 2.8). Initially, 2-phasic patients in both trials had similar responses to treatment, as shown by the decline in M-protein values immediately after treatment initiation and the similarity in the magnitudes of β_1. However, the long-term treatment response differed between the APEX and VISTA patients. We observed that, among patients who displayed 2-phasic trends, relapsed patients in the APEX trial were more likely to have statistically significant rebounds (β_2¿0 and p¡0.05; APEX DEX: 22/49 and APEX VEL: 31/85) than the newly diagnosed patients in the VISTA trial (VISTA MP: 19/102 and VISTA VMP: 27/194). In addition, most rebounding patients in the APEX trial had M-protein rebounds within 100 days after the start of treatment, while still on treatment (median: 74.21 days; mean: 83.20; sd: 41.88 for APEX DEX cohort and median: 68.02 days; mean: 69.14; sd: 27.80 for APEX VEL cohort).

Based on these observations in all four trial cohorts, we attribute the differences in M-protein dynamics between newly diagnosed and relapsed patients to the existence and expansion of a resistant clone in the relapsed patients (Figure 2.2 a). A dominant resistant clone existing prior to treatment explains the increasing M-protein values during treatment among 1-phasic patients in the APEX trial; an expanding resistant clone during treatment explains the initial declines followed by increases in M-protein values in the APEX trial; and the presence of a small resistant clone explains continuing 2-phasic declines in the remaining patients (Figure 2.2 b-d). Therefore, we extended our mathematical model to take into account resistant clone(s) (Figure 2.2 a). In this model, in addition to normal cells and sensitive MM cells, there is a resistant clone that originally arose from the sensitive progenitor MM cells. This resistant clone gives rise to a similar differentiation hierarchy as the sensitive cells. The observed M-protein values are the sum of M-protein values generated from the sensitive and resistant clones; the amount of M-protein secreted by each clone is proportional to the size of the clone and the relative secretion rates, which are considered to be similar; this assumption can be relaxed as more data becomes available. The time at which resistance arises determines the relative proportion of sensitive and resistant cells. In newly diagnosed patients, the M-protein contribution from the resistant cells during treatment is negligible; this is supported by the observation that only a relatively small number of patients (7 and 21% in VISTA VMP and MP cohorts, respectively) experienced increases in M-protein values while on treatment in the VISTA trial. In contrast, in the relapsed patients from the APEX trial, due to prior treatment-induced clonal selection, the M-protein contribution from the resistant clone is sufficiently large to alter the treatment response trajectory, leading to rebounds in a subset of patients while on treatment in the APEX trial (Methods). This hybrid model was able to explain the M-protein dynamics for both newly diagnosed and relapsed myeloma patients in response to chemotherapy (Figure 2.1 d-e and Figure 2.2 e-f). Our model suggests that treatment-induced clonal selection may contribute to the increases of the M-protein levels in the refractory patients while on treatment.

2.5 Discussion

Our analysis of newly diagnosed and refractory patient responses to therapy in the VISTA trial revealed complex but structured kinetic patterns that support a two-cell hierarchical model for MM. The proposed model was able to recapitulate the observed two phasic decline patterns observed in the majority of patients. Our model suggests the existence of a MM progenitor cell population that has self-renewal capacity and distinct growth kinetics and gives rise to the differentiated MM cell population. Notably, inter-patient variability of disease kinetics at the time of disease relapse was significant, requiring the adjustment of growth parameters in the model, suggesting that

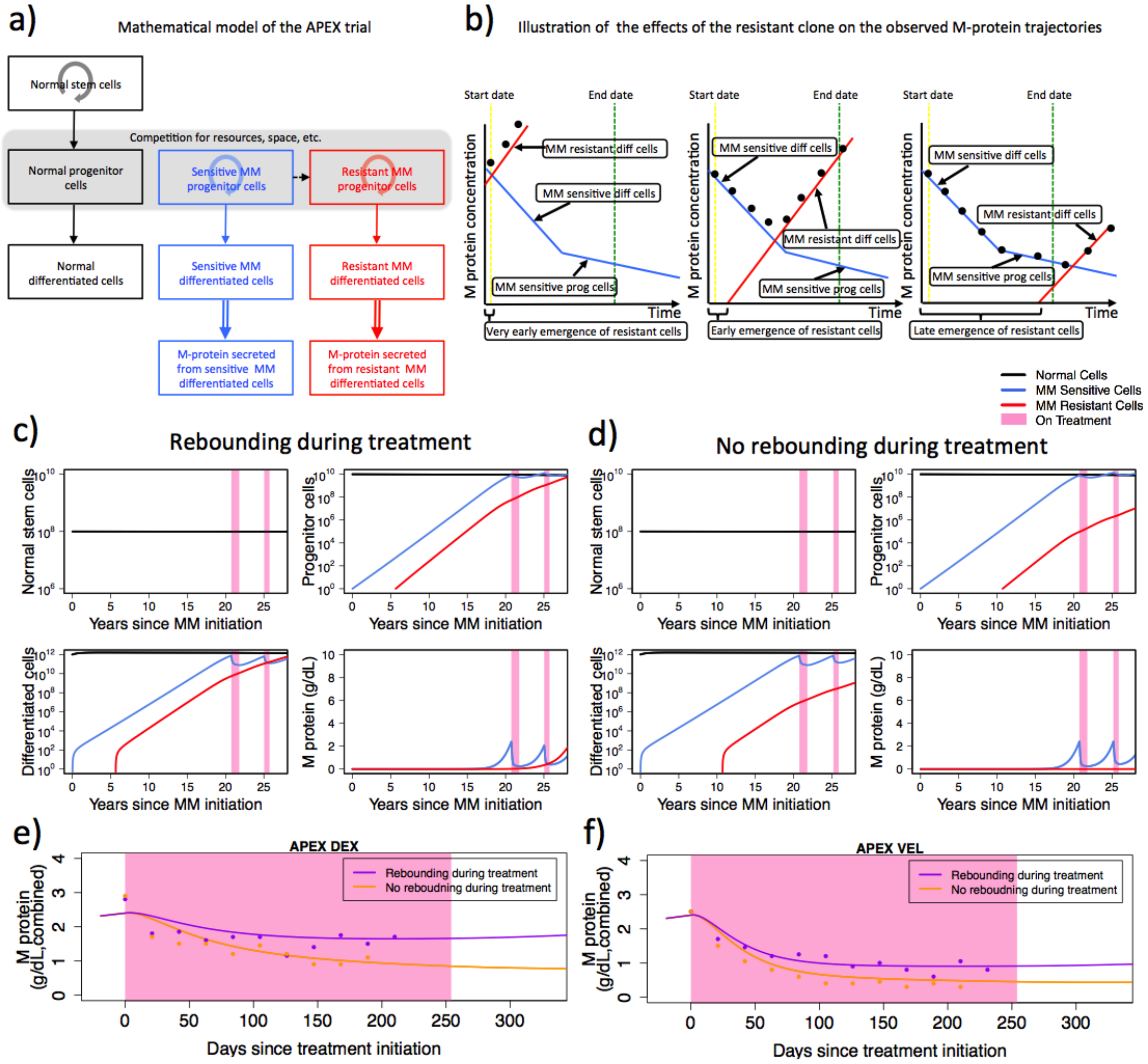

Figure 2.2: The hybrid mathematical model accurately predicts the dynamics of M-protein response in all three trials. (a) Illustration of the hybrid mathematical model. Normal, sensitive and resistant MM cells are shown in black, blue and red, respectively. The dashed arrow indicates the mutation event that gives rise to the first resistant cell. Solid downward arrows indicate the direction in the differentiation hierarchy. Circular arrows indicate cell regeneration within each differentiation level. Double-lined arrow indicates the production of M-protein from differentiated MM cells. (b) Illustration of effects of the time at which resistance arises on the observed M-protein trajectories. Left: resistance emerges very early; middle: resistance emerges early; right: resistance emerges late. The blue lines denote the contribution to the changes in the observed M-protein values of sensitive MM cells; the red lines denote the contribution to the changes in the observed M-protein values of resistant MM cells; and the black dots represent the observed total M-protein levels from both sensitive and resistant MM cells. Although the sensitive cell response to treatment remains identical in all three subpanels, the timing at which resistance arises determines the observed M-protein response. (c-d) The panels display the abundance of healthy (black) stem cells, healthy (black), sensitive MM (blue) and resistant MM (red) progenitor cells and differentiated cells over time (years) for early (c) vs. late (d) emergence of resistance for the APEX DEX cohort, as predicted by the mathematical framework. Panels (c) and (d) have identical parameter values except for the time at which resistance arises. The time at which resistance arises dictates whether rebounds occur during treatment phase. (e-f) M-protein treatment responses are dichotomized based on rebound status for APEX DEX and VEL cohorts. Rebound during treatment (purple): patients with at least one positive slope during the treatment phase; No rebounding during treatment (orange): patients with all negative slope(s) during the treatment phase. Observed median M-protein values (≥10 observations) from each subgroup are shown in dots. Lines show model-predicted M-protein trajectories. Within each cohort, all parameter values are identical, except the time at which resistance arises.

distinct MM progenitor subclones may have been selected by bortezomib treatment. The existence of clonal selection between myeloma subclones was also supported by our analysis of relapsed or refractory patients in the APEX trial. Recent studies [49–51] documented pronounced intra-patient genetic heterogeneity in human neoplasias and attributed disease progression and drug resistance to the differential molecular features of the underlying tumor subclones. Detection of genetic heterogeneity, however, does not preclude the existence of functional heterogeneity within a tumor and its individual clones. Quantification of functional heterogeneity in tumors is technically challenging with experimental methods. Mathematical modeling can address these limitations and provide insights into the relative contribution of genetic versus functional heterogeneity in the behavior of human cancers.

Our data are consistent with reports of clonogenic B-cell ”MM stem cells” isolated from patient samples [41,52]. However, experimental data are divided on whether MM progenitor cells are in fact contained within the CD138- cell compartment [53–55]. Additional surface markers may be needed to identify MM progenitor cells, but alternative biological explanations are also possible. MM progenitors may be a functionally distinct subset of MM cells defined by something other than by markers of normal B-cell maturation, e.g by stromal cell interactions [56,57]. Alternatively, two-phase response kinetics might be explained by yet undefined drug metabolism induced over time (although published pharmacokinetic data on bortezomib are not consistent with this hypothesis [58]), or by the induction of immune or other host responses activated after treatment initiation.

Our model provides a method for testing biological hypotheses directly relevant to disease outcomes in patients with MM. For example, blockade of plasma cell differentiation via suppression of Ire1-Xbp1 pathway in myeloma was recently found to cause resistance to bortezomib treatment [59], a finding that is consistent with our model. The model could be used to iteratively improve new clinical trials through mathematical analyses of treatment effects of specific agents on both differentiated and progenitor cells populations. In addition, our model can be applied to the optimization of myeloma treatment protocols, including the role of multi-drug combinations with complementary effects on differentiated and progenitor cell populations in initial therapy for active disease [60]. As multiple MM clones are present at diagnosis, the administration of rational combination treatments at relapse may reduce their expansion and therefore lead to more favorable outcomes, again an area where the model may have utility [61, 62]. Thus, collecting quantitative data centrally from future clinical trials and using mathematical modeling in various settings of the disease could aid efforts to improve survival for patients with MM overall.

Patterns of Proliferative Activity in the Colonic Crypt Determine Crypt Stability and Rates of Somatic Evolution

Rui Zhao[1,2] and Franziska Michor[1,2]

[1]Department of Biostatistics, Harvard School of Public Health
[2]Department of Biostatistics and Computational Biology, Dana-Farber Cancer Institute

3.1 Summary

Epithelial cells in the colon are arranged in cylindrical structures called crypts in which cellular proliferation and migration are tightly regulated. We hypothesized that the proliferation patterns of cells may determine the stability of crypts as well as the rates of somatic evolution towards colorectal tumorigenesis. Here, we propose a linear process model of colonic epithelial cells that explicitly takes into account the proliferation kinetics of cells as a function of cell position within the crypt. Our results indicate that proliferation kinetics has significant influence on the speed of cell movement, kinetics of mutation propagation, and sensitivity of the system to selective effects of mutated cells. We found that, of all proliferation curves tested, those with mitotic activities concentrated near the stem cell, including the actual proliferation kinetics determined in in vivo labeling experiments, have a greater ability of delaying the rate of mutation accumulation in colonic stem cells compared to hypothetical proliferation curves with mitotic activities focused near the top of the crypt column. Our model can be used to investigate the dynamics of proliferation and mutation accumulation in spatially arranged tissues.

3.2 Introduction

Colorectal cancer is the third most prevalent cancer type for both men and women in the United States, accounting for 9% of all cancer deaths [63]. This large incidence can be partially attributed to the rapid cell divisions that continuously replenish the colonic epithelium, as this large amount of cell turnover increases the risk of accumulating the genetic changes leading to colorectal tumorigenesis [64]. The gene most frequently altered in colorectal cancer is adenomatous polyposis coli (APC), with more than 85 % of all colorectal cancer cases harboring mutations in this gene [65]. APC, a tumor suppressor, is a negative regulator of the b-catenin oncoprotein [66] and mutations in APC lead to elevated levels of β-catenin in the cytoplasm, which in turn induce changes in proliferation, differentiation, migration, adhesion, and apoptosis [67]. Germline APC mutation results in the familial adenomatous polyposis (FAP) syndrome, which is characterized by an early onset of colorectal cancer in almost all afflicted individuals [68]. Other frequently altered genes in colorectal cancer include KRAS [69], the SMAD genes [70], TP53 [71], and MYC [72, 73]. In addition to alterations of oncogenes and tumor suppressor genes, colorectal tumors often display a mutator phenotype, which has been broadly categorized as microsatellite instability (MIN) [74] or chromosomal instability (CIN) [75]. About 15% of sporadic colorectal cancers display MIN, caused by a loss of DNA mismatch repair gene function [74]; the remaining 85% have CIN, characterized by an excessive rate of gaining or losing whole chromosomes or parts of chromosomes, at a rate of up to 10^{-2} per chromosome per cell division [75]. An important feature associated with tumors harboring CIN is the accelerated rate of loss of heterozygosity (LOH), which increases the rate of tumor suppressor gene inactivation. It is not unusual for more than half of the genes in colorectal tumor cells to display LOH [76]. More than one hundred genes associated with CIN have been identified in yeast, many of which have human homologs [77, 78].

In addition to the genetic sequence leading to colorectal cancer, the physical architecture and proliferation kinetics of epithelial cells have also been the topic of many investigations. Epithelial cells in the colon are arranged in cylindrical compartments called crypts [79]. Each crypt contains on average 2,000 cells, with about 40 cells in circumference and 80 cells in height [80]. A small number of stem cells (4-6) are located at the bottom of the crypt [81, 82]. These cells divide to produce the differentiated progenies populating the crypt. The latter cells divide and migrate upward with limited lateral movement and are eventually shed off into the lumen of the large intestine [83]. The proliferation kinetics of cells follows a complex and spatially specific pattern, with proliferating cells concentrated at the bottom half of the crypt, near the stem cells, and the upper half of the crypt consisting of non-dividing migrating cells [80, 84]. This proliferation pattern is tightly controlled, and changes in this pattern have been shown to be associated with the progression towards colorectal cancer [85]. Quantitative measurements in animal models demonstrated that the speed of the upward migration increases from 0.02 cell positions per hour per crypt column at the bottom of the crypt to approximately 1.0 cell positions per hour near the top [86]. Under normal circumstances, the entire crypt is regenerated every 2 to 7 days [64]. Overall, the human colon contains about 10^7 crypts, thus bringing the total number of epithelial cells in the colon to about 2×10^{10} cells.

As experiments involving colonic epithelial cells remain technically challenging or infeasible in humans, several mathe- matical and computational models were developed to enhance our understanding of crypt kinetics and the somatic evolution leading to colorectal cancer. Early work has led to the postulation that colorectal cancer is the result of a sequential accumulation of mutations [87]. ince then, many mathematical models have been proposed to describe the accumulation of mutations leading to colorectal cancer. For instance, some investigators have addressed the effects of tissue architecture on the rate of mutation accumulation in colonic tissues. These studies include the spatially explicit models proposed by Komarova and Wang [88] to investigate the location within the crypt at which APC mutations arise, by Michor et al. to elucidate the time during tumorigenesis at which CIN arises [89], and by Buske et al. to investigate the changes in tissue dynamics resulting from gains or losses of specific gene functions using an agent-based model [90]. In addition, Nowak *et al.* proposed a linear process model to study the speed of somatic evolution in colonic crypts [91]. In this model, N cells within a crypt column are projected onto a one-dimensional grid. During each time step, a cell is selected for reproduction. A cellular division yields two daughter cells, with one daughter occupying the original position and the other daughter residing in the position immediately to the right of the original cell. All cells on the right of the dividing cell move to the right by one position in the grid, and the last cell is shed off into the lumen of the intestine. During each cell division, a mutation may occur with a certain probability; each daughter cell has a chance of 1/2 of inheriting the mutation. Compared to a well-mixed population of cells, this linear process was shown to slow down the speed of somatic evolution and to conceal the selective effects of advantageous mutants [91]. This observation suggests that the cellular architecture of multicellular tissues has the potential to delay the onset of cancer. Several other models were designed to specifically investigate crypt kinetics. Two excellent reviews by van Leeuwen et al. [92] and de Matteis et al. [93] provide an in-depth discussion of these studies: a two-dimensional lattice-based model [94, 95], a one-dimensional lattice-based model with an intraepithelial growth factor gradient [96], a two-dimensional lattice-free model based on Voronoi tessellation [97], and a cellular Potts model (CPM) [98]. Recently, Mirams and Fletcher presented an integrated model incorporating both proliferation kinetics and tissue architecture for investigating mutation fixation within a crypt [99]. Using the number of proliferating cells as a proxy for proliferation kinetics, they showed that the dynamics of cell division have a significant effect on the spread of mutated cells within the population.

Despite these forays, several open questions remain regarding the effects of proliferation kinetics on the rate of mutation accumulation towards colorectal cancer. To address these issues, we developed a spatially arranged stochastic model of the colonic crypt. We investigated several different proliferation kinetics curves, including one quantitatively measured using labeling indices in the normal colonic epithelium [19,23], and their effects on the rate of somatic evolution towards colorectal tumorigenesis. This model contributes to a quantitative understanding of the initiation and progression of colorectal cancer and can be used to investigate the effects of spatial patterns on mutation accumulation.

3.3 Methods

The mathematical model: in order to investigate the effects of proliferation kinetics on the rate of somatic evolution toward colorectal tumorigenesis, we designed a spatial model capturing the essential features of tissue architecture and cellular movement in colonic crypts. Each colonic crypt is modeled by a representative column of cells, which is projected onto a linear lattice (3.1 A). The total number of cells per column is given by $N = 80$, as determined by in vivo measurements with a measured mean of 81.9 cells (±9.7 cells) [80]. Position 1 on the left end of the lattice represents the stem cell and position N on the far right represents the apex of the crypt, close to the gut lumen. During every elementary time step of this stochastic process, a cell at position i is selected to divide according to a probability weight, w_i, defined by a specific proliferation kinetic curve for ≤i≤N, zero elsewhere. The two daughter cells are then placed into positions i and $i + 1$, causing cells that previously resided in positions $i + 1$ to N to shift by one position to the right. The last cell is shed into the gut lumen. During each division, a mutation may occur with probability u. If a mutation arises, then each of the daughter cells has a chance of 1/2 of inheriting the mutation. This flexible model then allows us to investigate the effects of different proliferation curves on the rate of somatic evolution. Our model closely resembles the one originally proposed by Nowak *et al.* [91], with the difference of incorporating specific proliferation kinetics.

The dynamics of proliferation is a function of the cell position in the crypt column. The proliferation kinetic curve assigns a mitotic probability to each position in the crypt column: a more proliferative position in the crypt column is represented by a larger mitotic probability. We examined five proliferation kinetic curves (Figure 3.1 C). Position 1, the stem cell position, has the same mitotic probability in all curves, such that $\frac{w_1}{\sum\limits_{i=1}^{N} w_i}$ is identical for all curves. Weights for positions 2 to 80 are assigned by different proliferation curves. Proliferation curve 1 represents the measured kinetic curve, which is extrapolated from *in vivo* bromodeoxyuridine (BrdU) labeling experiments [80, 84]. The measured distribution was approximated using a normal distribution with mean 18 and standard deviation 15 to best match the 90^{th} percentile interval of the measured curve. The probability weights for choosing a cell at each position in the crypt column, i= 2 to 80, are specified by the probability density function, $\frac{1}{15\sqrt{2\pi}}e^{-\frac{1}{2}(\frac{i-18}{15})^2}$. Curve 2 represents the logistic proliferation curve generated from $\frac{1}{1+e^{\frac{i-40}{10}}}$; this curve is used to investigate the effects of spreading the proliferation activities upwards in the crypt column. Curve 3 represents a uniform curve. Curve 4 represents the mirror image of curve 2, with a vertical plane of reflection between positions 40 and 41. Finally, curve 5 represents the mirror image of curve 1, with a vertical plane of reflection between positions 40 and 41. Curves 4 and 5 were selected to examine the effects of proliferating activities concentrated far away from the stem cell.

In addition to the normal shedding of the last cell in the crypt column, accidental premature cell death may also occur (Figure 3.1 B). The rates of apoptosis have been measured using terminal deoxynucleotidyl transferase dUTP nick end labeling (TUNEL) in normal cells, hyperplastic polyps, adenomas and carcinomas; in these cases, the percentage of cells being labeled ranged from 1% to 4% [100]. These observations suggest that multiple cell deaths may occur during each round of cell division. In the context of our model, such cell death may occur after each normal cell division event. The number of dying cells, m, follows a Poisson distribution with mean λ, which denotes the mean number of cell deaths per round of cell division. To incorporate

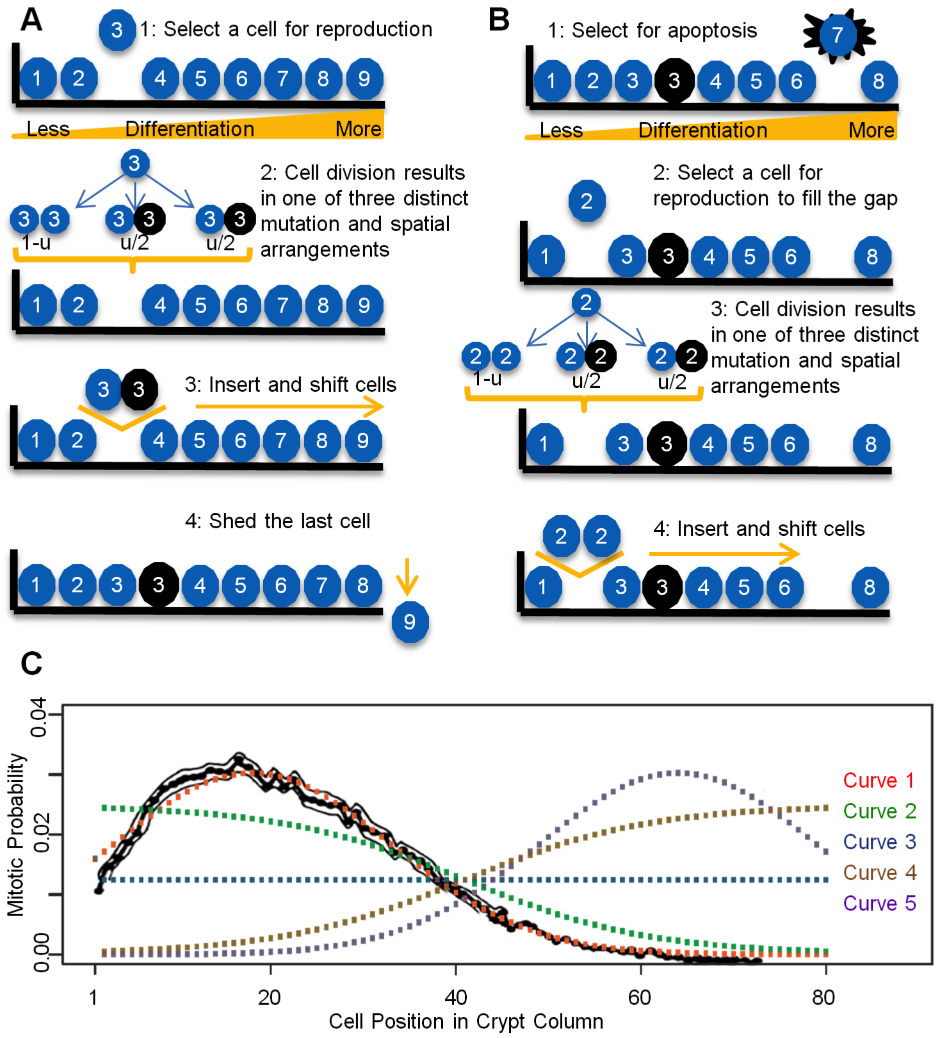

Figure 3.1: Schematics of the linear process and proliferation kinetic curves. A: We designed a linear process model to describe the essential features of cell movement in a colonic crypt. During each time step, a cell at position i is selected to divide. During mitosis, a mutation may occur with probability u, giving rise to one mutated and one wild type daughter cell, with equal probability of occupying either position i or $i+1$. Cell division pushes all cells to the right of position i upwards in the crypt by one position. The last cell is shed into the lumen of the colon. B: Cell death may occur after each round of cell division. The number of dying cells follows a Poisson distribution with mean l; the positions of the dying cells are selected according to a uniform distribution. Dead cells are replaced by replenishing cell divisions. Dying cells at position j can only be replaced by cells of a similar (j+1≤k≤j+d) or less (k≤j) differentiated stage. Position k is selected according to the proliferation kinetics curve. If multiple cells die simultaneously, the replenishing cell divisions occur sequentially, in the order of $j_{(1)}, j_{(2)}$ ... $j_{(m)}$, where $j_{(1)}, j_{(2)}$ ... $j_{(m)}$ are ordered death position. The m positions for the replenishing cell divisions are selected according to the reweighted kinetic curve. C: Proliferation kinetic curves as a function of cell positions. The black curve represents the measured labeling index for normal human colon using bromodeoxyuridine (BRDU). The colored curves represent the five kinetic curves under investigation. See the Methods section for details. Note that curve 1 is in good agreement with the measured labeling index.

the possibility of having multiple cell deaths, λ can vary between 0 and 3.2. The upper bound of 3.2 corresponds to 4% of the length of the crypt column, which is the observed percentage of cells undergoing apoptosis using Tunel labeling [101]. Cells are selected for death according to a particular apoptosis curve specifying the likelihood of cell death for each position in the crypt column. Due to a lack of quantitatively measured apoptosis curves as a function of cell position within the crypt column, we used the five proliferation curves discussed above as proxies for apoptosis curves and tested the resulting twenty five combinations of proliferation and apoptosis curves for their effects on the dynamics of the system.

The vacancy resulting from a cell death at position j can be filled by an additional cell division occurring at position k, where $k \leq j + d$ and d indicates the size of the interval in which more differentiated cells can replace the dead cell. All following numerical examples are calculated based on δ= 5. Position k is selected for a replenishing cell division according to the re-weighted proliferation, $w'_k = \frac{w_k}{\sum\limits_{l=1}^{j+\delta} a_l w_l}$, where a_l indicates the existence of a viable cell at position l. If multiple cells die simultaneously, the replenishing cell divisions occur sequentially, in the order of $j_(1)$, $j_(2)$ ... $j_(m)$, where $j_(1)$, $j_(2)$ ... $j_(m)$ are ordered positions for the m dying cells. The m positions for the replenishing cell divisions are again selected according to the sequentially re-weighted proliferation kinetic curve. This design was chosen to ensure that the dead cell(s) can only be replaced by cells of a similar differentiation stage ($j + 1 \leq k \leq j + d$) or a less differentiated stage (k≤j). In this model, the differentiation hierarchy is fully specified by each cell's position in the crypt column, with position 1 representing the least differentiated cell and position N representing the most differentiated cell. In addition, this replacement rule captures the essential features of two biological observations governing cellular repopulation of crypt columns: (i) replacement mitotic activities are concentrated near the stem cell [101,102]; and (ii) newly divided cells migrate upward in the crypt column [86].

The accumulation of mutations is described by specific transition probabilities between different mutational states. The possibility of back mutations, which reconstitute a less mutated state, is neglected. The mutation rates are assumed to be constant with respect to cell positions and with respect to time. Table 3.1 provides the range of plausible values used for the individual mutation rates. In addition to mutations arising during cell division, we also incorporated random mutations not linked to replication into our framework. Due to the lack of data on the positional dependency of this type of random mutation, such mutations are assumed to be equally likely to occur in any position in the crypt column. The mutation rate for the cell division- independent mutation events is considered to be the same as that of mutation events linked to cell division.

Table 3.1: The values used for individual mutation rates.

	Type of mutation	Mutation rate per cell division	References
u_0	$APC^{+/+}$ to $APC^{+/-}$	10^{-7}	[103]
u_1	$APC^{+/-}$ to $APC^{-/-}$	10^{-7} to 10^{-5}	[104,105]
u_2	$APC^{+/+}$ to $APC^{+/+}CIN$ and $APC^{+/-}$ to $APC^{+/-}CIN$	10^{-7} to 2×10^{-6}	[11]
u_3	$APC^{+/-}CIN$ to $APC^{-/-}CIN$	Up to 10^{-2}	[76]

Time is measured in rounds of cell shedding. At each elementary time step, the cell at position 80 is shed off into the lumen of the gut as the result of cell division and the associated cell movement. Cell deaths and replenishing cell divisions that replace dead cells are not counted as extra increments in time. The rationale for this design is to distinguish between the regenerative cell divisions under normal circumstances and the compensatory cell divisions for apoptotic losses. The instantaneous time scale for replenishing cell divisions is extrapolated from the observation that under strong external stimuli, the rate of progression through the cell cycle is accelerated; for instance, ionizing radiation was shown to induce proliferative activity [106] and shorten the duration of the cell cycle [107]. In addition, thermal injury [108] and starvation- induced stress [109] also tend to increase mitotic activity. In this study, we adopted the assumption of instantaneous replenishing cell divisions regardless of whether strong external stimuli are present or not.

Relative fitness is defined as the ratio of the proliferation rate of a mutant cell to that of a wild type cell at position i in the crypt column, $\frac{w_i^{mutant}}{w_i^{wildtype}}$. A relative fitness greater than 1 indicates that a mutant cell as position i is more likely to be selected to undergo cell division than a wild type cell at the same position. A relative fitness value of less than 1 represents a fitness disadvantage and thus decreases the probability of cell divisions at that position. A relative fitness value of 1 signifies a neutral mutation. We investigated the effects of relative fitness values between 0.5 (representing a 50% fitness disadvantage of a mutant cell) and 2.0 (representing a 100% fitness advantage of a mutant cell) [110].

3.4 Results

3.4.1 Cellular movement

Using this spatially arranged stochastic process model, we first investigated the effects of different proliferation curves on cell movement. Five different proliferation curves were selected to illustrate their effects on cell movement (Figure 3.1C). Curve 1 represents the measured labeling indices (LI) from in vivo experiments [84, 106]; curve 2 was selected to investigate the effects of spreading proliferating activities upwards in a crypt column; curve 3 represents the uniform kinetics in which cell proliferation is equally likely to occur in any cell along the crypt column; and curves 4 and 5 represent the mirror images of curves 2 and 1, respectively. The selection probabilities for position 1 in all curves are identical; furthermore the area under each curve is normalized to the same total in order to make the effects of each curve comparable.

The rates of cellular movement, measured by the number of mitoses required for a cell at a particular position in the column to reach the top of the crypt (position 80), depends on the shape of the proliferation curve (3.1 A Left). As expected for all kinetic curves investigated, cells located near the bottom of the crypt require a larger number of cell divisions to reach the top. For kinetic curves with mitotic activities concentrated near the base of the crypt column (curves 1 and 2), substantially fewer cell divisions are required to push out a cell located in the bottom half of the column. The numbers of cell divisions required to accomplish this task are very similar for curves 1 and 2. The uniform curve (curve 3) requires slightly more rounds of cell divisions (Figure 3.1 A Right). In contrast, curves 4 and 5, which have mitotic activities concentrated near the top of crypt column, require a much larger number of cell divisions than the other curves. In addition, we observed significant variations among individual runs of the stochastic simulation in the number of cell divisions needed to push a cell out of the crypt when considering the five different curves. At each position in the crypt, curves 4 and 5 show larger variations among simulation runs than curves 1, 2, and 3. Interestingly, cells proliferating according to kinetic curves 4 and 5 show a stronger positional dependency in the amount of variation as compared to curves 1, 2 and 3. For instance, for curves 4 and 5, the number of cell divisions needed to push out a cell located near the top of the crypt column is less variable than that for a cell located near the bottom (Figure 3.2 A).

In addition to the qualitative descriptions of cellular movement for different growth kinetic curves, we also derived a mathematical representation of the cellular behavior. The dynamics of cellular movement in the crypt column can be represented by a Markov chain. After each round of cell shedding, the transition probability for a cell in position m to remain in position m is given by $P_{m,m} = \sum\limits_{l>m} w_l + \frac{1}{2}w_m$, and transition probability from position m to $m+1$ is given by $P_{m,m} = \sum\limits_{l<m} w_l + \frac{1}{2}w_m$ for m ranging from 1... N, zero elsewhere. The absorbing state for this transition matrix represents the vent of a cell exiting the crypt column by reaching its top. The expected number of cell divisions needed for a cell to exit the crypt column (E) and the variance of the number of cell division (V) are given as the follows [111]:

$$E = (I_{N\times N} - P_T)^{-1} 1_{N\times 1} \tag{3.1}$$

where $I_{N\times N}$ is the identity matrix of size N, P_T is the transition matrix, and $1_{N\times 1}$ is a vector of length N and

$$V = (2(I_{N\times N} - P_T)^{-1} - I_{N\times N})E - E * E \tag{3.2}$$

where $E * E$ denotes the the Hadamard product of the expected number of cell divisions [112].

The presence of cell death results in changes in the transition matrix. The new transition matrix is then given by products of the transition matrix for normal shedding, P_T and the transition matrix for replenishing cell divisions, P_{TR}. The transition probabilities in the P_{TR} matrix are

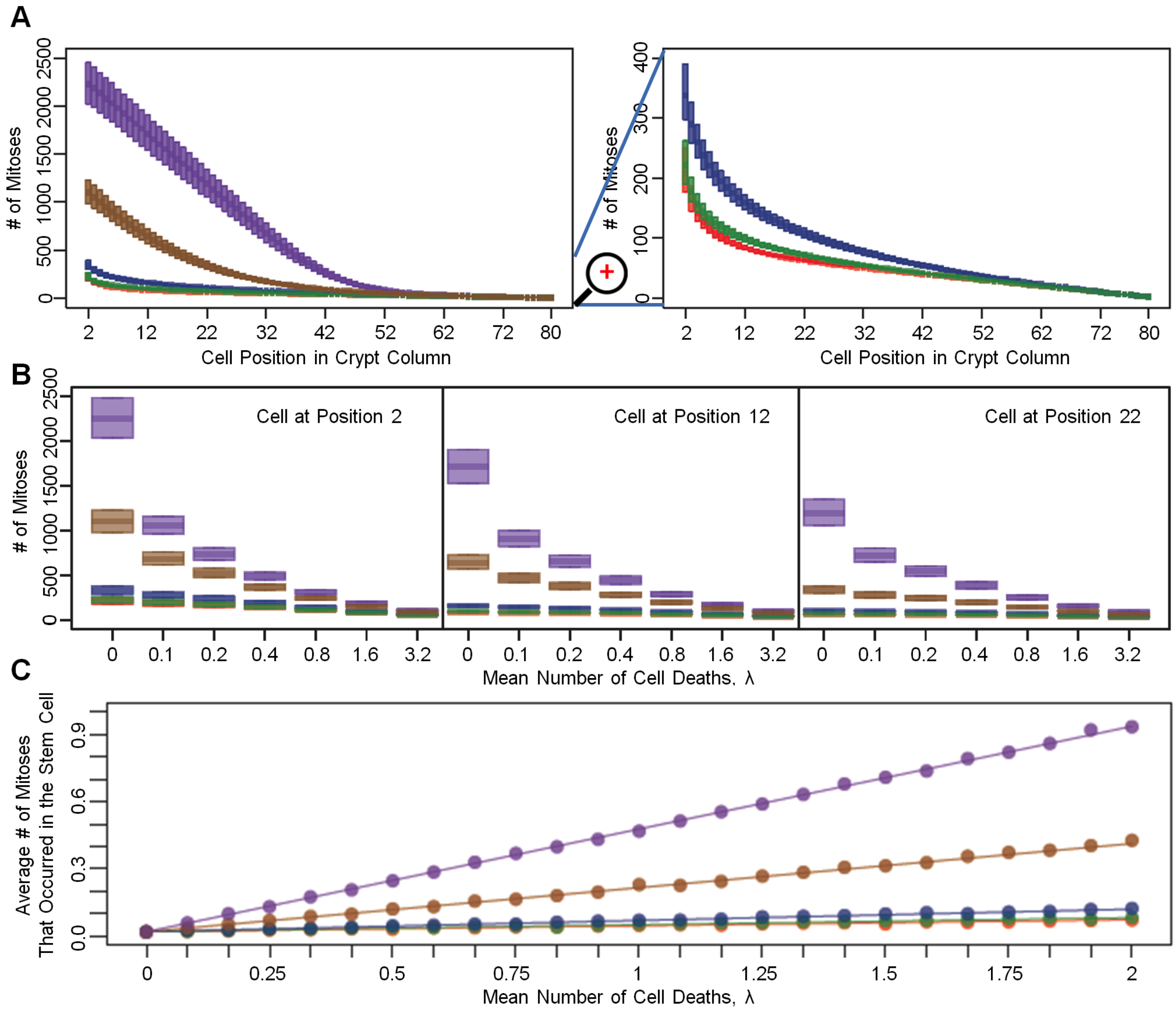

Figure 3.2: The rate of cellular movement in the crypt column. A: The left panel shows the distribution of the number of mitoses needed to push a cell at position i out of the crypt column for each proliferation curve. Colors match the corresponding proliferation curves in Fig. 1C. The horizontal axis represents the position of the cell in the crypt. Box plots indicate the distribution of the number of mitoses, assuming no cell death. The size of each bar indicates the amount of variation in the number of cell divisions. The right panel provides a zoomed-in view focusing on curves 1, 2 and 3. B: The effects of cell death on cellular movement in the crypt for three selected representative positions (2, 12, and 22) in the crypt column under the assumption of a uniform death selection function. As the death rate, λ, increases, the rate of cell movement increases, as shown by the decreasing number of mitoses needed to push a cell out of the crypt column. C: The panel shows the effects of cell death on the mitotic stress of the stem cell assuming a uniform death selection function. The average number of times the stem cell is selected for divisions is displayed as a function of cell death for the proliferation kinetic curves. Without cell death, the number of times the stem cell is selected for cell division is identical for all curves. As λ increases, the mitotic stress on the stem cell increases. The magnitude of increase depends on the shape of proliferation kinetic curve. Dots represent results from simulations, whereas the lines are exact results based on the terms inside the parentheses in Eq. 3.4. All graphs are generated based on 1,000 simulations for each kinetic curve under each scenario. All cells are assumed to have identical relative fitness values.

all zero, except for $P_{m,m-1}$, $P_{m,m}$ and $P_{m,m+1}$, which are given by:

$$\begin{cases} P_{m,m-1} = \sum\limits_{1 \leq j \leq N} \sum\limits_{k>j} Q_{kj} I(j < m < k) + \frac{1}{2} \sum\limits_{m-\delta<j<m} Q_{mj} \\ P_{m,m} = \sum\limits_{1 \leq j \leq N} \sum\limits_{k>j+\delta, k \neq j} Q_{kj} I(m \notin min(k,j)...max(k,j)) + \frac{1}{2} \sum\limits_{j<m-\delta} Q_{mj} \\ P_{m,m+1} = \sum\limits_{1 \leq j \leq N} \sum\limits_{k>j} Q_{kj} I(k < m < j) + \frac{1}{2} \sum\limits_{j>m} Q_{mj} \end{cases} \tag{3.3}$$

where $Q_{kj} = P(death = j) \frac{w_k}{\sum\limits_{l \leq j+\delta, l \neq j} w_l}$ for $k \leq j + \delta$ and $k \neq j$, zero otherwise; this quantity denotes the probability of apoptosis occurring at position j and a replacement cell division occurring at position k; and I denotes an indicator variable. The overall transition probability matrix is then given by:

$$P'_T = \sum_{v=0}^{\infty} P_T \times (P_{TR})^v \times \frac{e^{-\lambda} \lambda^v}{v!} \tag{3.4}$$

This matrix contains the average transition probabilities in the linear system for a given death rate λ. The expected number of cell division needed for a cell to exit the crypt column (E) and the variance for the number of cell divisions (V) can be calculated from equations 3.1 and 3.2.

The most important effect of cell death is its ability to accelerate cellular movement in the crypt column (Figure 3.2 B). As the mean number of deaths, λ, per cell division increases, fewer rounds of cell division are required to push a cell out of the crypt column (Figure 3.2 B). These acceleration effects on cellular movement were observed even when λ was as low as 0.1 and were more prominent in crypts proliferating according to curves 4 and 5 than those proliferating according to the other curves. Regression analysis indicated that the median number of cell divisions needed to push a cell at position 2 out of the crypt was not significantly different among crypt columns proliferating according to curves 1, 2 and 3. Also, interactions between birth and death curves were not significantly correlated with the speed of cellular movement. In addition to causing this acceleration effect, cell deaths also increase the mitotic burden on the stem cell (Figure 3.2 C). The mitotic burden of a cell is defined as the mean number of times a cell is selected to undergo cell divisions per time step. These divisions could either be cell divisions occurring under normal circumstances or replenishing replications that replace dead cells. Note that, in the absence of cell death ($\lambda = 0$), , the average number of times the stem cell is selected to divide is identical for all curves. However, in the presence of cell death, $\lambda > 0$, he number of times of selecting the stem cell to undergo replenishing cell divisions depends on the shapes of the proliferation kinetic and death curves as well as the death rate. Under the uniform death curve, when $\lambda > 0$, proliferative curves 1 and 2 show the smallest increases in the mitotic burden of the stem cell, due to the positioning of the proliferating cells close to the stem cell. These proliferating cells may undergo replenishing cell divisions to replace dead cells arising further up in the crypt column, which help lessen the mitotic burden on the stem cell. In contrast, the stem cell's mitotic burden increases drastically for proliferative curves 4 and 5 due to the long distance between the stem cell and the other proliferating cells. In these cases, cell deaths occurring in the middle of the crypt column can only be replaced by stem cell divisions due to the shape of the mitotic curves and the replenishing rules imposed; this effect thus increases the mitotic burden on the stem cell. The mitotic burden for other cells is less affected by cell death as compared to that of the stem cell and the overall shape of the kinetic curves remains similar to the original shape in the absence of cell death. One important consequence of over-using the stem cell to replace dead cells is that it accelerates the rate of mutation accumulation in the stem cell, as explored in the following section.

3.4.2 The single mutation model

We then incorporated a simple mutation model into the linear process. This addition captures for instance the accumulation of an inactivating mutation in one APC allele, thus transforming an $APC^{+/+}$ cell into an $APC^{+/-}$ cell (Figure 3.3 A). As a representative example, the dynamics of the somatic evolution process within a single crypt column is displayed in (Figure 3.2 B) n the absence of cell death, all mutations arising in non-stem cells within the crypt column are eventually flushed out of the crypt; only mutations arising in the stem cell have the ability to reach fixation, i.e. reach 100% frequency within a crypt column. This spatial restriction highlights the fundamental difference between the linear process and a stochastic process model describing a well-mixed population, for instance the Moran process [89] or the Wright-Fisher process. In the latter models, any cell within the population has an equal chance of taking over the population if all fitness values (i.e. growth and death rates) are equal. In the linear process, in contrast, only a mutation arising in the stem cell has the ability to take over the entire population of cells.

Somatic evolution in the crypt column in the absence of cell death can be split into two disjoint events: (i) a mutation arising in the stem cell, and (ii) mutation propagation through the crypt column (Figure 3.3 B). Since the mutation rate at which APC is inactivated per allele, u_0, is low (estimated to be on the order of 10^{-7} per cell division [103]), the rate-limiting event of this process is the time it takes until the mutation arises in the stem cell; mutations arising in any other cell are neglected here since they cannot reach fixation in the crypt. The number of times the stem cell divides is specified by the proliferation kinetic curve. In the absence of cell death, the probability of selecting the stem cell for cell division is identical for all kinetic curves; thus the time, measured by the number of mitoses occurring, until all cells in the crypt column are in the $APC^{+/-}$ state is identical for all kinetic curves (Figure 3.3 C). The distribution of mitotic activities along the crypt column plays no role in modifying the speed of mutation accumulation in the stem cell, since the rate of stem cell divisions are equal among all curves investigated (see Methods). The probability of fixation by time t in the linear process is determined by the probability that a mutation has arisen in the stem cell by time t,

$$P(t) = 1 - (1 - \frac{u_0 w_1}{2})^t \tag{3.5}$$

For a small u_0, this expression can be approximated by

$$P(t) = \frac{u_0 w_1 t}{2} \tag{3.6}$$

Here w_1 denotes the probability of selecting the stem cell position for replication and the factor of $\frac{1}{2}$ arises from the two possible arrangements of cells after cell divisions, only one of which can lead to a mutant cell residing in the stem cell position. Once the stem cell becomes mutated, fixation of its offspring in the crypt column quickly ensues. However, the rate of propagation of mutated cells throughout the crypt is heavily influenced by the kinetic curves (Figure 3.3 D). Mutated cells in crypts proliferating according to curves 1 and 2 reach fixation faster than in those proliferating according to curves 4 and 5. Curve 3, the uniform curve, leads to fixation of mutant cells on a

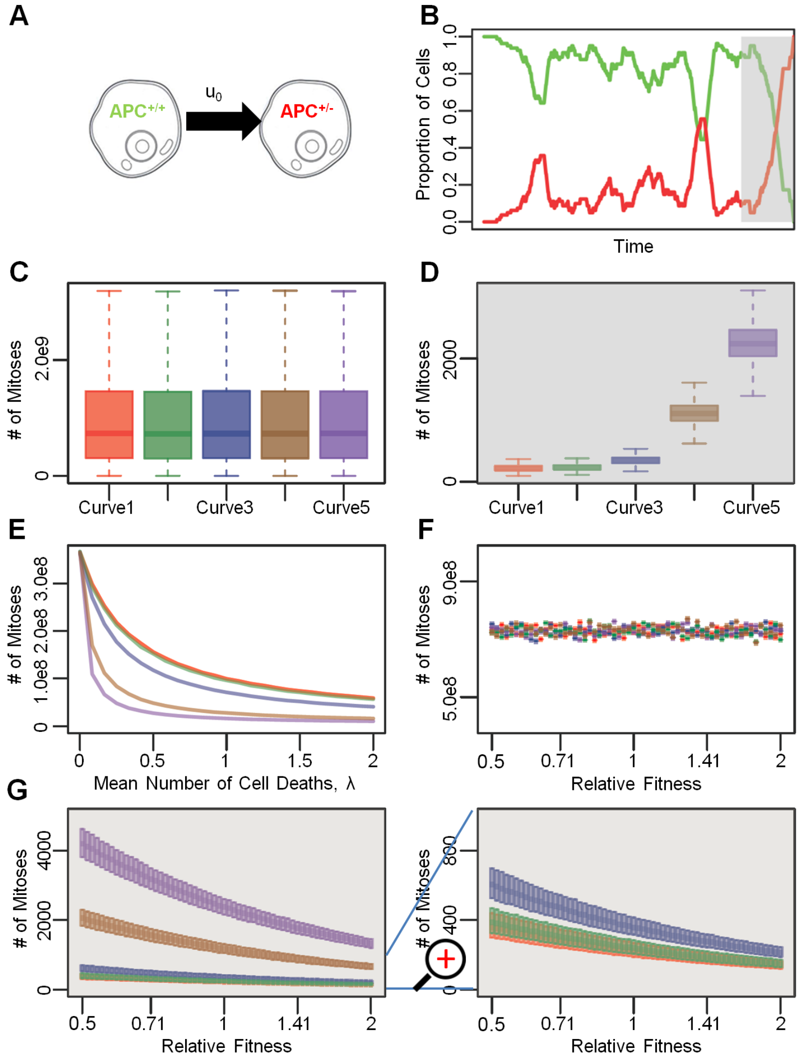

Figure 3.3: The single mutation model. A: Schematic representation of the single mutation model. B: An example of the dynamics of somatic evolution in the crypt column. The curves show the proportions of cells in the crypt column. The colors correspond to cell types in panel A. The gray shaded region indicates the stem cell is mutated to $APC^{+/-}$. For illustration purposes, u_0 = 0.01. C: The number of mitoses needed for a wild type crypt column to transition to an $APC^{+/-}$ state for various proliferation kinetic curves in the absence of cell death. As expected, the numbers of cell division needed to reach mutant fixation are the same for all curves. The mutation rate is $u_0 = 10^{-7}$ per cell division. Box plots are color coded, corresponding to the curves in Fig. 1C. D: The number of mitoses needed for fixation of $APC^{+/-}$ cells for various proliferation kinetic curves, measured from the time at which the stem cell accumulates the $APC^{+/-}$ mutation assuming no cell death. The gray area corresponds to the gray shaded interval in panel B. E: Acceleration of mutation accumulation due to cell death. As the death rate, l, increases, fewer cell divisions are required for a mutated stem cell to arise. The comparison between panels C-E highlights the importance of proliferation kinetics of non-stem cells in the presence of cell death. F: Effects of fitness differences and proliferation curves on the rate of somatic evolution. The range of relative fitness spans from 0.5 to 2.0. G: The left panel shows the effects of fitness differences and different proliferation curves on the rate of $APC^{+/-}$ fixation, starting from an $APC^{+/-}$ stem cell in the absence of cell death. The panel on the right provides a zoomed-in view on curves 1, 2 and 3.

Table 3.2: The probabilities of selecting the stem cell for a replenishing division per cell death event.

	Death Curve 1	Death Curve 2	Death Curve 3	Death Curve 4	Death Curve 5
Birth Curve 1	0.0374	0.0344	0.0269	0.0193	0.0186
Birth Curve 2	0.0471	0.0421	0.0314	0.0207	0.0190
Birth Curve 3	0.0844	0.0735	0.0504	0.0274	0.0224
Birth Curve 4	0.4201	0.3354	0.1969	0.0584	0.0294
Birth Curve 5	0.9180	0.7525	0.4587	0.1650	0.0488

slightly slower time scale than curves 1 and 2, but still faster than curves 4 and 5. In addition, the amount of variability in the number of cell divisions required for the $APC^{+/-}$mutation to propagate through the crypt column also depends on the shapes of the kinetic curves. As the mitotic activity becomes more concentrated near the top of the crypt, towards the gut lumen, the amount of variability among individual simulation runs in the fixation time increases (Figure 3.3 D).

In contrast, in the presence of non-stem cell death, the interactions between birth and death curves determine the speed of somatic evolution (Figure 3.3 E). We derived an analytical approximation to show the accelerating effects of non-stem cell death on the rate of mutation accumulation in the stem cell, in the absence of relative fitness differences between mutated an normal cells and in the absence of stem cell death. The probability of selecting the stem cell to undergo one round of additional cell division, and thus to shift all downstream cells along the crypt column to fill the vacancy created by a cell death at position j, is given by $\frac{w_1}{\sum_{l=1}^{j+\delta} a_l w_l}$, where δ specified the size of the interval (i.e. the number of cells) in which more differentiated cell can replace the dead cell. Thus, the probability of a mutation arising in the stem cell during this additional round of cell division is given by $\frac{w_1}{\sum_{l=1}^{j+\delta} a_l w_l}\frac{u_0}{2}$. Since the expected number of cell deaths occurring during a time interval t is λt, the probability that a mutation occurs in the stem cell during λt additional cell divisions is given by

$$P(t) = 1 - \prod_{r=1}^{\lfloor \lambda t \rfloor} (1 - \frac{w_1}{\sum_{l=1}^{j_r+\delta} a_l w_l}\frac{u_0}{2}) \tag{3.7}$$

where j_r indicates the position at which the r^{th} cell death event occurs. For small u_0, this expression can be approximated by $\sum_{r=1}^{\lfloor \lambda t \rfloor} \frac{w_1}{\sum_{l=1}^{j_r+\delta} a_l w_l} \frac{u_0}{2}$. If $\lambda t >> N$, it can further be approximated by $\frac{u_0 \lambda t}{2} \sum_{k=2}^{N} (\frac{w_1}{\sum_{l=1}^{k+\delta} a_l w_l} P_{death}(k))$, where $P_{death}(k)$ denotes the probability of cell death occurring at a particular position in the crypt column, and $a_k = 0$.

In addition to division-linked mutations, cell division-independent mutation also contributes to the rate of mutation accumulation in the stem cell. Given the assumption that cell division-independent mutation may occur anywhere in the crypt column, the additional contribution to the overall rate of mutation accumulation in this scenario can be modeled by including the factor $\frac{u_0 t}{N}$. Thus the overall fixation rate in the crypt column of a new mutant cell is given by

$$P(t) = u_0 t (\frac{w_1}{2} + \frac{\lambda}{2} \sum_{k=2}^{N} (\frac{w_1}{\sum_{l=1}^{k+\delta} a_l w_l} P_{death}(k)) + \frac{1}{N}) \tag{3.8}$$

The interactions between birth kinetics and death positions determine the probability of selecting the stem cell for replenishing cell divisions after apoptosis, as stated by the term $\sum_{k=2}^{N} (\frac{w_1}{\sum_{l=1}^{k+\delta} a_l w_l} P_{death}(k))$ in equation (3.9).

For the five curves examined, the interactions between birth kinetics and death selection are shown in Table 3.2. Curve 1 has the lowest probability of selecting the stem cell for replenishing cell divisions for all death curves. In addition, the rates of selecting the stem cell are less variable for curve 1 across different death selection curves (row 1 in Table 3.2) than for other proliferation kinetic curves. Deaths occurring near the top of the crypt column, such as in death curve 5, lower the mitotic burden on the stem cell for all birth kinetics curves. Of all twenty-five combinations examined, the interaction between birth kinetics curve 1 and death selection curve 5 results in the lowest amount of mitotic burden on the stem cell. In contrast, birth kinetics curve 5, with mitotic probabilities concentrated near the top of the crypt, and death selection curve 1, with apoptosis occurring near the stem cell, result in substantial increases in the probability of selecting the stem cell for replenishing cell divisions. In addition to the interaction between the location of proliferating cells and cells undergoing apoptosis, the rate of cell death, λ, also controls the rate of mutation accumulation in the stem cell. As λ increases, the rate of mutation accumulation in the stem cell is accelerated. Lastly, cell division-independent mutation increases the overall mutation rate, as shown by the last term in equation (3.9).

We also investigated the effects of fitness changes of mutant cells on the speed of somatic evolution. Relative fitness is defined as the ratio of selection probabilities for proliferation of a mutant cell to that of a wild type cell at the same position in the crypt column (see Methods). Changes in the relative fitness can potentially affect the speed of both the rate of mutation accumulation in the stem cell and the rate of mutant propagation through the crypt column. We investigated the effects of relative fitness values between 0.5 (representing a 50% fitness disadvantage of a mutant cell) and 2.0 (representing a 100% fitness advantage of a mutant cell) [110]. The speed of somatic evolution was not significantly affected by changes in fitness within this range (Figure 3.3 F). This effect arises because the rate-limiting event is represented by the generation of the first mutation in the stem cell, which - unlike its propagation throughout the crypt column - is not dependent on fitness. In the case of an extremely advantageous mutation with a relative fitness value greater than 10, fixation of its offspring in the crypt column can be substantially delayed for the cases in which the initial mutation arises in a non-stem cell. In these cases, cell divisions in non-stem mutants are driving the cellular movement and tissue regeneration in the crypt column, thus reducing the probability of the stem cell undergoing cell divisions. When conditioning on the event that the stem cell is already mutated, we found that the relative fitness has a significant effect on the fixation time for some kinetic curves (Figure 3.2 G). For instance, curves 4 and 5 are more sensitive to changes in relative fitness; as the relative fitness of mutants decreases, more cell divisions are required for a mutant cell to reach fixation. In contrast, curves 1 and 2 are less sensitive to changes in the relative fitness. The variation in the fixation time also depends on the kinetic curves and on the relative fitness of the mutant cells. Again, curves 1 and 2 lead to less variation compared to curves 4 and 5. Furthermore, at low relative fitness values, the number of cell divisions necessary for fixation is more variable than at high relative fitness values for curves 4 and 5. The uniform curve is more sensitive to fitness variations compared to curves 1 and 2 (Figure 3.2 G).

We then modified the basic mathematical framework to allow for the special case of stem cell death. In such situations, a mutant stem cell may be replaced by a more differentiated cell. Apoptosis of the stem cell delays the rate of mutation accumulation in the stem cell and mutant fixation. Regression analysis indicates that the number of times a mutant stem cell is replaced by a wild type cell as the result of apoptosis in the stem cell position is significantly related to the birth kinetics, death rate, relative fitness, and specific interactions between birth and death curves. Kinetics curves with mitotic probabilities concentrated near the top of the crypt (curves 3, 4 and 5) are less likely to lead to a loss of a mutation that had arisen in the stem cell position. Mutant stem cells with a low relative fitness are more likely to be replaced by wild type cells, since such mutant cells have a slower rate of propagation. Furthermore, large death rates increase the mean number of times a mutant stem cell is replaced by a wild type cell through apoptosis and dedifferentiation. Since the death selection function is normalized such that the stem position has an equal probability of being selected for all curves, death curves have no effect on the rate at which mutant stem cells are replaced by wild type cells. The interactions between birth and death curves only have weak effects on how often the mutant stem cell loses a mutation. Overall, these observations suggest that apoptosis in the stem cell has the ability to delay mutant fixation, whereas apoptosis in the differentiated cells accelerates mutation accumulation by increasing stem cell divisions. Consistent with this observation, recent studies suggest that a high rate of stem cell apoptosis in the small intestine is partially responsible for the low incidence of small intestine cancer compared to colorectal cancer; in the latter, the stem cell is protected from undergoing apoptosis by the expression of $bcl-2$, an anti-apoptosis protein [113].

3.4.3 The two mutation model

We then investigated a two mutation model within the linear process. This scenario captures, for instance, the mutations inactivating both alleles of the APC gene (Figure 3.4 A). Similarly to the single mutation model, the rate of emergence of double mutant cells (i.e. $APC^{-/-}$ cells) is driven by the rates per cell division at which the two mutations arise, for all growth kinetic curves investigated.

We first studied the dynamics of the accumulation of these two mutations by investigating the effects of proliferation kinetics on the probability that an $APC^{+/-}$ cell acquires an additional mutation in the second APC allele before being flushed out of the crypt. We investigated these dynamics in the absence of cell death. Figure 3.4 B shows a representative simulation run. There are two scenarios: the first APC mutation may arise in the stem cell, or alternatively it could arise in a non-stem cell. Once the stem cell harbors the first APC mutation, in the absence of cell death, this mutation is permanently maintained in the crypt and eventually, the second APC mutation arises. In contrast, if the first APC mutation arises in a non-stem cell, the probability that this cell and its progeny gain an additional mutation before exiting the crypt depends on four factors: the mutation rate for inactivating the second APC allele, u_1, the location of the $APC^{+/-}$ cell, the kinetic curve, and the relative fitness of the $APC^{+/-}$ cell. As expected, an increase in u_1 enhances the probability of accumulating an additional mutation in a non-stem mutant cell (Figure 3.4 C-F). This observation agrees with the findings by Komarova and Wang [88] that for a large u_1, $APC^{+/-}$ cells are likely to arise among differentiated cells. The position of the $APC^{+/-}$ cell also has a significant influence on the probability of accumulating the additional mutation. An $APC^{+/-}$ cell residing near the stem cell has a higher probability of acquiring a second mutation before being "washed" out of a crypt than a cell residing near the top of crypt (Figure 3.2 C-F). Finally, different birth kinetic curves also have effects on the probability of acquiring further mutations. For an $APC^{+/-}$ cell at a particular position between 3 and 80, curves with mitotic activities concentrated near the stem cell (curves 1, 2 and 3) have small probabilities of acquiring the second APC mutation before the cell exits the lattice (Figure 3.4 C-F). This effect is more prominent for a large than for a small u_1. The probability of accumulating the second mutation depends on the sum of mitotic probability weights for each cell: w_1 +...+w_{i-1}, where i denotes the position of the first $APC^{+/-}$ cell; this sum is inversely related to the probability of accumulating the second APC mutation. For instance, if the $APC^{+/-}$ cell resides at position 8, then the curve with the smallest sum of mitotic probability weights for positions 1 to 7 leads to the largest chance that this clone accumulates an additional

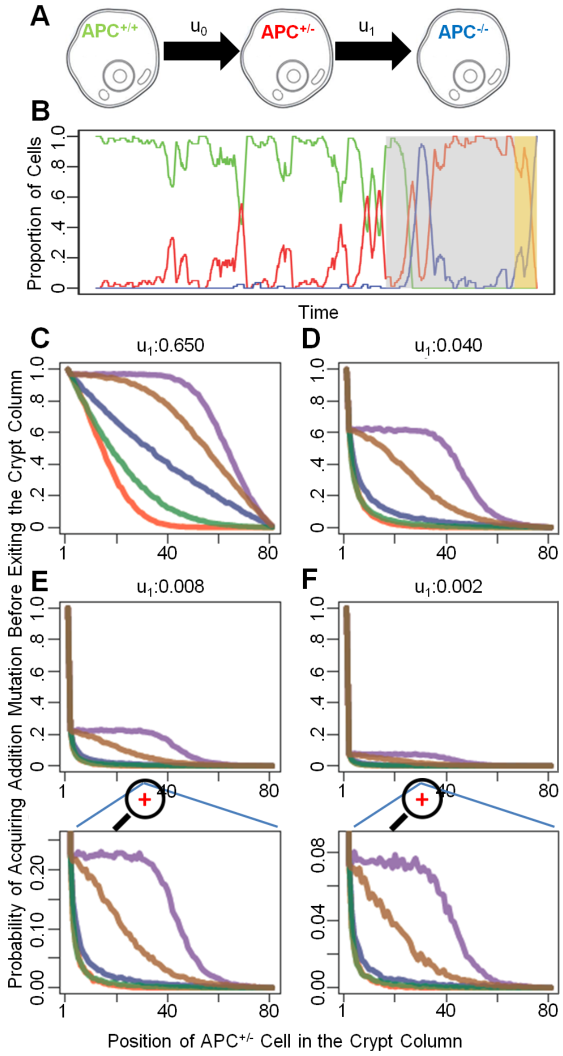

Figure 3.4: The two mutation model. A: Schematic representation of the mutations leading to inactivation of both APC alleles, at rates u_0 and u_1, respectively. B: A representative example of the dynamics of somatic evolution in the linear process. Each color-coded curve represents the proportion of each cell type in the crypt column, with colors corresponding to those in panel A. The gray shaded region represents the time interval during which the stem cell is in the $APC^{+/-}$ state. The yellow shaded region represents the time interval during which the stem cell is in the $APC^{-/-}$ state. C-F: Conditional probability for losing the second APC allele before an $APC^{+/-}$ cell at a particular position along the crypt column is "flushed" out of the crypt in the absence of cell death. At each position between 2 and 80, 1,000 simulation runs are generated in the absence of cell death to determine the probabilities of $APC^{+/-}$ cells gaining new mutations before being "flushed" out of the crypt column. Four different rates of inactivating the second APC allele, u_1, were investigated and are shown on the top of the four sub panels. The bottom two panels provide zoomed-in views.

mutation before exiting the lattice. Since all curves have the same mitotic probability for position 1, the chance that an $APC^{+/-}$ cell at position 2 accumulates a new mutation is the same for all kinetic curves. This effect arises only in the absence of cell death. Therefore, conditional to the event that an $APC^{+/-}$ cell resides between positions 3 and 80, those kinetic curves with mitotic probability weights concentrated near the stem cell confer a protective effect against acquiring new mutations. Increasing the relative fitness of mutant cells increases the likelihood that an $APC^{+/-}$ cell acquires a new mutation by enhancing the likelihood of this cell and its progeny to be selected for cell divisions. These considerations hold under the assumption of no cell death. The presence of cell death, in contrast, reduces the probability for a mutant cell to gain an additional mutation; increasing the rate of cell death enhances the likelihood for a mutant cell and its progeny to either die or be flushed out the crypt before they accumulate a new mutation.

3.4.4 Chromosomal instability

Finally, we incorporated the effects of chromosomal instability (CIN) into our model. CIN arises due to the accumulation of a specific mutation at rate u_2 and leads to a large mutation rate, u_3, at which the second APC allele is inactivated during cell divisions [76] (Figure 3.5 A). Considering this additional mutation event, we then set out to investigate the effects of CIN on the dynamics of the system. For large u_3, we observed a phenomenon that has previously been termed "stochastic tunneling" [114] . Tunneling refers to the process in which a crypt column moves from a homogeneous state in which all cells harbor ρ mutations to a homogeneous state in which all cells harbor $\rho + 2$ mutations, without ever transiting through a state in which all cells harbor $\rho + 1$ mutations. For instance, in our model, tunneling occurs when cells in the crypt column move from an $APC^{+/-}$ state directly to an $APC^{-/-}$CIN state, without reaching fixation in the $APC^{+/-}$CIN state, as illustrated in Figure 3.5 B. Another possible tunneling scenario is $APC^{-/-}$CIN to $APC^{+/-}$CIN to $APC^{-/-}$CIN. Tunneling between other states is less likely to occur given the small second mutation rates. Unlike prior investigations concerning the tunneling rate for a well-mixed population of cells [115], cells in this model remain constrained to a one-dimensional lattice.

The tunneling rate depends on the mutation rate, $u3$, the death rate, the birth kinetic curve, the death selection curve, and the relative fitness of mutated cells. Consider the uniform death curve (curve 3) as an illustration: for this curve, as u_3 increases, a larger proportion of all simulation runs display tunneling for all five proliferation kinetic curves (Figure 3.5 C). Even though all curves lead to this phenomenon, we found that crypts proliferating according to curves 4 and 5 are more likely to display tunneling than those proliferating according to curves 1, 2 and 3. For curves 4 and 5, more stem cell divisions are required to reach fixation of $APC^{+/-}$ CIN cells, starting from an $APC^{+/-}$CIN stem cell, than for the other curves. Because of the large number of stem cell divisions in crypts proliferating according to curves 4 and 5, there is a large probability for the stem cell to lose the second copy of the APC gene before all cells in the column become $APC^{+/-}$CIN cells. For a given u_3, as the mean number of cell deaths, λ, increases, a larger proportion of simulation runs reach fixation of $APC^{-/-}$CIN cells via tunneling. Furthermore, we found that increases in λ result in larger increases in the tunneling probability for cells proliferating according to curves 4 and 5 than for those proliferating according to curves 1, 2 and 3. Finally, in the presence of cell death, high relative fitness values of $APC^{+/-}$CIN cells reduce the tunneling probability, whereas high relative fitness values of $APC^{-/-}$CIN cells promote tunneling. Since the relative fitness values of $APC^{+/-}$CIN and $APC^{-/-}$CIN cells are correlated, the ratio of relative fitness values of $APC^{+/-}$CIN and $APC^{-/-}$CIN cells determines the tunneling rate. This ratio affects the selection of replacing cell divisions and hence the tunneling probability. Higher-order interaction terms involving birth curves, death curves and death rate are also important determinants of tunneling rates.

Finally, we derived a general solution for the tunneling probability under the assumption of no cell death. The general solution comprises the production of three terms: (1) the limiting probability of the initial $APC^{-/-}$CIN cell at position k to reach either the absorbing states: that an $APC^{-/-}$CIN stem cell arises, leading to tunneling, or that no further mutation arises in the stem cell position before the $APC^{-/-}$CIN clone is removed from the crypt column, signifying

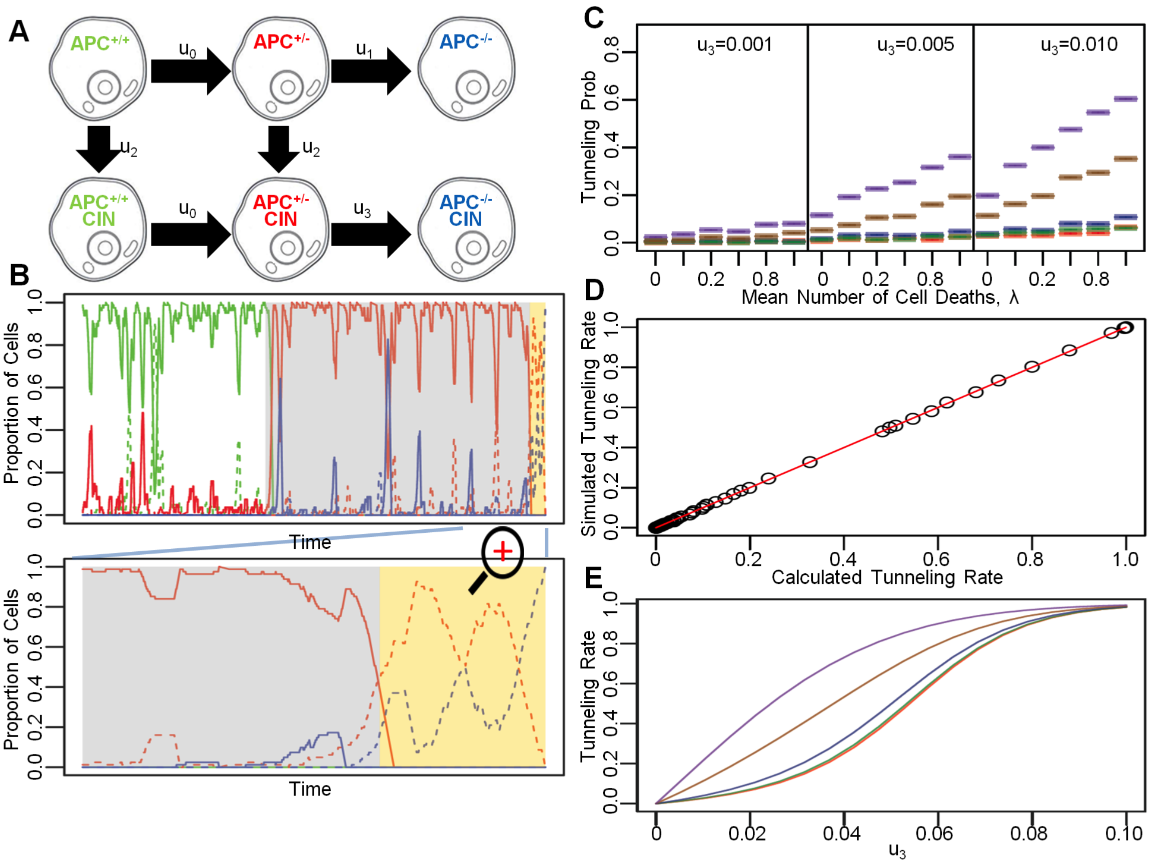

Figure 3.5: The effects of chromosomal instability and tunneling. A: Schematic representation of the mutations leading to the inactivation of both APC alleles incorporating chromosomal instability. B: The upper panel displays a representative example of linear somatic evolution dynamics. Each color-coded curves represent the proportion of each cell type in the crypt column, with colors corresponding to those in panel A. Dashed and solid lines correspond to cells with and within CIN respectively. The gray and yellow shaded regions represent the time interval during which the stem cell is in the $APC^{+/-}$ state and $APC^{-/-}$ state respectively, regardless of CIN status. The lower panel provides a zoomed-in view. Notice that the dashed red curve does not reach 1, which signifies tunneling. This representative simulation run is performed using the uniform proliferation kinetics in the absence of cell death and fitness differences. The mutation rate is inflated to $u_0 = u_1 = u_2 = 10^{-3}$ and $u_3 = 0.01$ for computational speed. C: The tunneling probability as a function of u3 and the cell death rate, l, for the five proliferation curves under uniform death selection. To reduce the extent of complexity, tunneling rate is simulated using a three-state system consisting of $APC^{+/-}$, $APC^{+/-}$CIN and $APC^{-/-}$CIN cells instead of the six-state system as illustrated in Panel A. Each simulation run starts with a crypt column seeded with an $APC^{+/-}$ cell at the stem position. The number of simulation runs is set at 1,000. Stem cell death is allowed. D: Concordance between simulated tunneling rates and analytical rates for linear systems of length N = 10, 20, ...100 with equal proliferation probability at each position, using mutation rate u_3 = 0.001, 0.01, 0.1 and 1.0. All simulations were performed for 1,000 runs. E: Analytical tunneling rate for the five proliferation curves at different mutation rate.

the fixation of $APC^{+/-}$CIN cells; (2) the probability that the initial $APC^{-/-}CIN$ cell arises at position k conditional to the vent that an $APC^{+/-}$CIN to $APC^{-/-}$CIN mutation occurred while $APC^{+/-}CIN$ populating the crypt column reach position l; (3) the probability that an $APC^{+/-}$CIN to $APC^{-/-}CIN$ mutation occurs as $APC^{+/-}CIN$ cells populating the crypt column reach position l. The transition matrix for calculating the limiting probabilities is given by

$$\begin{cases} p_{i,j} = \frac{1}{2}u_3(w_{j-1} + w + j), \text{for } 1 \leq j < i \\ p_{i,j} = \frac{1}{2}u_3 w_{j-1} + \sum\limits_{l=1}^{N} w_l \\ p_{i,i+1} = (1 - u_3) \sum\limits_{l=1}^{i-1} w_l \\ p_{N+1,N+1} = 1 \\ 0 \text{ elsewhere} \end{cases} \tag{3.9}$$

The transition matrix specifies the movement of the left-most $APC^{-/-}$CIN cell in the crypt column. Under the assumption of no cell death, the movement of the left-most $APC^{-/-}$CIN cell completely determines the tunneling probabilities. The two absorbing states are state 1, when the left-most $APC^{-/-}$CIN cell arises in the stem cell position, resulting in tunneling, and state $N + 1$, when the left-most $APC^{-/-}$CIN cell is out of the crypt column, resulting in fixation of $APC^{+/-}$CIN cells. The tunneling probability vector of length $N - 1$ can be calculated using the fundamental matrix of an absorbing Markov chain [103, 112],

$$[P(\text{Tunneling}|APC^{-/-}\text{CIN cell at position k})] = [I_{N-1} - P_{2:N,2:N}]^{-1} \times [P_{2:N,1}] \tag{3.10}$$

Thus, the overall tunneling vector of length N, denoted by $[P(T|k)]$, is given by

$$[P(T|k)] = [1, P(\text{Tunneling}|APC^{-/-}\text{CIN cell at position k})] \tag{3.11}$$

This expression arises since tunneling occurs with probability 1 if the $APC^{+/-}$CIN to $APC^{-/-}$CIN mutation arises in the stem cell.

Under the assumption of no cell death, the mutation conferring CIN must occur in the stem cell position, since otherwise, it would be flushed out of the crypt column. Thus, the probability for the initial $APC^{-/-}$CIN cell to arise at position k depends on the position of the right-most $APC^{+/-}$CIN cell as the latter populate the crypt column:

$$\begin{aligned} &P(\text{initial } APC^{-/-}\text{CIN cell at position} k | \text{right-most} \\ &\quad APC^{+/-}\text{CIN cell at position } l \text{and a mutation occurs}) \\ &\quad = \frac{0.5(w_{k-1} + w_k))}{\sum\limits_{i=1}^{l} w_i} \text{ for } k \leq l+1 \end{aligned} \tag{3.12}$$

Thus, the probability that the initial $APC^{-/-}$CIN cell occurs at position k conditional to the event that the right-most $APC^{+/-}$CIN cell is located at position l and a mutation occurs can be arranged in matrix form, denoted by $[P(k|l)]$, with columns representing k and rows representing l. Lastly, the probability that an $APC^{+/-}$CIN to $APC^{-/-}$CIN mutation occurs as the right-most $APC^{+/-}$CIN cell moves into position l follows a geometric distribution:

$$P(\text{right-most } APC^{+/-}CIN)\text{cell at position } l \text{ and a mutation occurs}) = (1-u_3)^{l-1}u_3 \tag{3.13}$$

for $1 \leq l \leq N$. Thus, a vector of length N, denoted by $[P(l)]$, completely specifies the probabilities of a mutation occurring as the right-most $APC^{+/2-}$CIN cell moves from $l-1$ position to l. Therefore, the overall tunneling probability can be calculated as

$$P(T) = [P(T|k)] \times [P(k|l)] \times [P(l)] \tag{3.14}$$

We then compared this analytical result with exact computer simulations and found good agreement (Figure 3.5 D). Furthermore, using this analytical result, we calculated the tunneling rates for the different proliferation curves at various values of the $APC^{+/-}$CIN to $APC^{-/-}$CIN mutation rate u_3 (Figure 3.5 E). For a given u_3, those proliferation curves with mitotic probabilities concentrated near the stem cell have lower tunneling probabilities than those with mitotic probabilities near the top of the crypt. In addition, in the absence of cell death, a variation in fitness values does not affect the tunneling rates; in contrast, fitness variation is significantly associated with the tunneling rate when cell death is present.

3.5 Discussion

We designed a spatially arranged computational model of intestinal epithelial cells to investigate the effects of proliferation kinetics on the dynamics of cell movement and mutation accumulation in the colonic crypt. The model considers a single cell column within a colonic crypt, in which N cells are arranged onto a one-dimensional lattice. One end of the lattice represents the bottom of the crypt, where the stem cell resides, and the other end represents the orifice of the crypt (Figure 3.1 A). Mitotic activities cause cell movements towards the upper end of the crypt and push the last cell off the lattice. During each cell division, a mutation may occur, which might increase the proliferative activity of the resulting mutant cell and can represent a step towards colorectal tumorigenesis. We then compared the effects of five different proliferation curves on the speed of somatic evolution and cell movement (Figure 3.1 C). We used these proliferative curves to demonstrate that proliferation kinetics is an important criterion that needs to be considered in modeling the dynamics of somatic evolution in spatially arranged tissues. In addition to the proliferation kinetics, we introduced a differentiation hierarchy to this linear process model. In our model, only cells at similar or less differentiated stages can replace dead cells. Finally, we used a discrete time scale such that under normal circumstances, only cell divisions contribute to the measurement of time while cell death and replenishing cell division events are assumed to be instantaneous in time.

Compared to previously published models [94, 95, 97, 98], in our model the crypt structure is greatly simplified to a one-dimensional lattice; nonetheless, the essential features of cell movement are captured by our simple model, in that cells move upward towards the gut lumen with limited lateral movement [82]. This simplified design allows for the investigation of the effects of proliferation kinetics on the rate of mutation accumulation. In addition, unlike previously published models, our simple design enables us to derive analytical solutions for several quantities of interest such as the rate of mutation accumulation and the tunneling probability. In contrast to compartmental models [116–118], the linear model has the advantage of retaining the spatial structure dictating colonic epithelial cell behavior. In addition, our model contains a gradual differentiation hierarchy, which is represented by the cell positions in the crypt, instead of being characterized by discrete compartmental boundaries.

Using this model, we demonstrated that spatially explicit proliferation kinetics have a significant impact on the stability and the dynamics of the crypt column in terms of the speed of cell movement and mutation propagation as well as sensitivities to apoptosis and selective effects of mutant cells. Comparing the proliferation kinetic curves we investigated, we identified three advantages of a spatial architecture in which the proliferative potential of cells is located close to the stem cell: 1) this type of proliferation architecture increases the stability of the linear system in terms of providing a less variable rate of cell movement; 2) in the presence of cell death, this architecture delays the rate of mutation accumulation in the stem cell; and 3) it provides protection against tumorigenesis by reducing the probability of acquiring further mutations in the absence of cell death. These results suggest that the kinetic curve identified using labeling index studies in the human colon [80,84] best delays the rate of somatic evolution towards colorectal tumorigenesis when compared to the other curves investigated here.

Prior work has demonstrated that both spatial organization and cellular hierarchy need to be considered in modeling somatic evolution [119]. Our findings highlight the importance of proliferation patterns, in addition to spatial arrangements and cellular hierarchies, in studying tissue and mutation dynamics. This area has not been explored in-depth prior to our investigation. Despite the highly simplified nature of our model, we have demonstrated that proliferation curves with mitotic activities concentrated near the stem cell confer an advantage to the colon crypt by increasing the stability of the linear system and by delaying the rate of mutation accumulation. Normal proliferation kinetics, in addition to the linear tissue architecture, can suppress the rate of evolution towards colorectal cancer. A departure from such proliferation kinetics accelerates the rate of mutation accumulation in the colonic crypt and destabilizes natural cell flow, thus representing a step towards cancer.

References

[1] N. M. Laird and J. H. Ware, "Random-effects models for longitudinal data," *Biometrics*, pp. 963–974, 1982.

[2] M. J. Lindstrom and D. M. Bates, "Newton—raphson and em algorithms for linear mixed-effects models for repeated-measures data," *Journal of the American Statistical Association*, vol. 83, no. 404, pp. 1014–1022, 1988.

[3] G. M. Fitzmaurice, N. M. Laird, and J. H. Ware, *Applied longitudinal analysis*, vol. 998. John Wiley & Sons, 2012.

[4] G. Verbeke and E. Lesaffre, "A linear mixed-effects model with heterogeneity in the random-effects population," *Journal of the American Statistical Association*, vol. 91, no. 433, pp. 217–221, 1996.

[5] W. Xu and D. Hedeker, "A random-effects mixture model for classifying treatment response in longitudinal clinical trials," *Journal of biopharmaceutical statistics*, vol. 11, no. 4, pp. 253–273, 2001.

[6] M. Jessica *et al.*, "A within-subject normal-mixture model with mixed-effects for analyzing heart rate variability," *Journal of Biometrics & Biostatistics*, 2012.

[7] N. G. Pakker, D. W. Notermans, R. J. De Boer, M. Roos, F. De Wolf, A. Hill, J. M. Leonard, S. A. Danner, F. Miedema, and P. T. A. Schellekens, "Biphasic kinetics of peripheral blood t cells after triple combination therapy in hiv-1 infection: a composite of redistribution and proliferation," *Nature medicine*, vol. 4, no. 2, pp. 208–214, 1998.

[8] R. A. Arnaout, D. Wodarz, *et al.*, "Hiv–1 dynamics revisited: biphasic decay by cytotoxic t lymphocyte killing?," *Proceedings of the Royal Society of London. Series B: Biological Sciences*, vol. 267, no. 1450, pp. 1347–1354, 2000.

[9] M. Tsiang, J. F. Rooney, J. J. Toole, and C. S. Gibbs, "Biphasic clearance kinetics of hepatitis b virus from patients during adefovir dipivoxil therapy," *Hepatology*, vol. 29, no. 6, pp. 1863–1869, 1999.

[10] A. U. Neumann, N. P. Lam, H. Dahari, D. R. Gretch, T. E. Wiley, T. J. Layden, and A. S. Perelson, "Hepatitis c viral dynamics in vivo and the antiviral efficacy of interferon-α therapy," *Science*, vol. 282, no. 5386, pp. 103–107, 1998.

[11] F. Michor, T. P. Hughes, Y. Iwasa, S. Branford, N. P. Shah, C. L. Sawyers, and M. A. Nowak, "Dynamics of chronic myeloid leukaemia," *Nature*, vol. 435, no. 7046, pp. 1267–1270, 2005.

[12] A. M. Stein, D. Bottino, V. Modur, S. Branford, J. Kaeda, J. M. Goldman, T. P. Hughes, J. P. Radich, and A. Hochhaus, "Bcr–abl transcript dynamics support the hypothesis that leukemic stem cells are reduced during imatinib treatment," *Clinical Cancer Research*, vol. 17, no. 21, pp. 6812–6821, 2011.

[13] M. Tang, R. Zhao, H. van de Velde, C. Mitsiades, S. Viselli, R. Neuwirth, D.-L. Esseltine, K. Anderson, J. F. S. Miguel, P. G. Richardson, M. H. Tomasson, and F. Michor, "Myeloma stem cells are relatively insensitive to targeted therapy." Submitted.

[14] C. H. Morrell, J. D. Pearson, H. B. Carter, and L. J. Brant, "Estimating unknown transition times using a piecewise nonlinear mixed-effects model in men with prostate cancer," *Journal of the American Statistical Association*, vol. 90, no. 429, pp. 45–53, 1995.

[15] J. C. Pinheiro and D. M. Bates, *Mixed effects models in S and S-PLUS*. Springer, 2000.

[16] E. N. Naumova, A. Must, and N. M. Laird, "Tutorial in biostatistics: evaluating the impact of 'critical periods' in longitudinal studies of growth using piecewise mixed effects models," *International journal of epidemiology*, vol. 30, no. 6, pp. 1332–1341, 2001.

[17] R. Cudeck and K. J. Klebe, "Multiphase mixed-effects models for repeated measures data.," *Psychological methods*, vol. 7, no. 1, p. 41, 2002.

[18] J. R. Harring, R. Cudeck, and S. H. du Toit, "Fitting partially nonlinear random coefficient models as sems," *Multivariate Behavioral Research*, vol. 41, no. 4, pp. 579–596, 2006.

[19] D. K. Pauler and N. M. Laird, "A mixture model for longitudinal data with application to assessment of noncompliance," *Biometrics*, vol. 56, no. 2, pp. 464–472, 2000.

[20] X. Lu and Y. Huang, "Bayesian analysis of nonlinear mixed-effects mixture models for longitudinal data with heterogeneity and skewness," *Statistics in medicine*, 2014.

[21] S. M. Hammer, F. Vaida, K. K. Bennett, M. K. Holohan, L. Sheiner, J. J. Eron, L. J. Wheat, R. T. Mitsuyasu, R. M. Gulick, F. T. Valentine, *et al.*, "Dual vs single protease inhibitor therapy following antiretroviral treatment failure: a randomized trial," *Jama*, vol. 288, no. 2, pp. 169–180, 2002.

[22] A. S. Perelson, P. Essunger, Y. Cao, M. Vesanen, A. Hurley, K. Saksela, M. Markowitz, and D. D. Ho, "Decay characteristics of hiv-1-infected compartments during combination therapy," 1997.

[23] J. Chin Choy and L. Broemeling, "Some bayesian inferences for a changing linear model," *Technometrics*, vol. 22, no. 1, pp. 71–78, 1980.

[24] M. Basseville, I. V. Nikiforov, *et al.*, *Detection of abrupt changes: theory and application*, vol. 104. Prentice Hall Englewood Cliffs, 1993.

[25] J. Chen and A. K. Gupta, *Parametric statistical change point analysis: with applications to genetics, medicine, and finance*. Springer, 2011.

[26] B. P. Carlin, A. E. Gelfand, and A. F. Smith, "Hierarchical bayesian analysis of changepoint problems," *Applied statistics*, pp. 389–405, 1992.

[27] D. V. Hinkley, "On the ratio of two correlated normal random variables," *Biometrika*, vol. 56, no. 3, pp. 635–639, 1969.

[28] L. Held, "Simultaneous posterior probability statements from monte carlo output," *Journal of Computational and Graphical Statistics*, vol. 13, no. 1, 2004.

[29] J. Besag, P. Green, D. Higdon, and K. Mengersen, "Bayesian computation and stochastic systems," *Statistical Science*, pp. 3–41, 1995.

[30] A. Agresti and B. A. Coull, "Approximate is better than "exact" for interval estimation of binomial proportions," *The American Statistician*, vol. 52, no. 2, pp. 119–126, 1998.

[31] J. F. San Miguel, R. Schlag, N. K. Khuageva, M. A. Dimopoulos, O. Shpilberg, M. Kropff, I. Spicka, M. T. Petrucci, A. Palumbo, O. S. Samoilova, *et al.*, “Bortezomib plus melphalan and prednisone for initial treatment of multiple myeloma,” *New England Journal of Medicine*, vol. 359, no. 9, pp. 906–917, 2008.

[32] A. van den Hout, G. Muniz-Terrera, and F. E. Matthews, “Smooth random change point models,” *Statistics in medicine*, vol. 30, no. 6, pp. 599–610, 2011.

[33] A. Palumbo and K. Anderson, “Multiple myeloma,” *N. Engl. J. Med.*, vol. 364, pp. 1046–1060, Mar 2011.

[34] P. G. Richardson, B. Barlogie, J. Berenson, S. Singhal, S. Jagannath, D. Irwin, S. V. Rajkumar, G. Srkalovic, M. Alsina, R. Alexanian, *et al.*, “A phase 2 study of bortezomib in relapsed, refractory myeloma,” *New England Journal of Medicine*, vol. 348, no. 26, pp. 2609–2617, 2003.

[35] P. G. Richardson, P. Sonneveld, M. Schuster, D. Irwin, E. Stadtmauer, T. Facon, J.-L. Harousseau, D. Ben-Yehuda, S. Lonial, H. Goldschmidt, *et al.*, “Extended follow-up of a phase 3 trial in relapsed multiple myeloma: final time-to-event results of the apex trial,” *Blood*, vol. 110, no. 10, pp. 3557–3560, 2007.

[36] P. G. Richardson, P. Sonneveld, M. W. Schuster, D. Irwin, E. A. Stadtmauer, T. Facon, J.-L. Harousseau, D. Ben-Yehuda, S. Lonial, H. Goldschmidt, *et al.*, “Bortezomib or high-dose dexamethasone for relapsed multiple myeloma,” *New England Journal of Medicine*, vol. 352, no. 24, pp. 2487–2498, 2005.

[37] J. San-Miguel, J. Bladé, O. Shpilberg, S. Grosicki, F. Maloisel, C.-K. Min, M. P. Zarzuela, T. Robak, S. V. Prasad, Y. T. Goh, *et al.*, “Phase 2 randomized study of bortezomib-melphalan-prednisone with or without siltuximab (anti–il-6) in multiple myeloma,” *Blood*, vol. 123, no. 26, pp. 4136–4142, 2014.

[38] R. Alexanian, A. Haut, A. U. Khan, M. Lane, E. M. McKelvey, P. J. Migliore, W. Stuckey, and H. E. Wilson, “Treatment for multiple myeloma: combination chemotherapy with different melphalan dose regimens,” *Jama*, vol. 208, no. 9, pp. 1680–1685, 1969.

[39] R. A. Kyle and S. V. Rajkumar, “Multiple myeloma,” *N. Engl. J. Med.*, vol. 351, pp. 1860–1873, Oct 2004.

[40] J. F. San Miguel, R. Schlag, N. K. Khuageva, M. A. Dimopoulos, O. Shpilberg, M. Kropff, I. Spicka, M. T. Petrucci, A. Palumbo, O. S. Samoilova, *et al.*, “Continued overall survival benefit after 5 years’ follow-up with bortezomib-melphalan-prednisone (vmp) versus melphalan-prednisone (mp) in patients with previously untreated multiple myeloma, and no increased risk of second primary malignancies: final results of the phase 3 vista trial,” in *ASH Annual Meeting Abstracts*, vol. 118, p. 476, 2011.

[41] W. Matsui, C. A. Huff, Q. Wang, M. T. Malehorn, J. Barber, Y. Tanhehco, B. D. Smith, C. I. Civin, and R. J. Jones, “Characterization of clonogenic multiple myeloma cells,” *Blood*, vol. 103, no. 6, pp. 2332–2336, 2004.

[42] H.-J. Kim, M. P. Fay, E. J. Feuer, and D. N. Midthune, “Permutation tests for joinpoint regression with applications to cancer rates,” *Statistics in medicine*, vol. 19, no. 3, pp. 335–351, 2000.

[43] D. J. Hudson, “Fitting segmented curves whose join points have to be estimated,” *Journal of the American Statistical Association*, vol. 61, no. 316, pp. 1097–1129, 1966.

[44] R. C. Tiwari, K. A. Cronin, W. Davis, E. J. Feuer, B. Yu, and S. Chib, “Bayesian model selection for join point regression with application to age-adjusted cancer rates,” *Journal of the Royal Statistical Society: Series C (Applied Statistics)*, vol. 54, no. 5, pp. 919–939, 2005.

[45] Y. Iwasa, M. A. Nowak, and F. Michor, “Evolution of resistance during clonal expansion,” *Genetics*, vol. 172, no. 4, pp. 2557–2566, 2006.

[46] B. Dune and S. Salmon, “A clinical staging system for multiple myeloma,” *Cancer*, vol. 36, no. 842, p. 4, 1975.

[47] C. T. Hansen, P. T. Pedersen, L. C. Nielsen, and N. Abildgaard, “Evaluation of the serum free light chain (sFLC) analysis in prediction of response in symptomatic multiple myeloma patients: rapid profound reduction in involved FLC predicts achievement of VGPR,” *Eur. J. Haematol.*, vol. 93, pp. 407–413, Nov 2014.

[48] S. Kumar, A. Dispenzieri, M. Lacy, M. Gertz, F. Buadi, S. Pandey, P. Kapoor, D. Dingli, S. Hayman, N. Leung, *et al.*, “Continued improvement in survival in multiple myeloma: changes in early mortality and outcomes in older patients,” *Leukemia*, vol. 28, no. 5, pp. 1122–1128, 2014.

[49] M. Gerlinger, A. J. Rowan, S. Horswell, J. Larkin, D. Endesfelder, E. Gronroos, P. Martinez, N. Matthews, A. Stewart, P. Tarpey, *et al.*, “Intratumor heterogeneity and branched evolution revealed by multiregion sequencing,” *New England Journal of Medicine*, vol. 366, no. 10, pp. 883–892, 2012.

[50] J. P. Patel, M. Gönen, M. E. Figueroa, H. Fernandez, Z. Sun, J. Racevskis, P. Van Vlierberghe, I. Dolgalev, S. Thomas, O. Aminova, *et al.*, “Prognostic relevance of integrated genetic profiling in acute myeloid leukemia,” *New England Journal of Medicine*, vol. 366, no. 12, pp. 1079–1089, 2012.

[51] M. J. Walter, D. Shen, L. Ding, J. Shao, D. C. Koboldt, K. Chen, D. E. Larson, M. D. McLellan, D. Dooling, R. Abbott, *et al.*, “Clonal architecture of secondary acute myeloid leukemia,” *New England Journal of Medicine*, vol. 366, no. 12, pp. 1090–1098, 2012.

[52] L. M. Pilarski and A. R. Belch, “Clonotypic myeloma cells able to xenograft myeloma to nonobese diabetic severe combined immunodeficient mice copurify with cd34+ hematopoietic progenitors,” *Clinical cancer research*, vol. 8, no. 10, pp. 3198–3204, 2002.

[53] L. Mirandola, Y. Yu, M. R. Jenkins, R. Chiaramonte, E. Cobos, C. M. John, and M. Chiriva-Internati, “Tracking human multiple myeloma xenografts in nod-rag-1/il-2 receptor gamma chain-null mice with the novel biomarker akap-4,” *BMC cancer*, vol. 11, no. 1, p. 394, 2011.

[54] S. Yaccoby and J. Epstein, “The proliferative potential of myeloma plasma cells manifest in the scid-hu host,” *Blood*, vol. 94, no. 10, pp. 3576–3582, 1999.

[55] T. Paíno, E. M. Ocio, B. Paiva, L. San-Segundo, M. Garayoa, N. C. Gutiérrez, M. E. Sarasquete, A. Pandiella, A. Orfao, and J. F. San Miguel, “Cd20 positive cells are undetectable in the majority of multiple myeloma cell lines and are not associated with a cancer stem cell phenotype,” *Haematologica*, vol. 97, no. 7, pp. 1110–1114, 2012.

[56] D. Zipori, “The hemopoietic stem cell niche versus the microenvironment of the multiple myeloma-tumor initiating cell,” *Cancer Microenvironment*, vol. 3, no. 1, pp. 15–28, 2010.

[57] C. Dierks, J. Grbic, K. Zirlik, R. Beigi, N. P. Englund, G.-R. Guo, H. Veelken, M. Engelhardt, R. Mertelsmann, J. F. Kelleher, *et al.*, “Essential role of stromally induced hedgehog signaling in b-cell malignancies,” *Nature medicine*, vol. 13, no. 8, pp. 944–951, 2007.

[58] D. E. Reece, D. Sullivan, S. Lonial, A. F. Mohrbacher, G. Chatta, C. Shustik, H. Burris III, K. Venkatakrishnan, R. Neuwirth, W. J. Riordan, *et al.*, “Pharmacokinetic and pharmacodynamic study of two doses of bortezomib in patients with relapsed multiple myeloma,” *Cancer chemotherapy and pharmacology*, vol. 67, no. 1, pp. 57–67, 2011.

[59] C. Leung-Hagesteijn, N. Erdmann, G. Cheung, J. J. Keats, A. K. Stewart, D. E. Reece, K. C. Chung, and R. E. Tiedemann, "Xbp1s-negative tumor b cells and pre-plasmablasts mediate therapeutic proteasome inhibitor resistance in multiple myeloma," *Cancer Cell*, vol. 24, no. 3, pp. 289–304, 2013.

[60] A. K. Stewart, P. G. Richardson, and J. F. San-Miguel, "How i treat multiple myeloma in younger patients," *Blood*, vol. 114, no. 27, pp. 5436–5443, 2009.

[61] J. P. Laubach, C. S. Mitsiades, A. Mahindra, M. R. Luskin, J. Rosenblatt, I. M. Ghobrial, R. L. Schlossman, D. Avigan, N. Raje, N. C. Munshi, *et al.*, "Management of relapsed and relapsed/refractory multiple myeloma," *Journal of the National Comprehensive Cancer Network*, vol. 9, no. 10, pp. 1209–1216, 2011.

[62] M.-V. Mateos, M.-T. Hernández, P. Giraldo, J. de la Rubia, F. de Arriba, L. L. Corral, L. Rosiñol, B. Paiva, L. Palomera, J. Bargay, *et al.*, "Lenalidomide plus dexamethasone for high-risk smoldering multiple myeloma," *New England Journal of Medicine*, vol. 369, no. 5, pp. 438–447, 2013.

[63] R. Siegel, D. Naishadham, and A. Jemal, "Cancer statistics, 2012," *CA: a cancer journal for clinicians*, vol. 62, no. 1, pp. 10–29, 2012.

[64] M. Brittan and N. Wright, "Stem cell in gastrointestinal structure and neoplastic development," *Gut*, vol. 53, no. 6, pp. 899–910, 2004.

[65] B. Vogelstein and K. W. Kinzler, *The genetic basis of human cancer*. McGraw-Hill, Health Professions Division, 1998.

[66] L.-K. Su, B. Vogelstein, and K. W. Kinzler, "Association of the apc tumor suppressor protein with catenins," *Science*, vol. 262, no. 5140, pp. 1734–1737, 1993.

[67] I. Nathke, "Inke nathke: The abcs of apc. interview by caitlin sedwick.," *The Journal of cell biology*, vol. 189, no. 5, pp. 774–775, 2010.

[68] M. L. Bisgaard and S. Bülow, "Familial adenomatous polyposis (fap): genotype correlation to fap phenotype with osteomas and sebaceous cysts," *American journal of medical genetics Part A*, vol. 140, no. 3, pp. 200–204, 2006.

[69] E. R. Fearon and B. Vogelstein, "A genetic model for colorectal tumorigenesis," *Cell*, vol. 61, no. 5, pp. 759–767, 1990.

[70] S. Zhou, K. W. Kinzler, and B. Vogelstein, "Going mad with smads," *The New England journal of medicine*, vol. 341, no. 15, pp. 1144–1146, 1999.

[71] G. Smith, F. A. Carey, J. Beattie, M. J. Wilkie, T. J. Lightfoot, J. Coxhead, R. C. Garner, R. J. Steele, and C. R. Wolf, "Mutations in apc, kirsten-ras, and p53—alternative genetic pathways to colorectal cancer," *Proceedings of the National Academy of Sciences*, vol. 99, no. 14, pp. 9433–9438, 2002.

[72] M. D. Erisman, P. G. Rothberg, R. E. Diehl, C. C. Morse, J. Spandorfer, and S. Astrin, "Deregulation of c-myc gene expression in human colon carcinoma is not accompanied by amplification or rearrangement of the gene.," *Molecular and cellular biology*, vol. 5, no. 8, pp. 1969–1976, 1985.

[73] T.-C. He, A. B. Sparks, C. Rago, H. Hermeking, L. Zawel, L. T. da Costa, P. J. Morin, B. Vogelstein, and K. W. Kinzler, "Identification of c-myc as a target of the apc pathway," *Science*, vol. 281, no. 5382, pp. 1509–1512, 1998.

[74] L. A. Aaltonen, P. Peltomaki, F. S. Leach, P. Sistonen, L. Pylkkanen, J.-P. Mecklin, H. Jarvinen, S. M. Powell, J. Jen, *et al.*, "Clues to the pathogenesis of familial colorectal cancer," *Science*, vol. 260, no. 5109, pp. 812–816, 1993.

[75] C. Lengauer, K. Kinzler, and B. Vogelstein, “Genetic instability in colorectal cancers,” *Nature*, vol. 386, no. 6625, pp. 623–627, 1997.

[76] C. Lengauer, K. W. Kinzler, and B. Vogelstein, “Genetic instabilities in human cancers,” *Nature*, vol. 396, no. 6712, pp. 643–649, 1998.

[77] M. S. Pino and D. C. Chung, “The chromosomal instability pathway in colon cancer,” *Gastroenterology*, vol. 138, no. 6, pp. 2059–2072, 2010.

[78] P. V. Jallepalli and C. Lengauer, “Chromosome segregation and cancer: cutting through the mystery,” *Nature Reviews Cancer*, vol. 1, no. 2, pp. 109–117, 2001.

[79] A. Humphries and N. A. Wright, “Colonic crypt organization and tumorigenesis,” *Nature Reviews Cancer*, vol. 8, no. 6, pp. 415–424, 2008.

[80] C. S. Potten, M. Kellett, S. A. Roberts, D. Rew, and G. Wilson, “Measurement of in vivo proliferation in human colorectal mucosa using bromodeoxyuridine.,” *Gut*, vol. 33, no. 1, pp. 71–78, 1992.

[81] B. Iacopetta, “Are there two sides to colorectal cancer?,” *International journal of cancer*, vol. 101, no. 5, pp. 403–408, 2002.

[82] N. A. Wright, “Epithelial stem cell repertoire in the gut: clues to the origin of cell lineages, proliferative units and cancer,” *International journal of experimental pathology*, vol. 81, no. 2, pp. 117–143, 2000.

[83] T. Wilson, B. Ponder, and N. Wright, “Use of a mouse chimaeric model to study cell migration patterns in the small intestinal epithelium,” *Cell Proliferation*, vol. 18, no. 3, pp. 333–343, 1985.

[84] C. S. Potten, M. Kellett, D. Rew, and S. A. Roberts, “Proliferation in human gastrointestinal epithelium using bromodeoxyuridine in vivo: data for different sites, proximity to a tumour, and polyposis coli.,” *Gut*, vol. 33, no. 4, pp. 524–529, 1992.

[85] A. J. Merritt, C. S. Potten, A. Watson, D. Y. Loh, K.-i. Nakayama, and J. A. Hickman, “Differential expression of bcl-2 in intestinal epithelia. correlation with attenuation of apoptosis in colonic crypts and the incidence of colonic neoplasia,” *Journal of Cell Science*, vol. 108, no. 6, pp. 2261–2271, 1995.

[86] S. Tsubouchi, “Theoretical implications for cell migration through the crypt and the villus of labelling studies conducted at each position within the crypt.,” *Cell and tissue kinetics*, vol. 16, no. 5, pp. 441–456, 1983.

[87] C. Nordling, “A new theory on the cancer-inducing mechanism,” *British journal of cancer*, vol. 7, no. 1, p. 68, 1953.

[88] N. L. Komarova and L. Wang, “Report initiation of colorectal cancer,” *Cell Cycle*, vol. 3, no. 12, pp. 1558–1565, 2004.

[89] F. Michor, Y. Iwasa, H. Rajagopalan, C. Lengauer, and M. A. Nowak, “Linear model of colon cancer initiation,” *CELL CYCLE-LANDES BIOSCIENCE-*, vol. 3, pp. 358–362, 2004.

[90] P. Buske, J. Galle, N. Barker, G. Aust, H. Clevers, and M. Loeffler, “A comprehensive model of the spatio-temporal stem cell and tissue organisation in the intestinal crypt,” *PLoS computational biology*, vol. 7, no. 1, p. e1001045, 2011.

[91] M. A. Nowak, F. Michor, and Y. Iwasa, “The linear process of somatic evolution,” *Proceedings of the National Academy of Sciences*, vol. 100, no. 25, pp. 14966–14969, 2003.

[92] I. Van Leeuwen, H. Byrne, O. Jensen, and J. King, "Crypt dynamics and colorectal cancer: advances in mathematical modelling," *Cell proliferation*, vol. 39, no. 3, pp. 157–181, 2006.

[93] G. De Matteis, A. Graudenzi, and M. Antoniotti, "A review of spatial computational models for multi-cellular systems, with regard to intestinal crypts and colorectal cancer development," *Journal of mathematical biology*, vol. 66, no. 7, pp. 1409–1462, 2013.

[94] M. Loeffler, R. Stein, H.-E. Wichmann, C. S. Potten, P. Kaur, and S. Chwalinski, "Intestinal cell proliferation. i. a comprehensive model of steady-state proliferation in the crypt," *Cell Proliferation*, vol. 19, no. 6, pp. 627–645, 1986.

[95] M. Loeffler, C. S. Potten, U. Paulus, J. Glatzer, and S. Chwalinski, "Intestinal crypt proliferation. ii. computer modelling of mitotic index data provides further evidence for lateral and vertical cell migration in the absence of mitotic activity," *Cell Proliferation*, vol. 21, no. 4, pp. 247–258, 1988.

[96] T. Gerike, U. Paulus, C. S. Potten, and M. Loeffler, "A dynamic model of proliferation and differentiation in the intestinal crypt based on a hypothetical intraepithelial growth factor," *Cell proliferation*, vol. 31, no. 2, pp. 93–110, 1998.

[97] F. Meineke, C. S. Potten, and M. Loeffler, "Cell migration and organization in the intestinal crypt using a lattice-free model," *Cell proliferation*, vol. 34, no. 4, pp. 253–266, 2001.

[98] S. Y. Wong, K.-H. Chiam, C. T. Lim, and P. Matsudaira, "Computational model of cell positioning: directed and collective migration in the intestinal crypt epithelium," *Journal of The Royal Society Interface*, vol. 7, no. Suppl 3, pp. S351–S363, 2010.

[99] G. R. Mirams, A. G. Fletcher, P. K. Maini, and H. M. Byrne, "A theoretical investigation of the effect of proliferation and adhesion on monoclonal conversion in the colonic crypt," *Journal of theoretical biology*, vol. 312, pp. 143–156, 2012.

[100] Y. Kikuchi, W. N. Dinjens, and F. Bosman, "Proliferation and apoptosis in proliferative lesions of the colon and rectum," *Virchows Archiv*, vol. 431, no. 2, pp. 111–117, 1997.

[101] U. Paulus, C. S. Potten, and M. Loeffler, "A model of the control of cellular regeneration in the intestinal crypt after perturbation based solely on local stem cell regulation," *Cell proliferation*, vol. 25, no. 6, pp. 559–578, 1992.

[102] C. S. Potten, G. Owen, and S. A. Roberts, "The temporal and spatial changes in cell proliferation within the irradiated crypts of the murine small intestine," *International journal of radiation biology*, vol. 57, no. 1, pp. 185–199, 1990.

[103] R. J. Albertini, J. A. Nicklas, J. P. O'Neill, and S. H. Robison, "In vivo somatic mutations in humans: measurement and analysis," *Annual review of genetics*, vol. 24, no. 1, pp. 305–326, 1990.

[104] C. Hornsby, K. M. Page, and I. Tomlinson, "The¡ i¿ in vivo¡/i¿ rate of somatic¡ i¿ adenomatous polyposis coli¡/i¿ mutation," *The American journal of pathology*, vol. 172, no. 4, pp. 1062–1068, 2008.

[105] T. Iwama, "Somatic mutation rate of the apc gene," *Japanese journal of clinical oncology*, vol. 31, no. 5, pp. 185–187, 2001.

[106] C. S. Potten, "The significance of spontaneous and induced apoptosis in the gastrointestinal tract of mice," *Cancer and Metastasis Reviews*, vol. 11, no. 2, pp. 179–195, 1992.

[107] S. Tsubouchi and C. S. Potten, "Recruitment of cells in the small intestine into rapid cell cycle by small doses of external γ or internal β-radiation," *International Journal of Radiation Biology*, vol. 48, no. 3, pp. 361–369, 1985.

[108] M. Varedi, R. Chinery, G. H. Greeley Jr, D. N. Herndon, and E. W. Englander, "Thermal injury effects on intestinal crypt cell proliferation and death are cell position dependent," *American Journal of Physiology-Gastrointestinal and Liver Physiology*, vol. 280, no. 1, pp. G157–G163, 2001.

[109] G. G. Altmann, "Influence of starvation and refeeding on mucosal size and epithelial renewal in the rat small intestine," *American Journal of Anatomy*, vol. 133, no. 4, pp. 391–400, 1972.

[110] A. Traulsen, J. M. Pacheco, and D. Dingli, "Reproductive fitness advantage of¡ i¿ bcr¡/i¿–¡ i¿ abl¡/i¿ expressing leukemia cells," *Cancer letters*, vol. 294, no. 1, pp. 43–48, 2010.

[111] S. M. Ross, *Introduction to probability models*. Academic press, 2014.

[112] T. F. Coleman and C. Van Loan, *Handbook for matrix computations*, vol. 4. Siam, 1988.

[113] C. S. Potten, "Epithelial cell growth and differentiation. ii. intestinal apoptosis," *American Journal of Physiology-Gastrointestinal and Liver Physiology*, vol. 36, no. 2, p. G253, 1997.

[114] Y. Iwasa, F. Michor, and M. A. Nowak, "Stochastic tunnels in evolutionary dynamics," *Genetics*, vol. 166, no. 3, pp. 1571–1579, 2004.

[115] N. L. Komarova, A. Sengupta, and M. A. Nowak, "Mutation–selection networks of cancer initiation: tumor suppressor genes and chromosomal instability," *Journal of theoretical biology*, vol. 223, no. 4, pp. 433–450, 2003.

[116] B. M. Boman, J. Z. Fields, K. L. Cavanaugh, A. Guetter, and O. A. Runquist, "How dysregulated colonic crypt dynamics cause stem cell overpopulation and initiate colon cancer," *Cancer research*, vol. 68, no. 9, pp. 3304–3313, 2008.

[117] B. M. Boman, J. Z. Fields, O. Bonham-Carter, and O. A. Runquist, "Computer modeling implicates stem cell overproduction in colon cancer initiation," *Cancer research*, vol. 61, no. 23, pp. 8408–8411, 2001.

[118] M. D. Johnston, C. M. Edwards, W. F. Bodmer, P. K. Maini, and S. J. Chapman, "Mathematical modeling of cell population dynamics in the colonic crypt and in colorectal cancer," *Proceedings of the National Academy of Sciences*, vol. 104, no. 10, pp. 4008–4013, 2007.

[119] N. L. Komarova, "Loss-and gain-of-function mutations in cancer: mass-action, spatial and hierarchical models," *Journal of Statistical Physics*, vol. 128, no. 1-2, pp. 413–446, 2007.